THERMAL PERFORMANCE SENSITIVITY STUDIES IN SUPPORT OF MATERIAL MODELING FOR EXTENDED STORAGE OF USED NUCLEAR FUEL

Fuel Cycle Research & Development

Prepared for
U.S. Department of Energy
Used Fuel Disposition Campaign

JM Cuta
SR Suffield
JA Fort
HE Adkins

September 27, 2013

FCRD-UFD-2013-000257
PNNL-22646

Reviewed by:

PNNL Project Manager

Signature on file

_____

Brady Hanson

SUMMARY

This report fulfills the M3 milestone M3FT-13PN0810025, “Perform Sensitivity Analysis Report”, under Work Package FT-13PN081002.

This report has been approved by all internal reviewers and is entered into the PNNL publication database (ERICA) as PNNL-22646.

The U.S. Department of Energy Office of Nuclear Energy (DOE-NE), Office of Fuel Cycle Technology, established the Used Fuel Disposition Campaign (UFDC) to conduct research and development (R&D) to support storage, transportation, and disposal of used nuclear fuel and high-level radioactive waste. Since nearly all potential degradation mechanisms are sensitive to temperature and in some cases, temperature history, the need for realistic, detailed temperatures and temperature distributions in the used nuclear fuel, storage canisters, and storage systems has been identified in an R&D gap analysis as one of several key cross-cutting needs.

The work reported here is an investigation of the sensitivity of component temperatures in a specific storage system, including fuel cladding temperatures, in response to modeling assumptions that differ from design-basis, including age-related changes that could degrade the thermal behavior of the system. Preliminary evaluations of representative horizontal and vertical storage systems at design basis conditions provides general insight into the expected behavior of storage systems over extended periods of time. The sensitivity analyses were performed using the detailed computational fluid dynamics (CFD) model of a horizontal storage module developed for the inspections performed at the Calvert Cliffs Nuclear Power Station’s Independent Spent Fuel Storage Installation (ISFSI) in June 2012.

This storage module (designated HSM15) is a site-specific variant of the standard NUHOMS® module, and contains a 24P dry shielded canister (DSC) loaded with twenty-four CE 14x14 spent fuel assemblies. The total decay heat load for the DSC in HSM15 was 10.58 kW at the time of loading (November 1996), after the fuel had spent approximately 12 years in wet storage. At the time of inspection (June 2012), after approximately16 years in dry storage, the total decay heat in the canister was calculated to be 7.58 kW. For the sensitivity analyses, the decay heat load for this fuel was projected to 300 years, and evaluations were performed for 6 kW, 4 kW, and 2 kW, corresponding to fuel approximately 50 years, 100 years, and 300 years old, respectively.

The purpose of these sensitivity studies is to provide a realistic example of how changes in the physical properties or configuration of the storage system components can affect temperatures and temperature distributions. The magnitudes of these sensitivities can provide guidance for identifying appropriate modeling assumptions for thermal evaluations of extended storage of used nuclear fuel. Three specific areas of interest were identified for this study:

- degradation of the canister backfill gas from pure helium to a mixture of air and helium, resulting from postulated leakage due to stress corrosion cracking (SCC) of canister welds

- uncertainties or changes in surface emissivity of system components, resulting from corrosion or other aging mechanisms, which could cause potentially significant changes in temperatures and temperature distributions
- the effect of fuel assembly position within the basket cells on fuel cladding and basket temperatures in the canister.

In general, the results of this study have shown that variation in the parameters examined have relatively small effects on peak temperatures and temperature distributions within a storage system initially loaded at approximately 45% of maximum thermal design basis. The results also show that these effects tend to diminish with time, due to the general decrease in temperatures with decreasing decay heat load. In particular, this study suggests that changes in surface emissivities of system components over long periods of time are not expected to have significant effects on overall temperatures for extended storage conditions. However, the uncertainty of the emissivity of cladding with much higher burnup or of newer cladding materials could have a large enough effect on the calculated peak clad temperature that some mechanisms (e.g., hydride reorientation and annealing of radiation damage) could be affected.

The evaluations of the effect of backfill gas composition on DSC surface temperature distribution suggest that measurements may provide information to assist in monitoring for evidence of the possibility of SCC of the DSC welds. However, it must be noted that these temperature differences are due to significant natural recirculation of the backfill gas within the 24P canister. Canister designs that do not have significant natural circulation flow paths around the basket would not show the variation in the top-to-side temperature difference with fill gas composition observed in this study. The possibility of using this behavior to detect temperature differences that could potentially provide information on backfill gas composition is limited to canisters of similar design to the 24P DSC.

Evaluation of natural recirculation within the closed container of the DSC using a CFD model is constrained by the limitation of using the Boussinesq approximation to capture the buoyancy effects that drive natural circulation of the fill gas, rather than treating it as an ideal gas. The ideal gas law can be used only if the problem is solved as a transient calculation. A transient solution is impractical for the HSM15 model, or any typical spent fuel storage system, due to the large size of such a model and the computational effort required by the long thermal time constants of the system. The Boussinesq approximation is accurate for small temperature differences, and temperature differences in dry storage canisters are generally much larger than the verified range of the model.

Based on comparisons with results for simplified models where the ideal gas law can be used to obtain an appropriate solution in steady-state and transient evaluations, there is some confidence that the Boussinesq approximation approach can produce a reasonably accurate solution for the range of conditions evaluated in this study, even though the large range of temperatures exceeds the recommended range for this approximate model. However, additional modeling studies are strongly recommended, to verify and validate the natural circulation behavior predicted with CFD models of flow dynamics within the dry storage canister. This is particularly important if evaluations are to be carried out for vertical systems, and for evaluations in horizontal and vertical systems at decay heat loads approaching system design-basis limits. In such systems, the temperature

differences are likely to be much larger than encountered in this study of a DSC that was initially loaded at less than 60% of design basis.

The results of this study show that at low decay heat loadings, changes in surface emissivities of components of the canister and storage module have only a minor effect on system peak temperatures, and this effect diminishes with time, due to decreasing decay heat load. However, this study should be extended to systems at thermal design basis and to systems without significant internal natural convection heat transfer within the DSC. At higher decay heat loading, and with the generally steeper temperature gradients in systems that rely on thermal radiation and conduction only, without convection, to remove heat from the fuel assemblies, the effect of surface emissivities may have a greater influence on peak temperatures and temperature distributions than are indicated by the limited scope of the current study.

The homogeneous effective conductivity model used by necessity in this study with a CFD model of the storage system allowed only limited evaluation of the effect of fuel assembly eccentricity within the storage compartment. The effect of eccentricity of the fuel assemblies within the basket was shown to be negligible when using the homogeneous k_{eff} model to represent the fuel assemblies, and ignoring potential effects due to contact conduction. Additional work is needed with a detailed model that can take into account conduction due to contact between the fuel assembly structure and the compartment wall in a multi-assembly canister model. The specific recommendation is to develop detailed models using the COBRA-SFS code for representative horizontal and vertical systems.

ACKNOWLEDGMENTS

Special thanks are owed to the technical editor, Cornelia Brim, for extraordinary efforts to assist in the production of the final version of this document in a timely manner.

CONTENTS

SUMMARY iv

ACKNOWLEDGMENTS vii

CONTENTS viii

ACRONYMS xii

1. INTRODUCTION 1

2. PRELIMINARY SCOPING STUDY OF TEMPERATURES IN EXTENDED STORAGE 3
   - 2.1 Temperatures in Horizontal Storage 7
   - 2.2 Temperatures in Vertical Storage 10
   - 2.3 Implications for Storage of High Decay Heat Fuel Assemblies 14

3. EVALUATION MODEL FOR SENSITIVITY STUDIES 15
   - 3.1 STAR-CCM+ Model of HSM15 15
   - 3.2 Fuel Effective Conductivity Model 18

4. MATRICES FOR SENSITIVITY EVALUATIONS 25
   - 4.1 Matrix for Backfill Gas Study 25
   - 4.2 Matrix for Emissivity Study 27
   - 4.3 Matrix for Fuel Assembly Eccentricity Study 30
   - 4.4 Fuel Effective Conductivity Models for Sensitivity Studies 32

5. SENSITIVITY EVALUATIONS 37
   - 5.1 Results of Canister Backfill Gas Study 37
     - 5.1.1 CFD Modeling of Natural Convection in Sealed Containers 43
   - 5.2 Results of Surface Emissivities Sensitivity Study 44
     - 5.2.1 Effect of Surface Conditions on Heat Transfer 44
     - 5.2.2 Effect of Assumed Surface Emissivities on System Temperatures 50
   - 5.3 Results of Fuel Assembly Eccentricity Study 61

6. CONCLUSIONS AND RECOMMENDATIONS 65
   - 6.1 Recommendations for Future Work 65

7. REFERENCES 67

Appendix A 69

FIGURES

Figure 2-1. Illustration of Time to Reach Decay Heat Level Where Dry Storage is Possible 3

Figure 2-2. Representative Decay Heat for PWR Fuel Assemblies as a Function of Burnup Compared to Maximum Permitted Decay Heat per Assembly in Dry Storage Systems 5

Figure 2-3. Representative Decay Heat vs. Time for BWR Fuel Assemblies as a Function of Burnup Compared to Maximum Permitted Decay Heat per Assembly in Dry Storage Systems 5

Figure 2-4. Estimated Decay Heat Projections in Dry Storage for 300 Years 7

Figure 2-5. Peak Clad Temperature Predictions for Projected Decay Heat Decrease over Time in Horizontal Storage 7

Figure 2-6. Radial Temperature Distribution through the Canister at the Peak Clad Temperature Location for Projected Decay Heat Decrease over Time in Horizontal Storage 8

Figure 2-7. Axial Temperature Distribution on the Hottest Rod Cladding Surface, for Projected Decay Heat Values over Time in Horizontal Storage (Initially at 40.8 kW) 9

Figure 2-8. Axial Temperature Distribution at the Canister Shell Surface along the Top, for Projected Decay Heat Values over Time in Horizontal Storage (Initially at 40.8 kW) 10

Figure 2-9. Peak Component Temperature Predictions for Projected Decay Heat Decrease over Time in Vertical Storage 11

Figure 2-10. Radial Temperature Distribution through the Canister and Overpack at the Peak Clad Temperature Location for Projected Decay Heat Decrease over Time in Vertical Storage 12

Figure 2-11. Axial Temperature Distribution on the Hottest Rod, for Projected Decay Heat Decrease over Time in Vertical Storage 13

Figure 2-12. Axial Temperature Distribution at the Canister Shell Surface for Projected Decay Heat Decrease over Time in Vertical Storage 13

Figure 3-1. Volume Mesh of HSM15 Assembly: Exterior View 16

Figure 3-2. Planar Slice Through Centerline Showing Volume Mesh of HSM15 and 24P DSC Model in Axial Direction 16

Figure 3-3. Planar Slice Through Mid-line Showing Volume Mesh of HSM15 and 24P DSC Model in Transverse Direction 17

Figure 3-4. Mid-Plane Cross-Sectional View and Exterior View of Internal Geometry in STAR-CCM+ Model of 24P DSC 18

Figure 3-5. Illustration of Typical Computational Mesh for Detailed CFD or FEA Model of Quarter-Section of a Spent Fuel Assembly for Determining Effective Conductivity 19

Figure 4-1. Possible Fuel Assembly/Basket Configurations in Horizontal Storage Systems (NOTE: The diagram is not to scale; the gap width is greatly exaggerated for clarity.) 31

Figure 4-2. Fuel Effective Radial Conductivity for CE 14x14 fuel as a Function of Backfill Gas Composition (for Backfill Gas Sensitivity Study) 33

Figure 4-3. Fuel Effective Axial Conductivity for CE 14x14 Fuel as a Function of Backfill Gas Composition (for Backfill Gas Sensitivity Study) 34

Figure 4-4. Fuel Effective Conductivity for CE 14x14 Fuel as a Function of Surface Emissivities (for Emissivity Sensitivity Study) 35

Figure 4-5. Fuel Effective Conductivity for CE 14x14 Fuel as a Function of Assembly Position within Fuel Compartment (for Assembly Eccentricity Sensitivity Study) 36

Figure 5-1. DSC Internal Temperatures at 7.58 kW Total Decay Heat Load: Results with 100% Helium as Backfill Gas 37

Figure 5-2. DSC Internal Temperatures at 7.28 kW Decay Heat Load: Results with 100% Air as Backfill Gas 38

Figure 5-3. DSC Shell Temperatures at 7.58 kW and 2 kW Decay Heat Loads, Comparing Results with Helium and Air Backfill Gas 39

Figure 5-4. DSC Top Temperatures at 7.58 kW and 2 kW Decay Heat Loads, Comparing Results for all Backfill Gas Compositions Evaluated 40

Figure 5-5. DSC Side Temperatures at 7.58 kW and 2 kW Decay Heat Loads, Comparing Results for all Backfill Gas Compositions Evaluated 40

Figure 5-6. Axial Distribution of DSC Top-to-side Temperature Differences at all Decay Heat Loads for all Backfill Gas Compositions Evaluated in this Study 42

Figure 5-7. Velocity at Axial Midplane in HSM15 42

Figure 5-8. Conceptual Diagram of Heat Flow Path 46

Figure 5-9. Estimated Temperature Drop Across Oxide Layer on Fuel Rod Cladding, for Constant Heat Flux at Postulated Decay Heat Loads over Time 48

Figure 5-11. Estimated Temperature Drop Across Oxide Layer for Constant Heat Flux through DSC Shell at Postulated Decay Heat Loads over Time 49

Figure 5-12. Estimated Temperature Drop Across Oxide Layer for Constant Heat Flux through Fuel Storage Compartment Wall at Postulated Decay Heat Loads over Time 50

Figure 5-13. Axial and Radial Temperature Contours within the DSC at 7.58 kW Decay Heat Load: Case A (Base Case) 51

Figure 5-14. Axial and Radial Temperature Contours within the DSC at 7.58 kW Decay Heat Load: Case B (Bounding Case) 52

Figure 5-15. DSC Temperature Contours at 7.58 kW Decay Heat Load: Case A (Base Case) and Case B (Bounding Case) 53

Figure 5-17. DSC Temperature Contours at 7.58 kW Decay Heat Load: Case D-1 (50% Increase in DSC Internal Surface Emissivities) and Case D-2 (Bounding Emissivities for DSC Internal Surfaces) 54

Figure 5-18. Peak Module Component Temperatures for all Cases in the Emissivity Matrix 55

Figure 5-19. Peak Fuel Cladding Temperatures and DSC Shell Temperatures for all Cases in the Emissivity Matrix 56

Figure 5-20. Comparison of Peak Component Temperatures for Nominal and Bounding Cases over the Full Range of Decay Heat Values Evaluated 58

Figure 5-21. Comparison of Peak Component Temperatures for Case C-1 and C-2 (Varying Surface Emissivities for Module and DSC Shell Exterior) to the Nominal Case (Case A) over Full Range of Decay Heat Values Evaluated 59

Figure 5-22. Comparison of Peak Component Temperatures for Case D-1 and D-2 (Varying Surface Emissivities for DSC Internal Surfaces Only) to the Nominal Case (Case A) over Full Range of Decay Heat Values Evaluated 60

Figure 5-23. Comparison of DSC Internal Temperatures Obtained with Assumed Variations in Fuel Assembly Eccentricity within Fuel Storage Compartment 62

TABLES

Table 3-1. Range of Total Canister Decay Heat Values 15

Table 4-1. Backfill Gas Composition Matrix for Backfill Gas Study 26

Table 4-2. Nominal Emissivity Values for Modeling HSM15 28

Table 4-3. Sensitivity Matrix for Emissivity Study 30

Table 5-1. Peak Temperature Differences Top to Side for Backfill Gas Sensitivity Study 41

Table 5-2. Maximum Component Temperatures in Surface Emissivity Study Cases 57

Table 5-3. Maximum Component Temperatures in Assembly Eccentricity Studies 63

ACRONYMS

BWR	boiling water reactor
CFD	computational fluid dynamics
DOE	U.S. Department of Energy
DOE-NE	U. S. Department of Energy Office of Nuclear Energy
DSC	dry shielded canister
FEA	finite element analysis
GWd/MTU	Gigawatt days per metric ton uranium (measure of burnup)
HSM	horizontal storage module
ISFSI	independent spent fuel storage installation
MPC	multi-purpose canister
NIST	National Institute of Standards and Technology
PNNL	Pacific Northwest National Laboratory
PWR	pressurized water reactor
SCC	stress corrosion cracking

THERMAL PERFORMANCE SENSITIVITY STUDIES IN SUPPORT OF MATERIAL MODELING FOR EXTENDED STORAGE OF USED NUCLEAR FUEL

1. INTRODUCTION

The U.S. Department of Energy Office of Nuclear Energy (DOE-NE), Office of Fuel Cycle Technology, established the Used Fuel Disposition Campaign (UFDC) to conduct research and development (R&D) to support storage, transportation, and disposal of used nuclear fuel and high-level radioactive waste. As part of this work, an R&D gap analysis was performed (Hanson et al. 2012) identifying data gaps and prioritizing efforts to develop the technical bases for demonstration of continued safety of extended storage and subsequent retrieval of used nuclear fuel. The need for realistic, detailed temperatures and temperature distributions in the used nuclear fuel, storage canisters, and storage systems was identified as one of several key cross-cutting needs, since nearly all degradation mechanisms are sensitive to temperature and in some cases, temperature history.

The work reported here is an investigation of the sensitivity of component temperatures of an operating storage system, including fuel cladding temperatures, in response to modeling assumptions that are different from the design-basis for thermal evaluation of the system. Three specific areas of interest were identified for this study:

- degradation of the canister backfill gas from pure helium to a mixture of air and helium, resulting from postulated leakage due to stress corrosion cracking (SCC) of canister welds
- uncertainties or changes in surface emissivity of system components, resulting from corrosion or other aging mechanisms, which could cause potentially significant changes in temperatures and temperature distributions
- the effect of fuel assembly position within the basket cells on fuel cladding and basket temperatures in the canister.

The purpose of these sensitivity studies is to provide a realistic example of how changes in the physical properties or configuration of storage system components can affect temperatures and temperature distributions, and to determine areas where additional data may be required to remove the conservatisms typically included in thermal models. The magnitudes of these sensitivities can provide guidance for identifying appropriate modeling assumptions for thermal evaluations of storage conditions for extended periods and for areas where additional research or modeling may be required. The sensitivity analyses were performed using the detailed computational fluid dynamics (CFD) model of a site-specific NUHOMS® module containing a 24P DSC developed for the inspections performed at the Calvert Cliffs Nuclear Power Station's Independent Spent Fuel Storage Installation (ISFSI) in June 2012 (Suffield et al. 2012).

As a baseline to illustrate the expected temperature versus time behavior in typical spent fuel storage systems, Section 2 contains a preliminary study of temperatures in extended storage for

representative horizontal and vertical systems evaluated at design basis conditions. Section 3 provides a detailed description of the CFD model used to represent the specific spent fuel storage system used in the sensitivity evaluations. Section 4 describes the matrix of sensitivity cases developed to evaluate the thermal consequences of uncertainties in properties or age-related changes in the system. Section 5 presents the results of the sensitivity evaluations, and Section 6 discusses general conclusions derived from the studies of this specific system, and provides recommendations for future work. Cited references are listed in Section 7.

2. PRELIMINARY SCOPING STUDY OF TEMPERATURES IN EXTENDED STORAGE

Initial temperatures in dry storage systems are a direct function of the decay heat of the assemblies at the time of loading in the canister. The general relationship between decay heat and cooling time is shown in Figure 2-1, with a sample exponential radioactive decay curve (based on ANSI/ANS-5.1 2004) normalized to decay heat at time of discharge from the reactor. The vertical (blue) line on the plot corresponds to the point in time when the decay heat has dropped low enough for an assembly to be a candidate for dry storage. In general, the hotter the fuel assembly at time of discharge (effectively, the higher the burnup), the farther to the right the blue line would have to shift before that assembly would be cool enough for dry storage. This plot does not include an absolute time scale, because the decay heat value at which a given assembly would be eligible for dry storage depends on the particular fuel design, its burnup history, and the design of the dry storage system that would receive it.

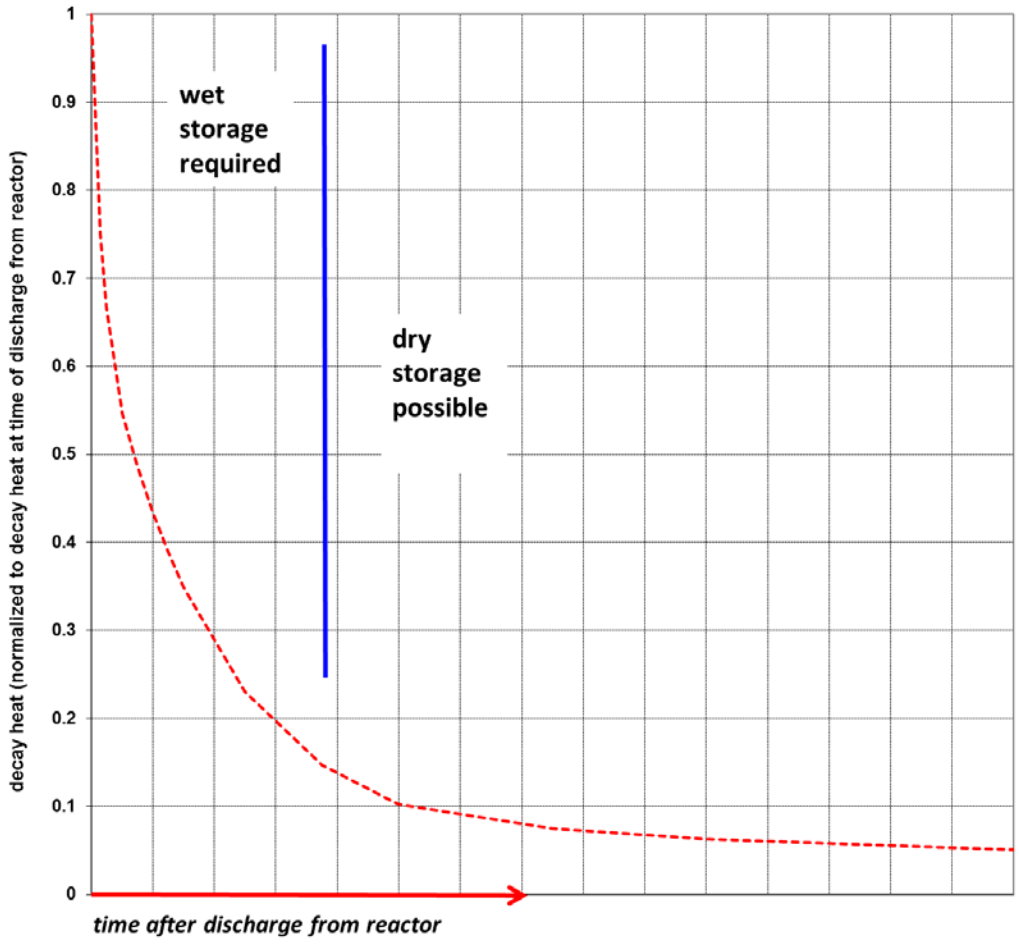

Figure 2-1. Illustration of Time to Reach Decay Heat Level Where Dry Storage is Possible

A storage module, in conjunction with a dry storage canister that contains the fuel assemblies, is licensed for a specific maximum design basis total decay heat load and maximum per-assembly decay heat load. For systems that permit preferential loading of the canister (i.e., not all assemblies at the same or nearly the same decay heat load), the maximum per-assembly heat load varies by location within the canister. The maximum decay heat load in canisters with uniform loading is typically 1 kW or less for pressurized water reactor (PWR) fuel, and 0.4 kW or less for boiling water reactor (BWR) fuel, for both horizontal and vertical storage systems. With preferential loading of fuel assemblies in the dry storage canister, which is a design feature of some advanced storage system designs (such as NUHOMS® HSM-H for horizontal storage and HI-STORM100 for vertical storage), the maximum design-basis loading can approach 1.5 to 2.0 kW per assembly for PWR fuel, and up to 1 kW per assembly for BWR fuel. However, for these preferentially loaded canisters, fewer than half of the total number of assemblies in the canister can be at the maximum decay heat value, while the remainder must have much lower decay heat values, to bring the total decay heat load within licensed limits. For example, a canister that is allowed to have up to a third of its assemblies at 1.5 kW might be allowed no more than 0.5 kW per assembly for the remaining two-thirds of its assemblies, within the constraints of design basis maximum decay heat loading.

Given these thermal design basis limits for storage systems, and also the conservative practice of loading dry storage systems at no more than ~60% of design basis capacity, the higher the burnup of a given fuel assembly, the longer it is likely to be in wet storage before being transferred to dry storage. Fuel with very low burnup, (<25 GWd/MTU) may be eligible for dry storage 3-5 years after discharge from the reactor. More typically, fuel with burnup in the range 35-45 GWd/MTU might be cool enough for dry storage 10 to 20 years after discharge, depending on the capacity of its destination dry storage system. With more aggressive loading practices, some higher burnup fuel (>45 GWd/MTU) might be transferred to dry storage after only 10 to 15 years in wet storage, but much of it is likely to reside at least 25 to 30 years in the pool before it is transferred to dry storage. Some of the most highly enriched, high burnup fuel can be expected to have even longer cooling times (on the order of 30 to 50 years) in wet storage before transfer to dry storage. However, it must be noted that these times are estimates only, and actual cooling time for an assembly depends on the storage system configuration, maximum licensed decay heat load, and whether zoned or uniform loading is implemented

Figure 2-2 and Figure 2-3 illustrate the relationship between assembly burnup and required minimum cooling time before the assembly would be allowed in a typical horizontal dry storage system. The horizontal lines in the plots in these two figures correspond to the design-basis maximum initial decay heat values for dry storage systems. These two figures are illustrative only, as the actual decay heat curves used in detailed analysis of dry storage conditions for a specific system depend on the particular fuel assembly types to be stored, their initial enrichment, and their in-reactor exposure history. However, these plots show the general behavior of decay heat as a function of burn-up for spent fuel assemblies. Curves for burnup values above 62 GWd/MTU would have similar shapes, but would lie increasingly farther to the right on these plots; that is, with longer time after discharge before crossing the horizontal lines corresponding to maximum initial decay heat values permitted in dry storage .

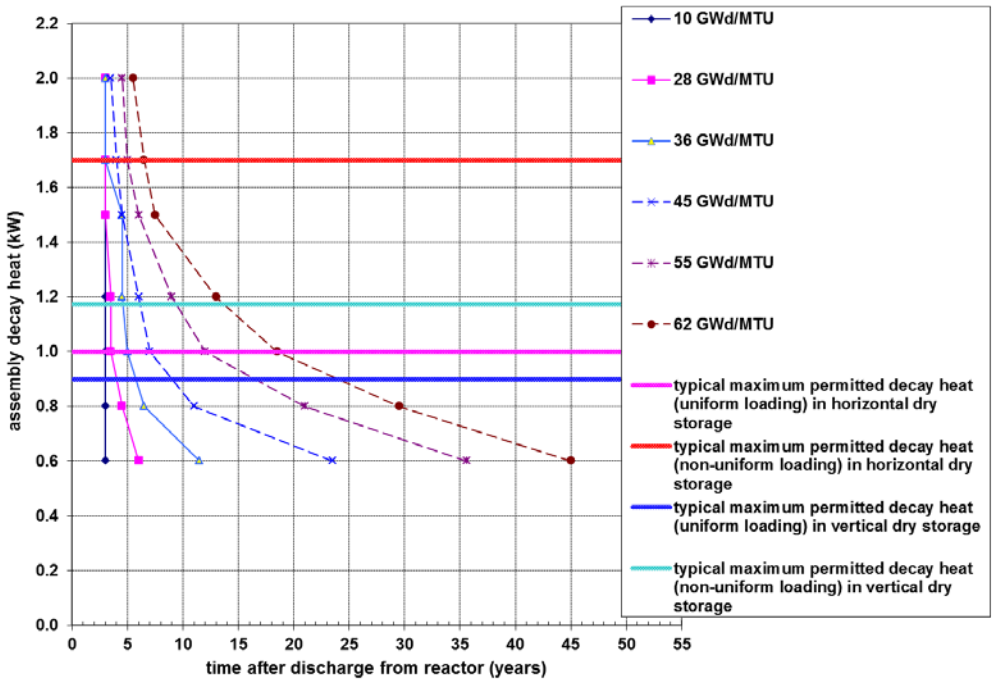

Figure 2-2. Representative Decay Heat for PWR Fuel Assemblies as a Function of Burnup Compared to Maximum Permitted Decay Heat per Assembly in Dry Storage Systems

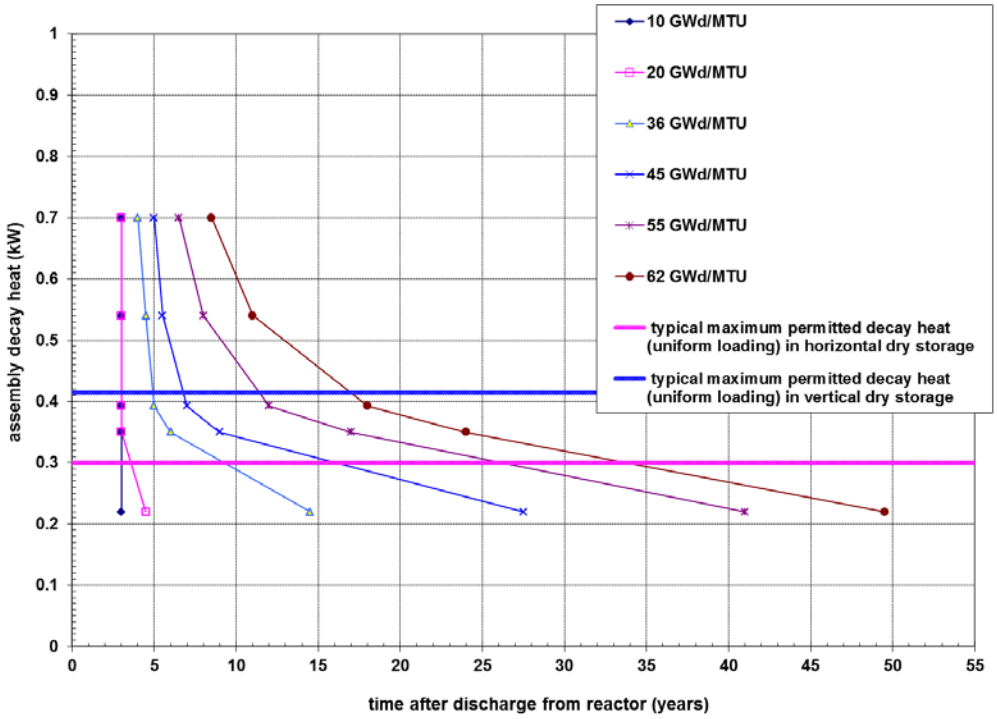

Figure 2-3. Representative Decay Heat vs. Time for BWR Fuel Assemblies as a Function of Burnup Compared to Maximum Permitted Decay Heat per Assembly in Dry Storage Systems

As an illustrative example of fuel cladding and component temperatures over time in extended storage, two advanced, high-capacity storage modules, one horizontal and one vertical, were analyzed for the design-basis maximum initial decay heat loading. Analyses were also performed with decay heat values representing the initial loading projected out to 300 years. The horizontal storage module evaluation was performed using a Star-CD (CD-adapco Group, 2004) model of the NUHOMS® HSM-H containing a 32PTH1 dry storage canister (DSC) at design-basis thermal loading and two postulated lower, more typical loading conditions. The vertical storage module evaluation was performed using a COBRA-SFS (Michener et al., 1995) model of the HI-STORM 100 system containing an MPC-32 dry storage canister at design-basis loading for the non-uniform loading configuration permitting the highest assembly decay heat load.

For the fuel assemblies in the 32PTH1, the decay heat curves were projected assuming that the canister contained WE 14x14[a] fuel at 62 GWd/MTU, with a nonuniform basket loading configuration allowing 40.8 kW for the initial total decay heat load. This is the maximum design basis decay heat load for this horizontal system. Calculations were also performed assuming more typical initial decay heat loads of 22 kW and 12 kW (~55% and ~30% of design basis, respectively), to evaluate the sensitivity of results to initial conditions. For the fuel assemblies in the MPC-32, the decay heat curves were projected assuming that the canister contained WE 17x17 OFA[b] at 62 GWd/MTU, with a non-uniform loading configuration corresponding to the largest permitted per-assembly decay heat load, allowing 30.2 kW initial total decay heat load. Figure 2-4 shows the total decay heat loadings assumed for these canisters, projected out to 300 years.

The curves in Figure 2-4 show two characteristics that are particularly relevant to detailed thermal analysis of extended storage conditions. First, the largest fraction of the decrease in decay heat load occurs in the first 50 years of storage. In this example, the projected decay heat load values decrease by 50%-60% in this time period. Second, after about 150 years, the rate of decrease in the decay heat load amounts to only a few percent per century. This suggests that the greatest temperature changes will occur in the first 50 to 100 years of storage, regardless of the initial starting point for any particular canister and fuel loading.

For the purposes of this analysis, the ambient conditions were treated as constant in time for the entire 300 year period, at 38°C (100°F) for the horizontal storage module and 27°C (80°F) for the vertical storage module. These values are based on “hot normal conditions of storage” as defined in current licensing evaluations for these systems. Calculations at each projected decay heat value at specified points in time out to 300 years were performed assuming steady-state conditions. Given the large thermal mass of these systems, and the relatively slow rate of change of decay heat load with time, this approach gives a reasonable approximation of conditions at the corresponding time in the long cooldown transient of the system.

[a] This is the design basis fuel for thermal analysis of the 32PTH1. The high burnup may be unrealistic for this fuel, but the assumption was made in order to obtain bounding decay curves for extended storage.

[b] This is the limiting fuel configuration for the MPC-32.

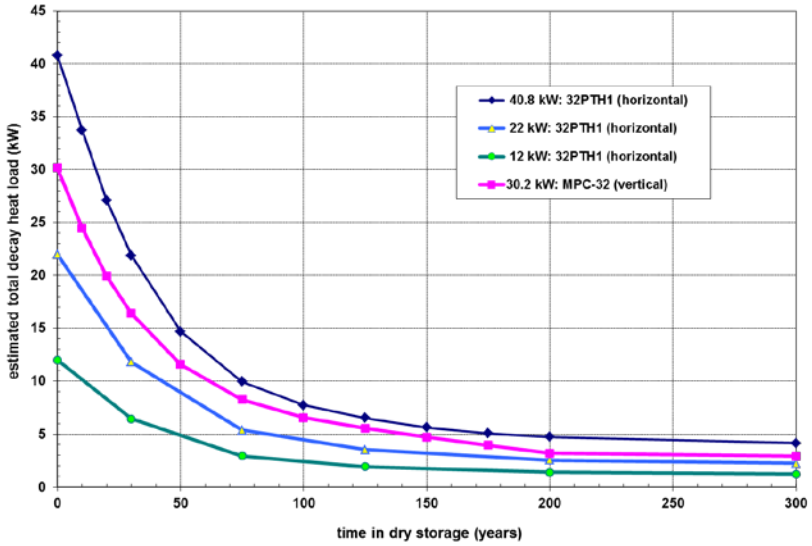

Figure 2-4. Estimated Decay Heat Projections in Dry Storage for 300 Years

2.1 Temperatures in Horizontal Storage

The peak fuel cladding temperature is generally the temperature of greatest interest in dry storage for initial loading of the canister. Figure 2-5 shows the response of this component temperature to the projected decay heat load decrease over time, for the range of initial decay heat loadings evaluated. As might be expected, these temperature curves mimic the decreasing decay heat curves in Figure 2-4. After about 150 years, the peak clad temperature is predicted to decrease by only a few degrees per century.

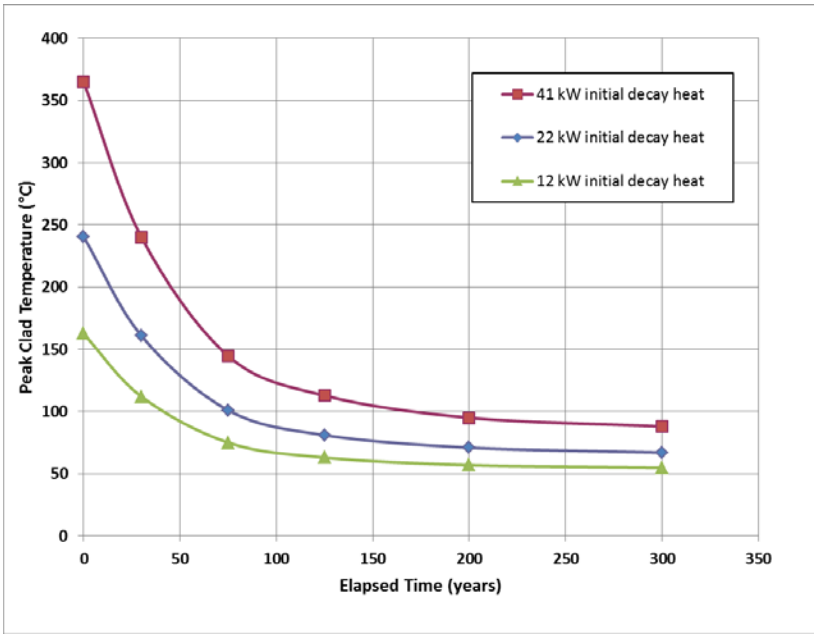

Figure 2-5. Peak Clad Temperature Predictions for Projected Decay Heat Decrease over Time in Horizontal Storage

The temperature distributions within the canister can be as important as the peak temperatures in assessing the long-term behavior of the system. Because most of the heat is removed radially from the canister (that is, perpendicular to the long axis of the canister), radial temperature distributions give the most informative picture of temperature gradients within the system. Within the canister, the temperature gradients are determined mainly by the loading pattern of the fuel assemblies, the basket design, and the support structures used to position the basket within the canister. The actual shape of the distributions will vary considerably from canister to canister, depending on decay heat loading and basket design, but the general behavior seen in horizontal systems is well illustrated by the graph in Figure 2-6, showing the radial temperature distribution through the canister, on a line passing through the fuel assemblies in the central region of the basket. This profile is taken at the axial location of the peak fuel cladding temperature, and traces the temperature from the lower surface of the horizontal canister, through the support structures and fuel assemblies, to the upper surface of the canister.

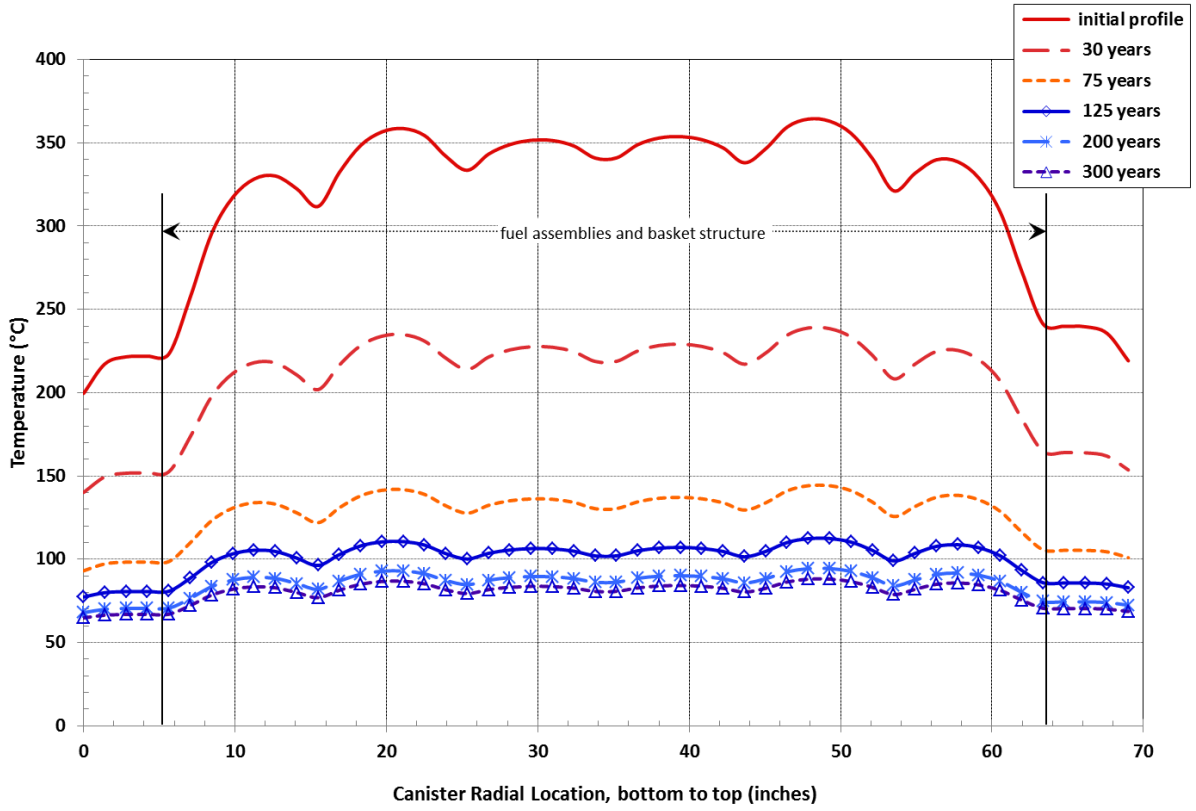

Figure 2-6. Radial Temperature Distribution through the Canister at the Peak Clad Temperature Location for Projected Decay Heat Decrease over Time in Horizontal Storage

In this example, the nonuniform loading pattern of the assemblies results in lower temperatures on the fuel cladding surfaces of rods near the center of the canister. The highest peak cladding temperature and the steepest radial temperature gradients occur in the fuel assemblies on the periphery of the basket. As with the peak cladding temperature histories illustrated in Figure 2-5, the temperature profiles show the largest decreases in the first 100 years of storage, and after

that, the rate of decrease is much slower. The overall gradient at a given point in time shows increased flattening with increased time in storage, as well.

The axial distribution of temperatures in the canister tends to be relatively flat over the length of the active fuel region, with relatively steep roll-off at the ends. This is due primarily to the relatively flat burnup profile of spent fuel, which is what determines the decay heat profile. In addition, very little heat is removed from the ends of the canister, due to module geometry and other design constraints that result in much more limited heat transfer paths in the axial direction, relative to the radial direction. This is illustrated in Figure 2-7, showing the cladding surface temperature distribution axially along the hottest fuel rod in the hottest assembly. All other fuel rods in the canister have similar profiles, at reduced peak values (corresponding to the radial distribution of peak temperature values illustrated in Figure 2-6.)

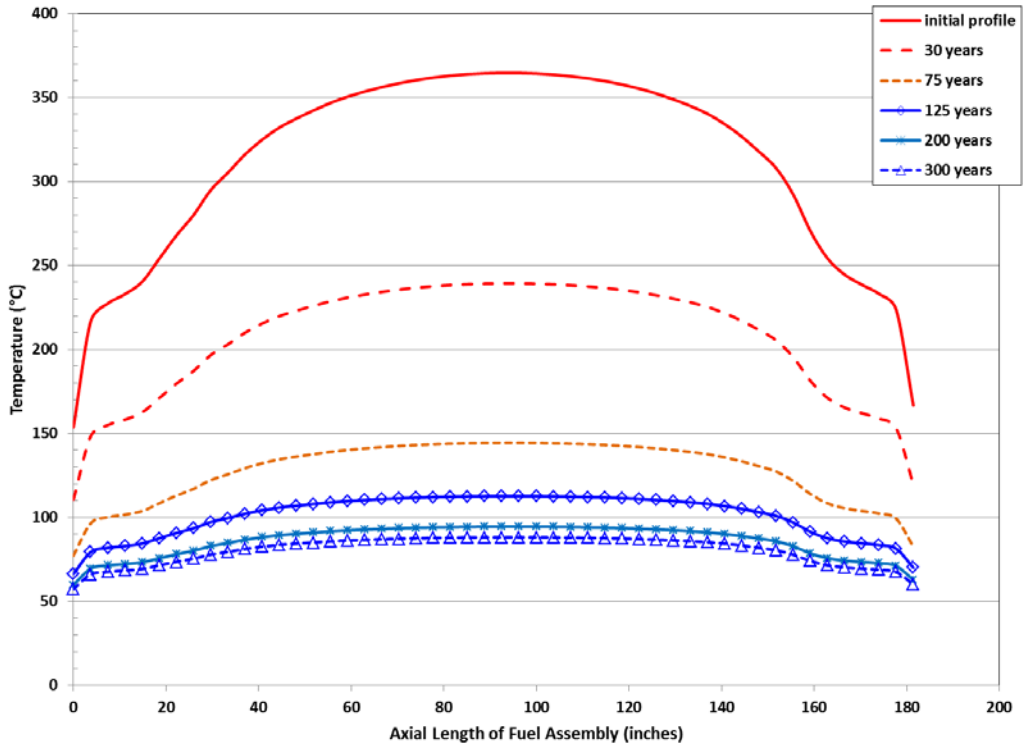

Figure 2-7. Axial Temperature Distribution on the Hottest Rod Cladding Surface, for Projected Decay Heat Values over Time in Horizontal Storage (Initially at 40.8 kW)

The curves in Figure 2-7 show that axial temperature profiles on the hottest components in the system (i.e., the fuel rods) flatten out as temperatures decrease with time, as gradients flatten in the axial as well as the radial direction. The curves in Figure 2-8 show a corresponding flattening of the axial temperature distribution on the canister outer shell surface at the location of the peak outer shell temperature (along the top of the canister). These curves are for the case with initial decay heat at the design basis value of 40.8 kW. Similar plots of results from the cases with lower initial decay heat values would show the same trends, but with temperature values of correspondingly lower magnitude.

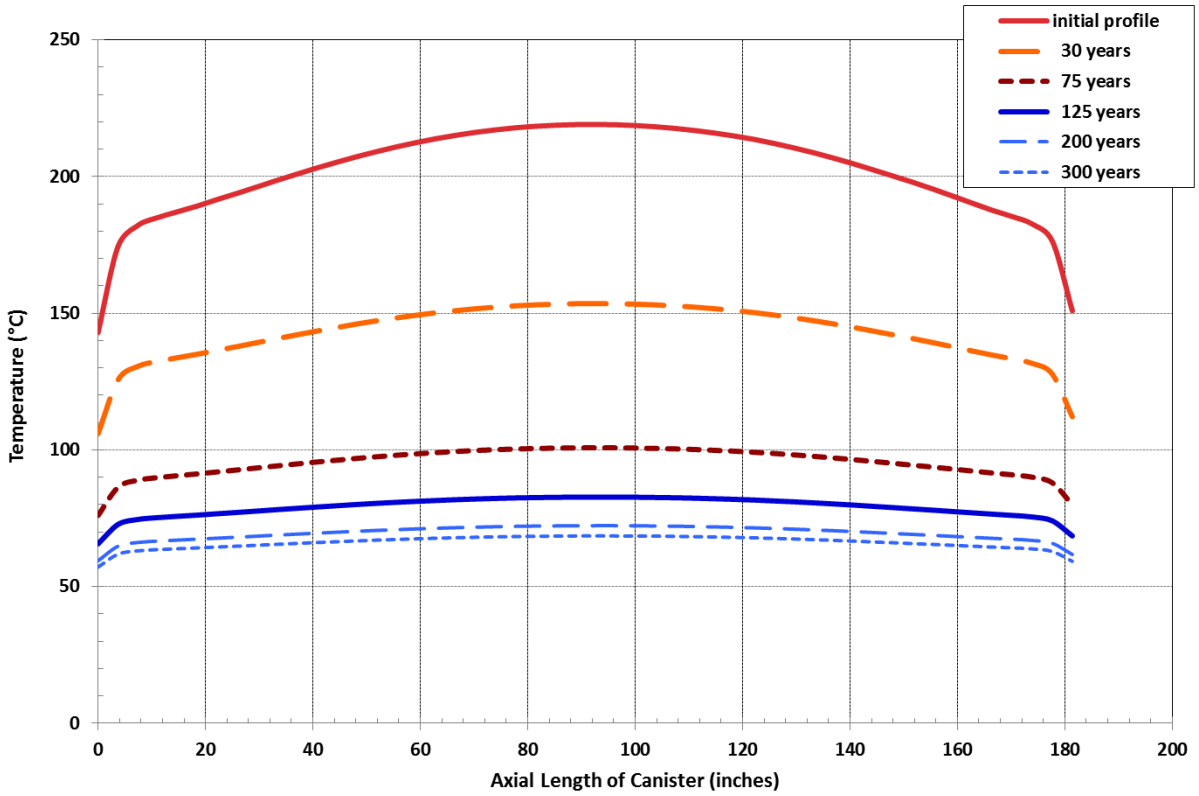

Figure 2-8. Axial Temperature Distribution at the Canister Shell Surface along the Top, for Projected Decay Heat Values over Time in Horizontal Storage (Initially at 40.8 kW)

2.2 Temperatures in Vertical Storage

The temperatures and temperature distributions in vertical storage systems are comparable to those predicted for horizontal storage systems at similar decay heat loads, but with some significant differences. The gradients tend to be somewhat steeper, and the peak component temperatures somewhat lower, due to the generally greater efficiency of free convection from a vertical cylinder compared to that from a horizontal cylinder. Figure 2-9 shows the response of the peak component temperatures to the projected decay heat load decrease over time for vertical storage. As with the results for horizontal storage shown in Figures 2-5 through 2-8, these temperature curves reflect the corresponding decreasing decay heat curve in Figure 2-4 for this system.

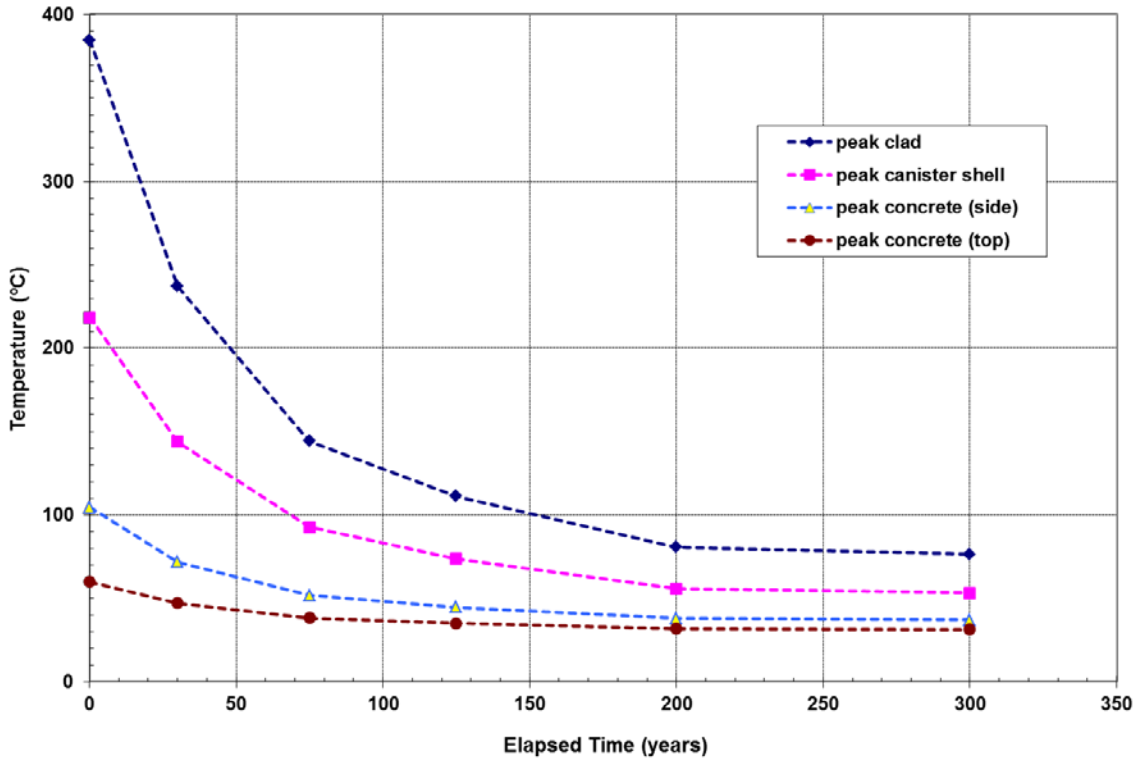

Figure 2-9. Peak Component Temperature Predictions for Projected Decay Heat Decrease over Time in Vertical Storage

Storage canisters in the HI-STORM100 are typically pressurized with helium at 7 to 9 atm, to obtain enhanced heat removal rates for internal convection in the thermo-syphon recirculation that occurs in this vertical canister design due to the internal basket structure, which includes open channels for downflow between the basket and the canister shell. The enhanced heat removal at higher internal pressures is due to the increased density of the helium gas within the canister, and is not a function of the pressure, *per se*. As temperatures in the system decrease over time, the pressure will also decrease, following the ideal gas law, but because this is a closed container, the average gas density will remain constant, and the effect of enhanced convection will persist.

It can be readily demonstrated from the physics of gas behavior and flow hydrodynamics that the enhancement of convection heat transfer due to increased gas density is significant for density increases corresponding to only about 5 atm pressurization in this canister design. Therefore, design basis analyses for this system assume canister pressure of only 5 atm for thermal evaluations, even if the actual initial pressurization of the system at loading may be somewhat higher.

It seems rather unlikely that the helium gas density in the MPC would remain unchanged for 300 years, but evaluation of canister failure modes is beyond the scope of the current analysis. This was also the implicit assumption in the evaluations for the horizontal storage module, presented in the previous section, which was assumed to maintain a helium atmosphere within the 32PTH1

DSC for 300 years. For consistency of the comparison, the calculations presented here assume that the average helium gas density remains at its initial value in the MPC-32 and in the 32PTH1 throughout the 300-year time span considered.

The estimated radial temperature distributions for the vertical system at the axial location of the peak fuel temperature are illustrated in Figure 2-10. (For clarity of presentation, the curves in this plot show the system only in half-symmetry, from the canister centerline to the outer wall of the overpack.) As in the case of the horizontal system, the steepest temperature gradients in the vertical system also occur in the peripheral fuel assemblies, and the temperature profiles show the largest decreases in the first 100 years of storage. Subsequently, the rate of decrease is much slower and the overall gradients show increased flattening with time, due to the decreasing decay heat load.

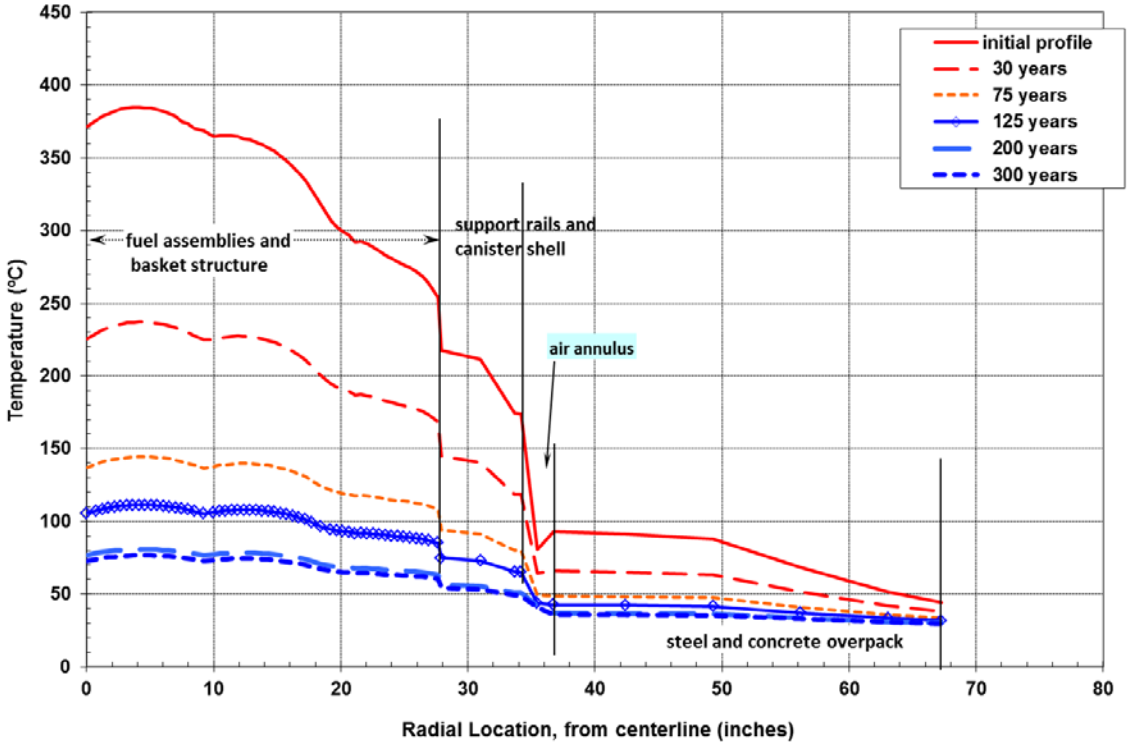

Figure 2-10. Radial Temperature Distribution through the Canister and Overpack at the Peak Clad Temperature Location for Projected Decay Heat Decrease over Time in Vertical Storage

The change in axial temperature profiles within the canister over time in storage is illustrated in Figure 2-11, showing the axial temperature profile on the hottest fuel rod in the system. The change in temperature with time on the external surface of the canister is shown in Figure 2-12 These profiles are somewhat different in shape from those obtained for the horizontal canister, due to differences in natural convection behavior between the two systems (compare Figures 2-11 and 2-12 to Figures 2-7 and 2-8, respectively). However, the overall pattern of decreasing peak temperature with time is essentially the same. As with the radial profiles, the axial profiles decrease in magnitude as the decay heat decreases with time, but because of the vertical

orientation of the canister, the axial gradients tend to remain steeper than in the horizontal system.

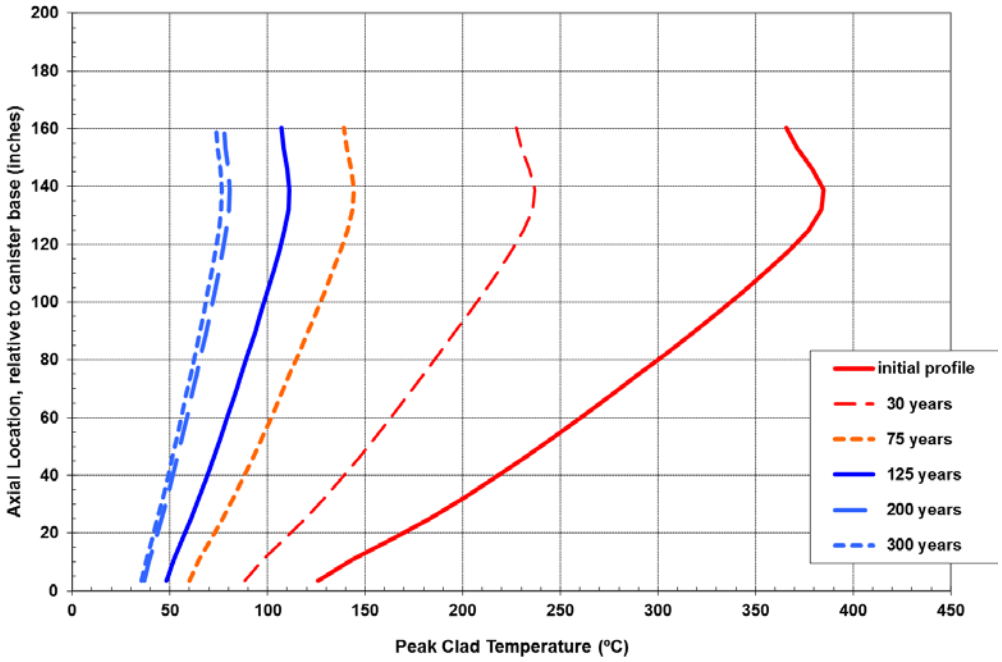

Figure 2-11. Axial Temperature Distribution on the Hottest Rod, for Projected Decay Heat Decrease over Time in Vertical Storage

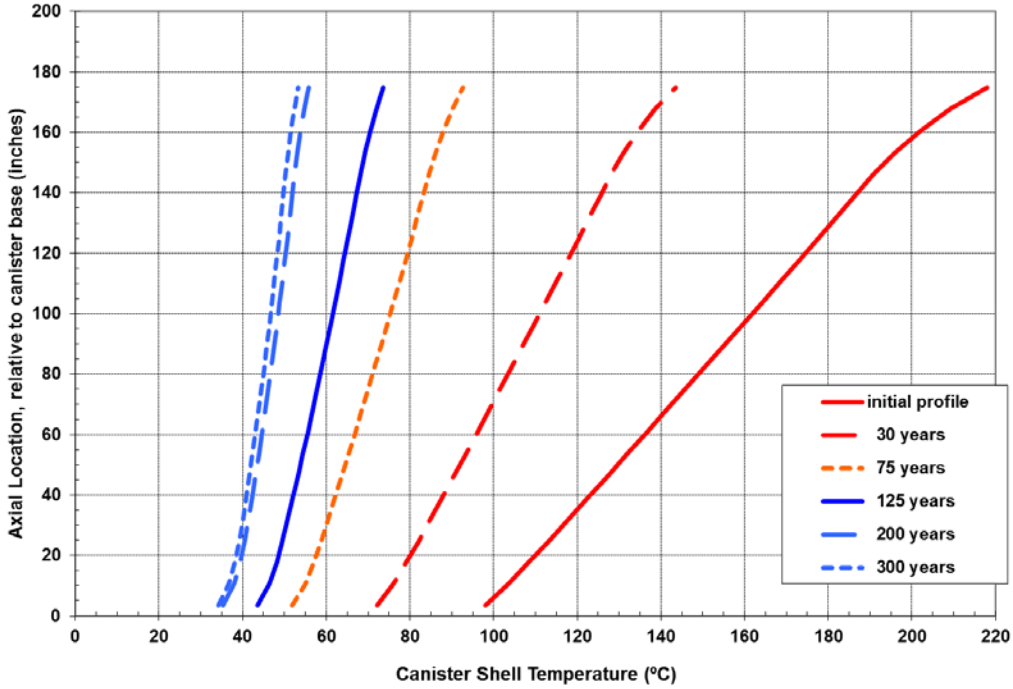

Figure 2-12. Axial Temperature Distribution at the Canister Shell Surface for Projected Decay Heat Decrease over Time in Vertical Storage

2.3 Implications for Storage of High Decay Heat Fuel Assemblies

The results of this preliminary study provide insight into the maximum temperatures and temperature distributions that would be expected in horizontal and vertical systems for extended storage of used nuclear fuel. The results are based on maximum design basis decay heat loading for advanced systems that are designed to operate at the highest decay heat loads licensed to date (i.e., as of 2013.) The highest decay heat loads in these systems are achieved only with non-uniform loading configurations, in order to meet thermal performance requirements (e.g., peak clad temperature below 400°C).

These systems therefore can store only a limited number of assemblies at the highest per-assembly decay heat loads that are currently permitted in dry storage (typically one-half to one-third of the total number that can be loaded into the canister, at up to 1.5 to 1.8 kW per assembly). The remainder of the assemblies in the same canister must be at much lower decay heat values, to be within design-basis total decay heat load limits. These maximum thermal limits and loading pattern constraints apply to all types of fuel assemblies that may be loaded in these systems, whether of low, intermediate, or high burnup. If a canister were to store only high burnup fuel, some 10 or 12 of the assemblies could be relatively 'young', perhaps less than 15 years in the pool, and therefore at or near the highest permitted per-assembly decay heat values. The remaining 20 or so assemblies in the canister would have to be much older, perhaps as much as 25 years or more in the pool, to be at the required lower per-assembly decay heat values permitted for the licensed loading configuration. If canisters of these advanced designs are allowed to contain assemblies with a range of burnup values, possibly including low, intermediate and high burnup assemblies in the same canister, the assemblies could span a relatively large range of ages to achieve the maximum permitted total decay heat loading.

The calculations for these design basis systems assume that the configuration of the system (other than the decay heat load) is maintained unchanged from initial conditions indefinitely. The evaluations presented in the following sections consider the potential effects of uncertainties and variability as well as departures from nominal conditions in an actual operating system due to postulated age-related changes in the system that could affect thermal performance.

3. EVALUATION MODEL FOR SENSITIVITY STUDIES

The sensitivity evaluations were performed using the STAR-CCM+ (CD-adapco, 2012) model developed for module HSM15 in the Calvert Cliffs ISFSI, for pre-inspection and post-inspection thermal modeling in support of the site inspection in June 2012 (see Suffield et al., 2012). This storage module contains a 24P dry shielded canister (DSC) loaded with twenty-four CE 14x14 spent fuel assemblies. The total decay heat load for the DSC in HSM15 was 10.58 kW at the time of loading, corresponding to approximately 12 years in wet storage. At the time of inspection (June 2012), after approximately16 years in dry storage, the total decay heat in the canister was calculated to be 7.58 kW. The decay heat load for this canister was projected to 300 years, and evaluations were performed for 6 kW, 4 kW, and 2 kW, corresponding to fuel approximately 50 years, 100 years, and 300 years old, respectively. Table 3.1 lists the different decay heat values. All simulations were run assuming an ambient temperature of 27.8°C (82°F).

Table 3-1. Range of Total Canister Decay Heat Values

Heat Decay Value (kW)	Conditions/ Time
10.58	At-loading conditions, after ~12 years in wet storage
7.58	At time of inspection, after ~16 years in dry storage (~27 years after discharge)
6	After ~38 years in dry storage (~50 years after discharge)
4	After ~88 years in dry storage (~100 years after discharge)
2	After ~288 years in dry storage (~300 years after discharge)

Section 3.1 presents a detailed description of the STAR-CCM+ model of HSM15. This section contains information from the primary reference for the inspections at the Calvert Cliffs ISFSI, and is repeated here for completeness in the description of the sensitivity evaluations. Section 3.2 describes the fuel effective conductivity model used to represent the fuel assemblies in this model, with variations for the specific cases developed for the various sensitivity studies.

3.1 STAR-CCM+ Model of HSM15

The mesh for the model is composed of 43 separate regions connected by 117 interface boundaries, resulting in a single conformal volume mesh across all regions. The polyhedral volume mesh of the HSM15 assembly contains 21,536,624 cells, 127,598,563 faces, and 106,295,728 vertices. Along each wall/fluid interface, the mesh contains a prism layer to improve the accuracy of the flow solution near the walls. The prism layer consists of orthogonal prismatic cells, two cells thick, adjacent to the wall boundaries. Figure 3-1 shows an exterior view of the overall volume mesh of the HSM15 assembly. The interior mesh, including the 24P DSC within HSM15, is illustrated in Figure 3-2 with an axial slice along the central midplane of the structure. Figure 3-3 shows the mesh for a transverse slice through the module near the middle of the axial length of the DSC. The mesh within the 24P DSC and in the region of the airflow path around the DSC is highly resolved, to appropriately capture temperature and

velocity gradients. In the concrete walls and in airflow regions far from the DSC, where gradients are less extreme, a coarser mesh is used, for computational efficiency.

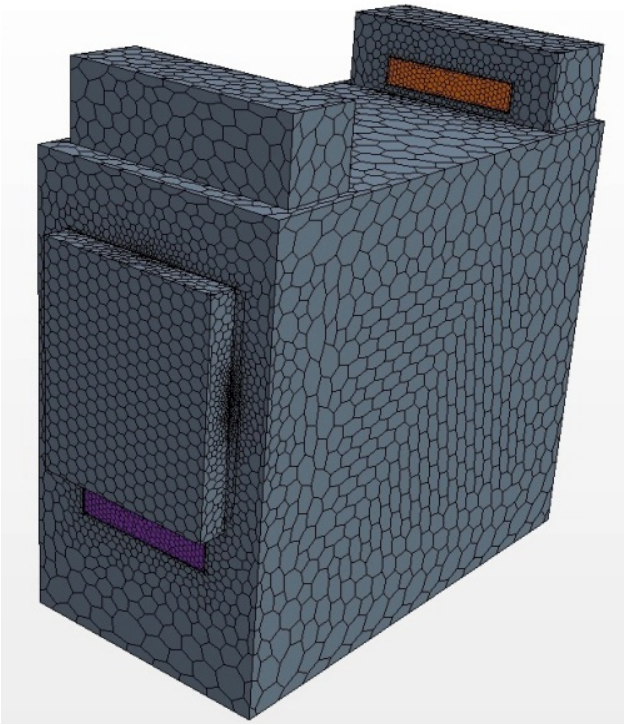

Figure 3-1. Volume Mesh of HSM15 Assembly: Exterior View

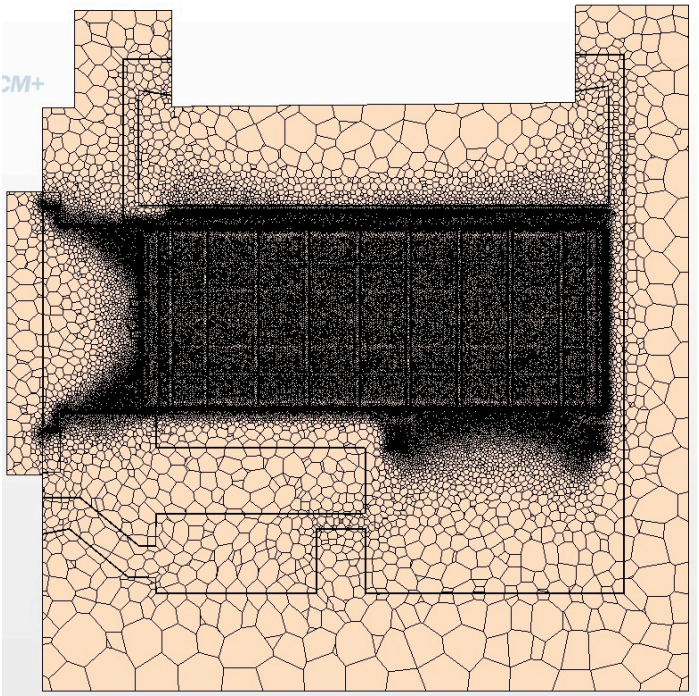

Figure 3-2. Planar Slice Through Centerline Showing Volume Mesh of HSM15 and 24P DSC Model in Axial Direction

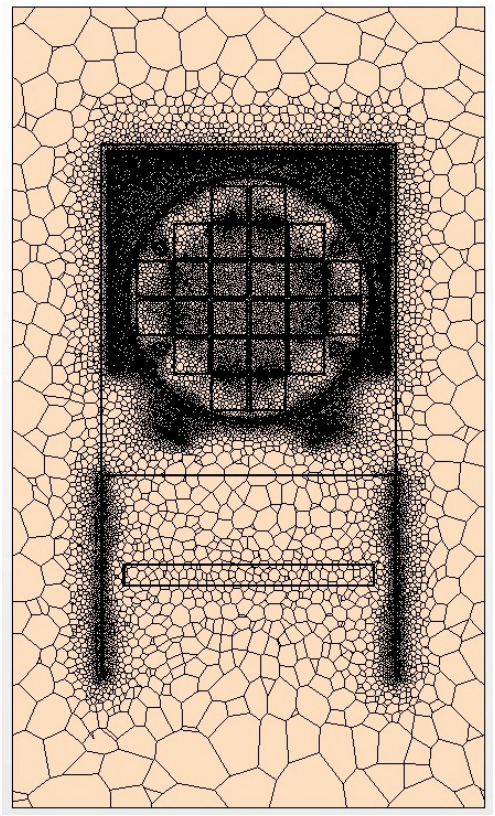

Figure 3-3. Planar Slice Through Mid-line Showing Volume Mesh of HSM15 and 24P DSC Model in Transverse Direction

The fuel assemblies within the DSC were represented as homogeneous solid regions using the fuel effective conductivity model. In order to reduce the complexity of the mesh, a nonconformal mesh was applied to the thin steel guide sleeves that surround the fuel assemblies. The support disks and tie rods were represented as solid material elements with appropriate thermal and material properties. Figure 3.4 illustrates the geometry of the fuel assemblies, guide sleeves, support rods, and support disks within the DSC. The helium gas backfill within the DSC was represented as a gas region between the support disks and external to guide sleeves.

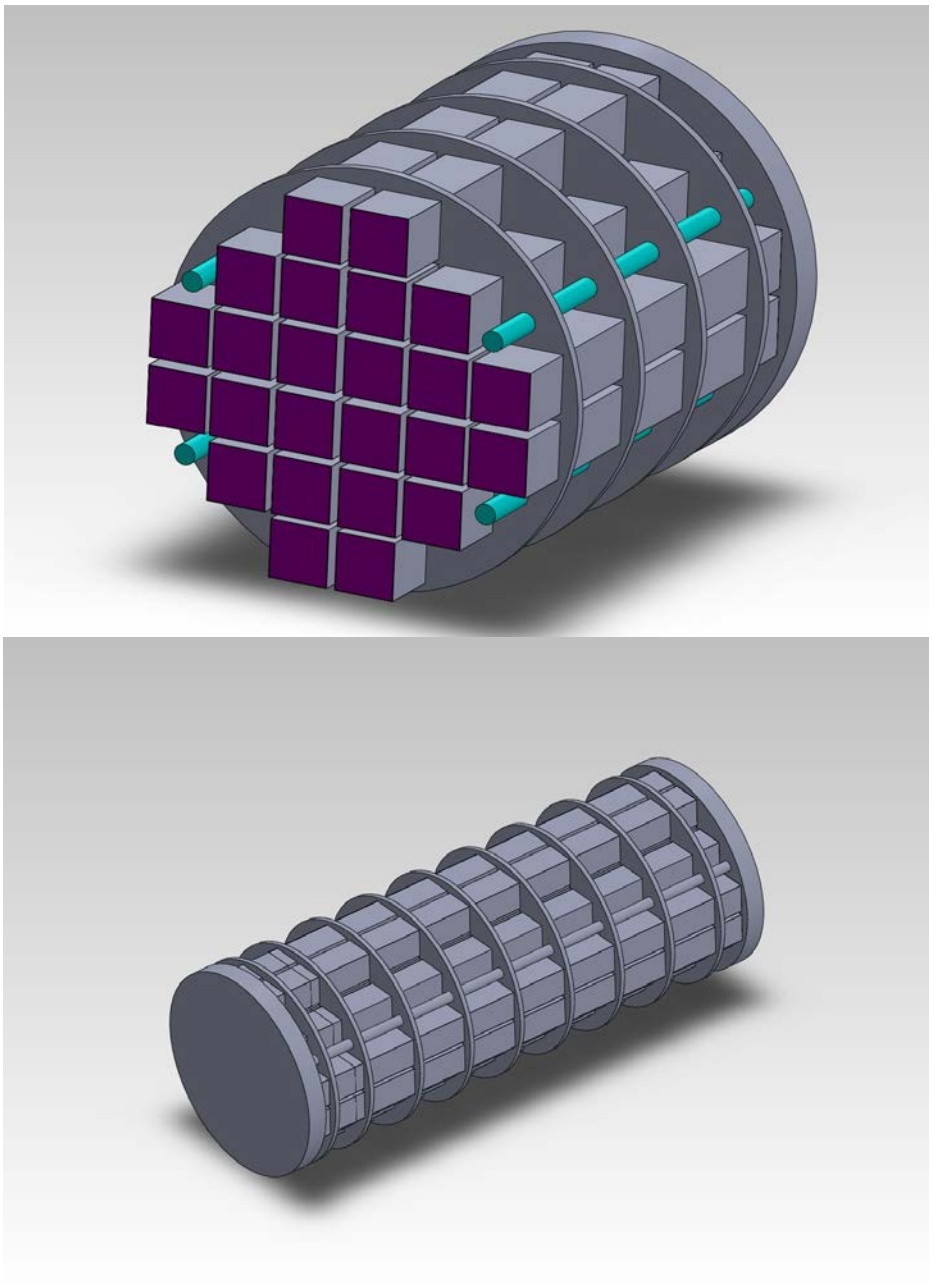

Figure 3-4. Mid-Plane Cross-Sectional View and Exterior View of Internal Geometry in STAR-CCM+ Model of 24P DSC

3.2 Fuel Effective Conductivity Model

The 24P DSC in HSM15 contains twenty-four CE14x14 spent fuel assemblies discharged from the Calvert Cliffs plant at the end of various cycles from 1982 to 1987. In the STAR-CCM+ model of this system, the active fuel length of each fuel assembly was modeled using a homogeneous effective conductivity representing CE 14x14 fuel assemblies with helium backfill gas within a fuel storage compartment of a 24P DSC. The fuel assembly effective conductivity in the radial direction is determined with the modeling approach (Sanders et al. 1993; Bahney and Lotz, 1996) typically used in spent fuel thermal evaluations using CFD or finite element

analysis (FEA) codes for storage and transportation systems. This approach is used because accurate and complete computational modeling of the heat transfer in a spent fuel assembly with a CFD code such as STAR-CCM+ (or an FEA code such as ANSYS) requires extremely detailed resolution to properly capture the local temperature gradients and energy exchange due to the different modes of heat transfer involved. Figure 3-5 shows an example of a typical model of a quarter-section of a spent fuel assembly developed for ANSYS, which illustrates the complexity of the mesh required. Constructing such a mesh for an entire canister of fuel assemblies (24 full assemblies, in this case) is obviously an untenable approach, even with modern computational resources.

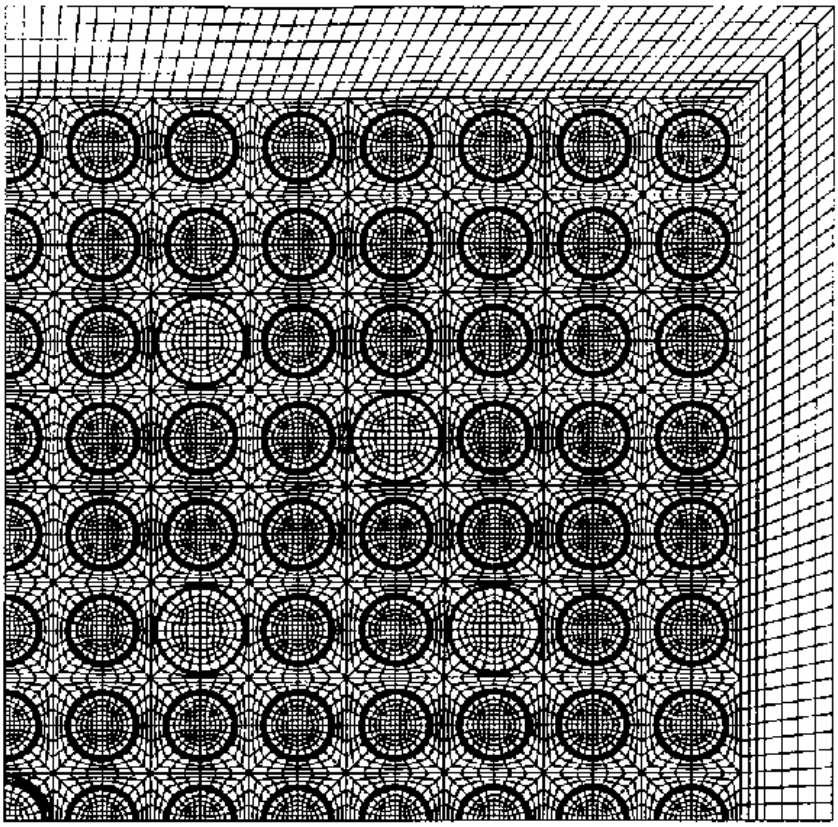

Figure 3-5. Illustration of Typical Computational Mesh for Detailed CFD or FEA Model of Quarter-Section of a Spent Fuel Assembly for Determining Effective Conductivity

The k-effective model was developed to allow a much simpler representation of a spent fuel assembly within a fuel compartment by treating the entire spent fuel rod array and the surrounding fill gas within the confines of the compartment as a homogenous solid material. The fuel rod assembly and surrounding gas are modeled with an effective conductivity that is designed to yield an overall conduction heat transfer rate that is equivalent to the combined effect of local conduction and radiation heat transfer in a plane through the assembly. The basic approach used to develop the k-effective model assumes that convection heat transfer within the fuel assembly is negligible, which is generally the case with a horizontal canister, such as the 24P in HSM15. Axial conduction is also neglected in this model. It is also assumed that the heat generation rate can be treated as uniform throughout the volume of the fuel compartment

enclosing the fuel rod assembly. This is generally a reasonable assumption for spent fuel assemblies.

With these simplifying assumptions, radial heat transfer in the cross-section of the storage compartment containing an individual fuel assembly can be represented with the steady-state heat conduction equation for a solid material with uniform heat generation;

$$\frac{\partial^2 T}{\partial x^2} + \frac{\partial^2 T}{\partial y^2} + \frac{Q}{k_{eff}} = 0$$

where T = temperature field over the homogeneous cross-section
Q = assembly decay heat load
k_{eff} = effective thermal conductivity of the homogeneous region for decay heat load Q

For uniform heat generation and uniform boundary temperatures in the *x* and *y* directions (defining the origin at the center of the assembly), this partial differential equation can be solved directly using Fourier analysis. This yields a two-dimensional temperature field for the homogeneous cross-section representing the fuel assembly within the fuel compartment. A textbook source (Carslaw and Jaeger 1986) is given for this solution in the model's primary documentation, but the same result can be found in almost any advanced heat transfer text. The solution to the partial differential equation for this particular application to a fuel assembly cross-section can be expressed as

$$T(x,y) = q''' \frac{a^2 - x^2}{2k_{eff}} - 16q''' \frac{a^2}{k_{eff}\pi^3} \sum_{n=0}^{\infty} \frac{(-1)^n \cos\left(\frac{(2n+1)\pi x}{2a}\right) \cosh\left(\frac{(2n+1)\pi y}{2a}\right)}{(2n+1)^3 \cosh((2n+1)\pi / 2)}$$

where

$T(x,y)$ = temperature field over the homogeneous cross-section
k_{eff} = effective thermal conductivity of the homogeneous region for decay heat load yielding heat generation rate q'''
a = distance from the center of the rod array to the wall
q''' = uniform heat generation rate due to assembly decay heat load Q distributed over the homogeneous volume, V_h
where $V_h = (2a)^2 L_a$
with L_a = active fuel length for the assembly

Because of the strong divergence of the *cosh* function, the summation term in the above equation for the temperature field reduces to a simple constant at the location (0,0), which in this case corresponds to the physical center of the assembly cross-section. Therefore, the center temperature for the homogeneous region is given by

$$T(0,0) = q''' \frac{a^2}{k_{eff}} (0.2957)$$

For a uniform boundary temperature at the wall and a uniform heat generation rate (defined in terms of the assembly decay heat load over the total axial length of the active fuel), the effective thermal conductivity can be expressed as,

$$k_{eff} = 0.2957 \frac{Q}{4L_a(T_c - T_{wall})}$$

where Q = total decay heat load in the assembly
L_a = active fuel length for the assembly
T_c = peak (center) temperature of homogeneous cross-section
T_{wall} = uniform wall temperature

The k-effective model is therefore simply a specialized solution of the 2-D conduction equation that relates heat generation and fuel compartment wall temperature to the peak temperature in a spent fuel assembly. In a purely conduction problem, the thermal conductivity of the material is generally a quantity known from experimental measurement. In this application to spent fuel assemblies, where the heat transfer consists of conduction and radiation through an array of different materials (i.e., the fuel, fuel rod cladding and the fill gas), it is not generally possible to obtain experimental measurements of the effective conductivity of the assembly. However, virtual 'measurements' of the total heat transfer rate in an assembly as a function of boundary conditions can be obtained with an extremely detailed model of the assembly similar to that illustrated in Figure 3-5 above using a CFD or FEA code, or more easily with a detailed rod-and-subchannel model of the assembly, using the COBRA-SFS code.

A computational database generated in this manner can be used to calculate the effective thermal conductivity for the assembly, using the above relationship for k_{eff}. This yields an array of values of k_{eff} versus wall temperature, peak clad temperature, and decay heat load for the particular assembly design and fill gas. The k_{eff} values generated for one set of conditions are not generally applicable to different heat loads or fill gas, even for the same fuel design, and a separate computational database must be generated for each combination of fuel design, decay heat load, fuel compartment configuration, and fill gas.

The k_{eff} values in the computational database for a given fuel design and decay heat load are defined in terms of two temperatures; the peak clad temperature and the wall temperature. What is actually needed in application of the k-effective model, however, is a way to specify k_{eff} as a function of a single local mesh temperature, so that it can be treated as a temperature-dependent material property. This is accomplished by the simple expedient of tabulating the computed k_{eff} values in terms of the bundle average temperature T_b, defined as the average of the peak clad temperature T_{pc} and the uniform compartment wall temperature T_{wall}; that is,

$$T_b = (T_{pc} + T_{wall})/2$$

This average temperature is treated as a convenient surrogate for the temperature difference that is actually used in the model to define the effective conductivity for the bundle. The result is a temperature-dependent relationship for the effective conductivity that can be specified as a thermal property of the homogeneous material representing the fuel assembly within the storage compartment. The application also implicitly ignores any effect of non-uniform temperature distribution on the compartment walls surrounding the fuel assembly. The relationship is typically applied as a function of the local element or node temperature within the homogeneous region, rather than the bundle average temperature, since the bundle average temperature is not generally a computational variable in thermal or thermal-hydraulic analysis codes. This is a further simplification of the model, but in general is conservative in the region of the assembly with the highest temperatures.

The computational mesh representing the homogenized fuel compartment contents within a larger comprehensive model of a storage system is much coarser than that of the extremely detailed single-assembly or partial-assembly model typically used to derive the k_{eff} values (see Figure 3-5). Rather than a finely detailed mesh that captures the structure of the fuel, cladding, and fill gas surrounding the rods, the fuel region in a system model is simply a square NxN mesh, where N is on the order of the size of the rod array (e.g., 16x16 for a 14x14 array, 20x20 for a 17x17 array.) This results in a cross-sectional mesh on the order of 10^2 elements for the homogeneous region representing a single fuel assembly, compared to a cross-sectional mesh on the order of 10^4 to 10^5 elements in a detailed model that encompasses only one-quarter of an assembly. In typical applications, an array of k_{eff} vs. temperature values is incorporated into the input stream for the computational model of the cask as a table of material properties applicable to the elements of the homogeneous region representing the fuel assembly within its enclosing compartment.

The local mesh temperature in the homogeneous region representing the fuel assembly does not distinguish between the fill gas temperature, local fuel pellet temperature, and the fuel cladding temperature. By convention, the local mesh temperature is treated as the fuel cladding surface temperature. This is a reasonable assumption, because the radial temperature gradient from pellet center to cladding surface for the individual fuel rods is very small in a typical spent fuel assembly, due to the very low individual rod decay heat values. For example, in a WE 17x17 fuel assembly at 1 kW, the average decay heat of an individual rod in the array is approximately 3.8 Watts. This heat generation rate results in a steady-state heat flux on the order of 36 W/m^2 at the fuel rod surface. The temperature difference through the fuel pellet and across the cladding thickness as a result of this heat flux is a very small fraction of a degree (in K, C, or F). The radial cross-section of a given spent fuel rod at a given axial location along its length can be realistically treated as being at an essentially uniform temperature.

The homogeneous k-effective model has been validated against experimental data (as documented in the primary references, Sanders et al. 1993; Bahney and Lotz, 1996) for assembly decay heat loads up to 0.6 kW, with helium, nitrogen, and argon backfill, in test assemblies with conduction and radiation heat transfer, without significant convection. Some limited validation was also performed for vacuum conditions. The k-effective model yields slightly conservative (high by ~6-8%) estimates of peak cladding temperature in comparison to the validation data. Specific applications of the k-effective model have also been verified by comparison to detailed

evaluations with COBRA-SFS models of single assemblies and multi-assembly canisters, with individual assembly decay heat loads up to 2.5 kW. These applications have included a relatively wide range of PWR fuel types, including WE 14x14, WE 15x15, WE 17x17, CE 14x14, CE 16x16, and B&W 15x15 assemblies. More limited verification has been performed with BWR fuel types, including GE 7x7, GE 8x8, and some ATRIUM configurations.

The homogeneous k-effective model was used by necessity to represent the fuel assemblies in the 24P DSC in the detailed STAR-CCM+ model of the complete HSM15 system. Based on verification and validation of the k-effective model, as noted above, there is confidence that the fuel region temperatures predicted in this study are reasonable estimates for the postulated extended storage conditions. A more detailed evaluation of temperatures and temperature distributions on the fuel rods will require developing a detailed COBRA-SFS model of the canister. A COBRA-SFS model would include pin-by-pin modeling of the assembly, and detailed hydrodynamic modeling of gas flow within the assembly, capturing all modes of heat transfer from the fuel to the fuel storage compartment walls and beyond. A model at this level of detail could also include effects of contact conductance, for fuel assembly structures in contact with the wall.

For the thermal sensitivity study, the specific radial effective fuel conductivity values in the homogeneous fuel regions in the STAR-CCM+ model were determined from a detailed rod-and-subchannel model of a CE 14x14 assembly developed for the COBRA-SFS code. This model was applied with the various conditions assumed for the fuel assemblies in the matrix of variations for the sensitivity studies (i.e., backfill gas, component emissivities, and fuel assembly eccentricity within the storage compartment). The temperature versus k_{eff} values produced using the COBRA-SFS modeling results were used to create a user-defined function in the STAR-CCM+ model for radial thermal conductivity of the homogeneous fuel regions. The field function calculated the thermal conductivity of each cell within the fuel regions based upon the temperature of that cell.

The axial thermal conductivity of the homogeneous fuel regions was treated as conduction only, through an array of parallel paths, using the feature of STAR-CCM+ allowing anisotropic material properties. The specific values for input to the model were computed based on the mass-weighted average of the constituent materials of the region, which included the backfill gas, UO_2 fuel, and zircaloy cladding. At the bottom of the fuel region, the effective axial conductivity representing the space between the fuel pins and DSC bottom plug was calculated from the mass-weighted average of the assembly lower tie plate and the volume of helium gas in this region. The axial fuel thermal conductivity was specified in STAR-CCM+ with a user-defined function. The field function calculated the axial conductivity of each cell within each of the fuel regions, based upon local mesh temperature and axial location.

4. MATRICES FOR SENSITIVITY EVALUATIONS

Three sets of calculational matrices were developed to investigate the sensitivity of component temperatures of the HSM15 storage system to factors that could potentially affect or degrade the design-basis thermal behavior of the system. The three specific areas of interest identified for this study are defined as follows.

- degradation of the canister backfill gas from pure helium to a mixture of air and helium, resulting from postulated leakage due to SCC of canister welds
- uncertainties or changes in surface emissivity of system components, resulting from corrosion or other aging mechanisms, which could affect local heat transfer rates and cause potentially significant changes in temperatures and temperature distributions within the system
- effect of assumed fuel assembly position within the fuel storage compartments in the canister on fuel cladding and other internal component temperatures.

The matrix of calculations performed for the backfill gas composition study is described in Section 4.1. Section 4.2 describes the matrix for the surface emissivities study. Section 4.3 describes the matrix for the fuel assembly eccentricity study.

4.1 Matrix for Backfill Gas Study

The initial backfill gas for nearly all spent fuel storage systems is helium, an inert gas with a relatively high thermal conductivity, compared to other gases that might otherwise be suitable for this application. Initial pressurization of the dry storage canister after vacuum drying for many systems is only about 1 atm at ambient temperature, with the expectation that the gas temperature increase due to decay heat from the fuel will result in a maximum steady-state operating pressure of 1.5 to 3 atm at beginning of dry storage for design-basis maximum decay heat loading. Some designs, notably canisters in Holtec's HI-STORM 100 and HI-STAR systems, are designed to support an operating pressure of 7 to 9 atm at maximum decay heat loading at beginning of dry storage.

This means that dry storage canisters are expected to spend a significant portion of their service life at pressures above atmospheric ambient, so maintaining leak-free canister welds is an important design criterion. It has been postulated that SCC of canister steel affected by welding processes could allow helium gas to escape from the canister, depressurizing the interior to equilibrium with ambient. Canister internal pressure response to seasonal temperature changes could result in ambient air being drawn into the canister if the ambient temperature is low enough for the canister internal pressure to drop below ambient pressure. As canister internal pressure subsequently increases with rising ambient temperature, it would vent a mixture of air and helium. The cycle would then repeat as ambient temperatures dropped again. Such postulated seasonal "breathing" of the canister would gradually displace the entire helium gas inventory with air. The time scale of this process would depend on a number of factors, including the size and location of the cracks, the magnitude of the seasonal temperature variations, and the (gradually decreasing) decay heat load in the fuel.

Evaluating the potential for SCC and quantifying leak rates for the resulting loss of helium from the canister is beyond the scope of this study. This study does not include direct evaluation of effects on canister internal components due to chemical reactions resulting from ingress of reactive gases (e.g., oxygen, water vapor). The purpose of this study is to investigate thermal effects of backfill gas composition, by evaluating changes in temperatures in a specific horizontal storage system with postulated changes in backfill gas. The specific effects evaluated include changes in gas thermal conductivity and gas density, which affect the rate of heat transfer due to internal natural recirculation of the fill gas within the canister. These effects are studied over a range of decay heat values representing approximately 300 years in storage.

Table 4-1 summarizes the sensitivity matrix developed to examine this issue using the STAR-CCM+ model of the 24P DSC in HSM15. The first and last cases consist of the bounding conditions of 100% helium and 100% air, respectively, with three intermediate cases of increasing air (decreasing helium). The mass fraction of helium is decreased by half in each of cases 2 through 4. Table 4-1 also shows the equivalent molar fractions of the gas mixture, based on the selected mass fractions. Calculations were performed for each case at four different decay heat loads, representing the aging of the system over time, using the decay heat values listed in Table 3-1.

Table 4-1. Backfill Gas Composition Matrix for Backfill Gas Study

		Gas Composition	
Case No.	Component	(Mass Fraction)	(Mole Fraction)
1	Helium	1.0	1.0
	Air	0.0	0.0
2	Helium	0.5	0.88
	Air	0.5	0.12
3	Helium	0.25	0.71
	Air	0.75	0.29
4	Helium	0.12	0.5
	Air	0.88	0.5
5	Helium	0.0	0.0
	Air	1.0	1.0

The four simulations over the range of decay heat values from 7.58 kW to 2 kW in Case 1 represent the optimistic assumption that the canister would not experience leakage of backfill gas due to SCC, or any other potential failure of its ability to maintain internal pressure, for nearly 300 years. The four simulations in Case 5 represent the bounding assumption that the canister entirely fails to retain the initial helium backfill gas for even a relatively short time in storage. The helium is assumed to be entirely replaced with air very early in the timespan considered. Cases 2, 3, and 4 assume increasingly large losses of initial helium, and the range of decay heat values for these cases represent the full range of age-in-storage when the assumed leakage fraction might be postulated to occur.

Thermal properties for the backfill gas mixtures, including 100% air and 100% helium, are listed in Appendix A. The properties of pure helium and air were verified by comparison to properties obtained from the National Institute of Standards and Testing database 23 (NIST 2010). Properties for mixtures of air and helium were calculated using gas mixture algorithms from MATPRO (NRC, 1990). The applicability of these algorithms to the assumed DSC storage conditions was verified by comparison to basic physics of mixture gas dynamics (Van Wylen and Sonntag, 1973). All simulations were run as steady-state calculations, at an assumed ambient temperature of 27.8°C (82°F), corresponding to the temperature at the Calvert Cliffs ISFSI during the inspections in June 2012. Because this study does not address leak rates for the backfill gas, these calculations assumed a constant internal canister pressure for all backfill gas compositions evaluated.

4.2 Matrix for Emissivity Study

Surface emissivities of component materials were assumed to be at nominal values in the inspection evaluations and subsequent modeling studies. For the purposes of the thermal analyses related to the inspections at Calvert Cliffs, these values were considered reasonable and realistic within the uncertainty in known conditions in the storage module. The zircaloy cladding of the fuel rods in the CE 14x14 assemblies was assumed to have an emissivity typical of fuel at end of life in the reactor. This has been determined to be in the range of 0.6 to 0.9, with 0.8 as a typical value (Creer et al., 1987; Davis 1980; McKinnon et al., 1987).

It is well established that fuel rods come out of the reactor with a layer of oxide that extends the full length of the rod, with axially and azimuthally varying thickness depending upon the local temperature history during irradiation (Kesterson et al., 2013). Fuel rod surfaces are also subject to accumulation of CRUD, due to deposition of primary system corrosion products (Sandoval et al., 1991). The distribution of thicknesses of the oxide layer and the CRUD layer is of compelling interest for determining cladding material properties, particularly those related to strength, ductility, and corrosion mechanisms for the cladding, but from the standpoint of thermal analysis, the most important feature of this layer is its effect on surface emissivity for thermal radiation heat transfer. In determining the surface emissivity, variations in the thickness of the oxide and CRUD layer is largely irrelevant, since the effect on outer surface condition (in the wavelength range of thermal radiation) is essentially the same, regardless of thickness of the layer. The effect on thermal emissivity is to uniformly ‘blacken’ the surface of the rod. Extended time in wet storage would be unlikely to decrease this value, and may tend to increase it, depending on the management practices for criticality control in the spent fuel pool.

The canister internal components were clean and free of excessive corrosion at the time the cask was loaded and backfilled with an inert gas, as required by canister loading procedures followed at the Calvert Cliffs fuel handling facility. The outer surface of the DSC stainless steel shell was assumed to be clean at the time of insertion into the storage module, since wash-down of the outer surface of the canister is a normal step in the loading process, to reduce the potential for radioactive contamination. The internal surfaces of storage module components that are exposed to air flowing through the module (e.g., heat shield, support structures, and inner surfaces of the concrete walls) were also assumed to be at “as-built” values. These nominal emissivities for system components are listed in Table 4.2 for the base model of the 24P DSC within HSM15.

Table 4-2. Nominal Emissivity Values for Modeling HSM15

Surface	Material	Emissivity
Module Components--		
Base plate	carbon steel	0.65
Concrete	concrete	0.8
Door	concrete	0.8
DSC shell outer surface	stainless steel	0.46
Heat shield	stainless steel	0.46
HSM access sleeve	carbon steel	0.65
Rail plate	carbon steel	0.65
Steel support brackets	carbon steel	0.65
DSC components--		
DSC bottom cap	stainless steel	0.46
DSC shell inner surface	stainless steel	0.46
Guide sleeve outer surface	stainless steel	0.46
Spacer plate	carbon steel	0.65
Support rod	stainless steel	0.46
DSC top cap	stainless steel	0.46
Fuel rod cladding	zircaloy	0.8
Guide sleeve inner surface	stainless steel	0.46

In defining the sensitivity study matrix, all changes in surface emissivities were selected to reflect realistic changes that the system might be expected to undergo as a result of aging. This study does not attempt to capture the full range of all possible surface conditions of all systems. It is a study of how a particular system, HSM15 at the Calvert Cliffs ISFSI, with a reasonably well-characterized 'baseline condition' might be expected to change with time. Because aging processes tend to involve corrosion and accretion of material to initially clean surfaces, all realistic changes tend to be "for the worse"—that is, the emissivity value of a given surface will tend to increase above its initial more-or-less pristine value.

The initial value of 0.8 assumed for the emissivity of the fuel rod cladding is a realistic estimate for zircaloy-4 cladding. This study considers only zircaloy4 cladding, since this is the cladding material used in CE14x14 fuel assemblies. This study does not include evaluations of different fuel types with different cladding materials, such as ZIRLO™ or M5, and therefore cannot address potential variation in realistic emissivity values for these materials, compared to zircaloy-4. However, in considering possible variations in emissivity values for fuel rod cladding of whatever material, it is not reasonable to suppose that the emissivity values would decrease with age, because of the environment encountered by the fuel rods in the reactor and in the spent fuel pool. Low emissivity values for metal surfaces are generally achieved only if the surface is very clean and usually requires considerable polishing, as well. No matter how bright

and shining the fuel rods might be when they leave the manufacturing facility, they will accumulate oxide and CRUD layers while in reactor, and these layers will not be removed by long immersion in the spent fuel pool. The oxide layer may, in fact tend to continue to accrete, but at a rate much slower than at the high temperature conditions in-reactor. Therefore the emissivity of the fuel rod cladding surface can be expected to only increase with age.

The metal components that are exposed to the flow of air within this particular storage module (and in most other storage module designs) are stainless steel or carbon steel. The stainless steel is expected to resist corrosion *in situ* over the design life of the module (typically 40 years), and the carbon steel components are generally painted or otherwise covered with a protective coating to reduce corrosion. Changes in surface conditions due to corrosion may proceed quite slowly in these systems, and may not have significant effects on surface emissivity until long after the decay heat load has dropped to a very low value. However, dust particles and water vapor (which may contain dissolved salts) in the air flowing through the system can be expected to deposit material on exposed surfaces, which over time will tend to decrease the reflectivity of the surfaces, resulting in a corresponding increase in emissivity. Depending on conditions at a particular site, this process may proceed at a faster rate than surface condition changes due to corrosion, and could potentially increase corrosion rates.

For concrete surfaces, low emissivity values are extremely difficult to achieve, even with special efforts. As noted above, age-related changes in surface emissivities for the storage system are expected to be due to deterioration resulting from mechanisms such as surface oxidation or deposition of particulate material on surfaces. No credible aging mechanism would tend to decrease emissivities of the exposed concrete surfaces.

The emissivity study matrix is summarized in Table 4-3. The baseline for this matrix is Case A, using the nominal emissivities listed in Table 4-2. Case B is the bounding case of all components at maximum possible "blackness," with emissivity of 1.0 at all wavelengths. Case C evaluates the more reasonable assumption that the emissivities of the DSC internal components will remain at their initial values, due to the inert gas environment, but there would be significant aging of storage module components, which are exposed to the flow of ambient air through the system. Case D evaluates the assumption that the DSC internal components experience significant degradation in surface emissivity very early in storage, possibly due to water or water vapor incompletely removed during the drying process, but the storage module components remain relatively pristine.

Cases C and D include evaluations at two sets of emissivity values for the deteriorating surfaces, assuming a 50% increase in the affected surface emissivities, and also the bounding case of completely black surfaces. This approach permits evaluation of possible nonlinear effects of changing emissivities on the temperatures and temperature gradients in the system. Calculations were performed for the range of decay heat values from initial loading conditions for this module to storage out to approximately 300 years (i.e., total decay heat load of 10.58 kW, 7.58 kW, 6 kW, 4 kW, and 2 kW). In all cases, the backfill gas was assumed to be 100% helium, and all simulations were run as steady-state calculations, at an assumed ambient temperature of 27.8°C (82°F).

Table 4-3. Sensitivity Matrix for Emissivity Study

	Case A: base case (nominal emissivities)	Case B: (bounding case)	Case C: (DSC internals remain at nominal; module components deteriorate)		Case D: DSC internals deteriorate; module components remain at nominal	
Surface material	Emissivity					
Module and DSC exterior surface--						
Carbon steel	0.65	1.00	0.825	1.00	0.65	0.65
Concrete	0.80	1.00	0.90	1.00	0.80	0.80
Stainless steel	0.46	1.00	0.73	1.00	0.46	0.46
DSC internal surfaces--						
Stainless steel	0.46	1.00	0.46	0.46	0.73	1.00
Carbon steel	0.65	1.00	0.65	0.65	0.825	1.00
Zircaloy (fuel cladding)	0.80	1.00	0.80	0.80	0.9	1.00

4.3 Matrix for Fuel Assembly Eccentricity Study

The standard assumption in thermal evaluations for dry storage canisters is that the fuel assembly is centered within the storage compartment, as illustrated for the fuel assembly in the upper left corner in Figure 4-1. (Note that the fuel assembly block in the diagram in Figure 4-1 is not to scale; the gap width is greatly exaggerated for clarity.) This is in general a relatively small conservatism in the modeling approach, since the storage compartments in a typical basket are only slightly larger than the fuel assemblies. For a CE 14x14 fuel assembly within a fuel compartment in the 24P DSC, the wall gap is about 1.38 cm (0.545 in.). Therefore the possible range of variation in the peripheral gap is relatively small. The assumption that the fuel is centered in the storage compartment is in reality more of a convenient modeling simplification than a significant conservatism, even when used for horizontal systems, where such a configuration is clearly impossible.

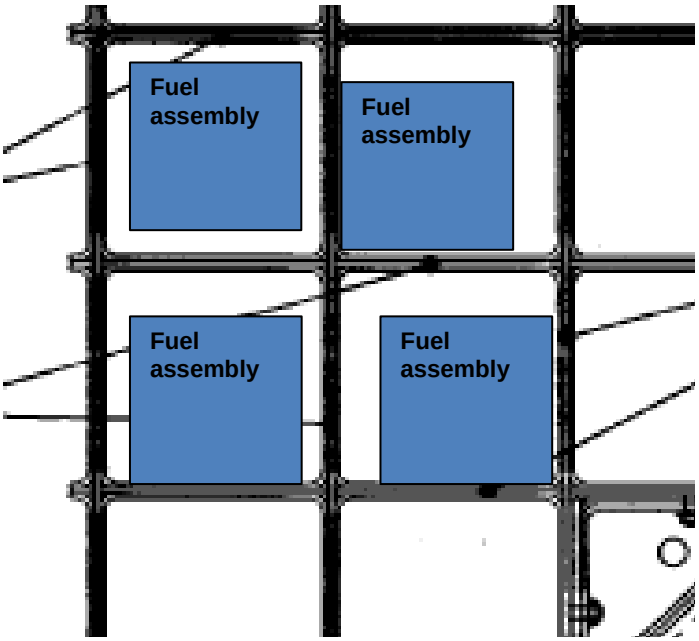

Figure 4-1. Possible Fuel Assembly/Basket Configurations in Horizontal Storage Systems (NOTE: The diagram is not to scale; the gap width is greatly exaggerated for clarity.)

The purpose of this study is to quantify the effect of this assumption on fuel cladding temperatures for a particular system, and provide an illustrative example of its relative significance for extended storage temperatures. Because the Star-CCM+ model is constrained to use the homogeneous k-effective model for the fuel assemblies, as discussed in Section 3.2, only a limited range of eccentricity effects can be evaluated with this model. This study evaluates the effect of two more realistic positions of the fuel assembly within the basket in a horizontal canister, in terms of the effect on conduction and radiation heat transfer between the fuel rods and the wall, due to the small range of possible changes in the length of the heat transfer paths from the rod surfaces to the wall.

The evaluation of changes in conduction is limited to the effect of a non-uniform wall gap on different ‘edges’ of the assembly. With the homogeneous k-effective model, it is not possible to investigate the effect of physical contact between the wall and the assembly hardware, or distorted fuel rods contacting the wall. Evaluation of sensitivity of fuel cladding surface temperatures to geometry changes at this level of detail would require a COBRA-SFS model of the system, which can include local contact conductance and specific geometry variations within the fuel assembly. This is recommended for future work, as part of recommendations for extending this evaluation of a single specific system to a broader study of thermal modeling sensitivities within storage canisters.

Within the constraints of the limitations of the homogeneous k-effective model, this study evaluates the effect of two additional configurations of the fuel assembly within the storage compartment. The first is with the fuel assembly resting on the lower plate of the enclosing basket cell, but centered in the compartment side-to-side. The second is with the fuel assembly shifted against one corner of the cell, as illustrated in Figure 4-1. Calculations were performed

only for the maximum decay heat value at beginning of storage for the 24P DSC in HSM15 (i.e., 10.58 kW), since the effect is expected to be small, and will dwindle with decreasing decay heat load. In all cases, the backfill gas was assumed to be 100% helium, and all simulations were run as steady-state calculations, at an assumed ambient temperature of 27.8°C (82°F).

4.4 Fuel Effective Conductivity Models for Sensitivity Studies

The fuel assemblies are represented in the STAR-CCM+ model using the fuel effective conductivity model, as described in Section 3.2. This model treats the region inside the fuel storage compartment as a homogeneous solid with heat generation, and represents conduction and thermal radiation heat transfer in the radial direction with an effective conductivity function. The radial k_{eff} values used in the base model for this study were derived assuming helium backfill, with nominal surface emissivities of 0.8 for the zircaloy cladding and 0.46 for the fuel compartment walls. Various cases in the sensitivity matrix assume different backfill gas compositions, different surface emissivities for the cladding and fuel compartment walls, and different geometry configurations for the fuel assembly within the basket. It was therefore necessary to generate appropriate sets of k_{eff} values for each of these configurations.

The fuel effective conductivity in the radial direction is a function of the assembly heat generation rate, backfill gas, storage compartment geometry, fuel assembly characteristics, and the peak-to-wall temperature gradient. As discussed in detail in Section 3.2, the k_{eff} values for a given fuel assembly in a particular storage system are typically obtained by creating a detailed model of a single fuel assembly (with a CFD or FEA code), and generating a database of peak temperatures for the assembly heat generation rate, basket geometry, and range of boundary wall temperatures of interest. These temperatures are then used to develop a set of k_{eff} values as a function of temperature, which can be used to calculate radial heat transfer in the homogeneous fuel region(s) of a more general system model, such as the STAR-CCM+ model of the 24P DSC in HSM15.

For this study, the databases for the different sets of k_{eff} values for the radial direction were obtained with a detailed rod-and-subchannel model of a CE 14x14 fuel assembly using the COBRA-SFS code. Experience with this code in independent verification of k_{eff} values for a wide range of fuel types, vendor-specific designs, and basket geometries has shown that the COBRA-SFS thermal-hydraulic modeling approach can produce k_{eff} values that are identical to results obtained with detailed assembly models using CFD and FEA codes.

The sensitivity evaluations for this study require eight separate radial k_{eff} models, in addition to the base model, to capture the range in variation of parameters affecting the fuel radial effective conductivity. Four of these are for the different backfill gas compositions assumed in the backfill gas sensitivity study. Two are for the range of variation in the fuel cladding and compartment wall emissivities, and two are for the range of variation assumed for the position of the fuel assembly within the storage compartment.

The radial k_{eff} values for the backfill gas study are shown in Figure 4-2. The curves in this plot clearly illustrate the decreasing conductivity of the fill gas, from 100% helium to 100% air. Over the range of fuel temperatures of interest in this study, the effect of fill gas composition on k_{eff}

values is relatively constant as a function of temperature. This is the expected result, as the difference in thermal conductivity for air and helium is relatively constant over this range.

The effective conductivity of the assembly in the axial direction is treated as an array of parallel paths through the fuel, zircaloy cladding, and backfill gas. The conductivity of the fuel and cladding is the same in all cases, but the conductivity of the fill gas varies with assumed gas composition. Figure 4-3 shows the effective conductivity for axial heat transfer along the length of the fuel assembly, for the range of backfill gas compositions evaluated. For the emissivity sensitivity study and the eccentricity sensitivity study, the axial effective conductivity does not change, since the backfill gas is assumed to be 100% helium in all cases for these studies, and the overall fuel assembly geometry is unchanged. The base-case axial effective conductivity is used in all of these calculations.

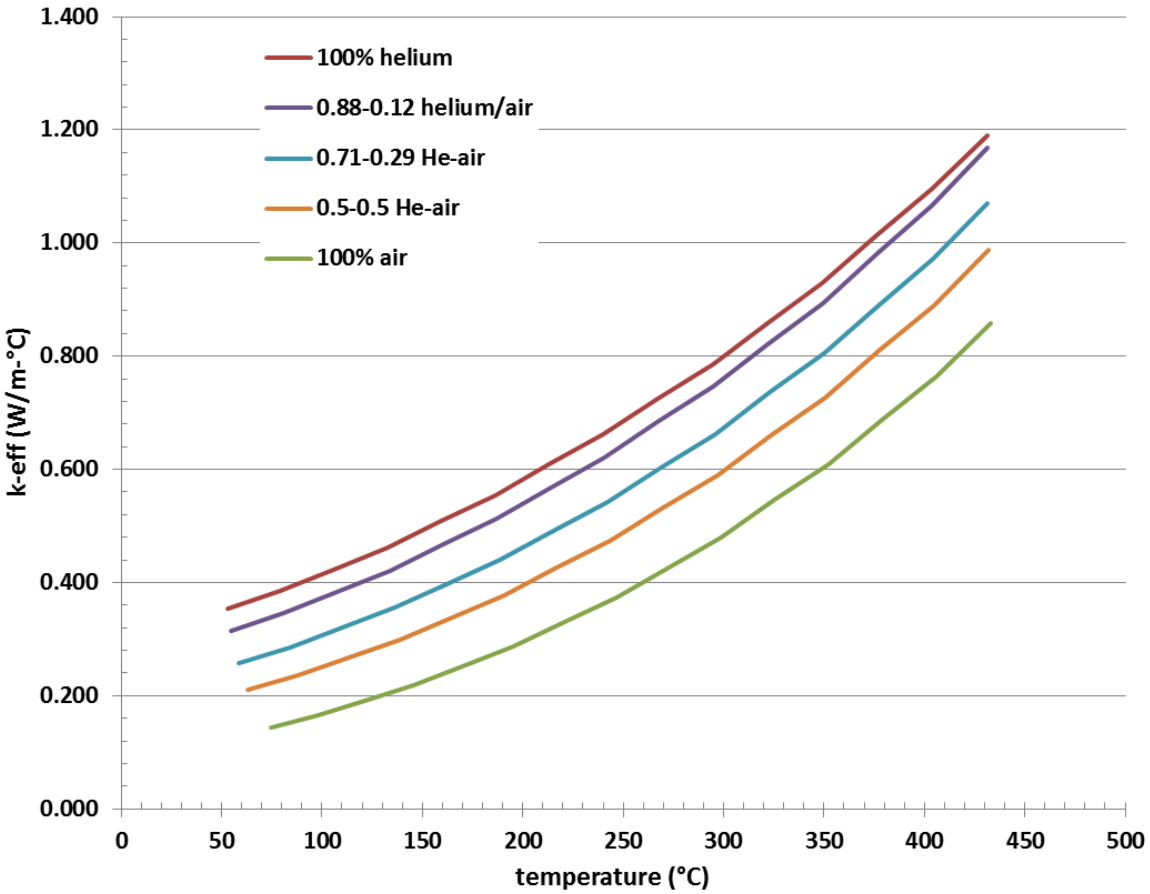

Figure 4-2. Fuel Effective Radial Conductivity for CE 14x14 fuel as a Function of Backfill Gas Composition (for Backfill Gas Sensitivity Study)

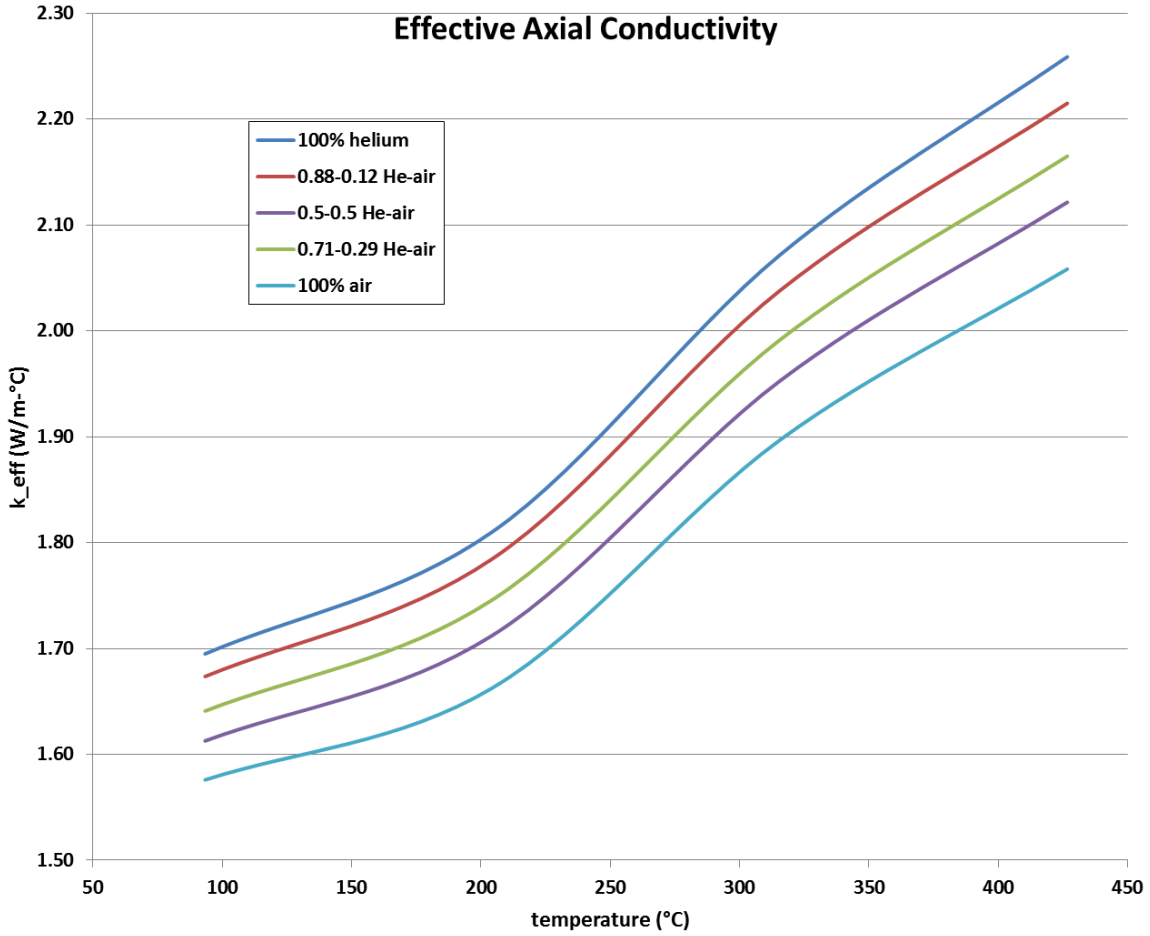

Figure 4-3. Fuel Effective Axial Conductivity for CE 14x14 Fuel as a Function of Backfill Gas Composition (for Backfill Gas Sensitivity Study)

The k_{eff} values developed for the emissivity study are shown in Figure 4-4. The matrix of cases considered for this study contains only two variations from the base case assumption. These are the bounding assumption of 1.0 emissivity for all surfaces (Case B and Case D-2), and the 50% degradation in emissivities assumed for Case D-1. The effect of assumed surface emissivity on the k_{eff} values is relatively large, and is significantly nonlinear. The effect is greater at higher temperatures and decreases with decreasing temperature, as the thermal radiation component of heat transfer within the assembly decreases.

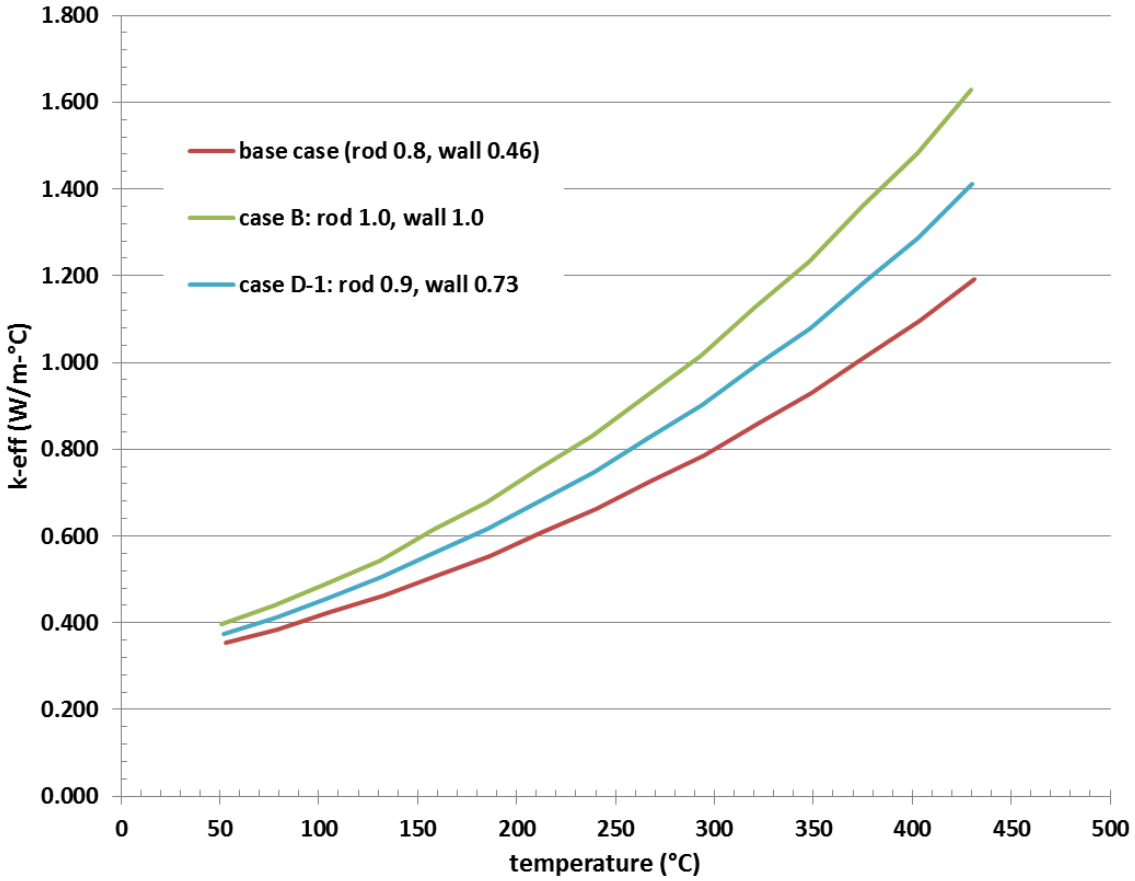

Figure 4-4. Fuel Effective Conductivity for CE 14x14 Fuel as a Function of Surface Emissivities (for Emissivity Sensitivity Study)

The k_{eff} values developed for the eccentricity study are shown in Figure 4-5. The base case assumption is that the fuel assembly is centered within the compartment. The first variation from the base case is with the assembly on the bottom face of the compartment, with uniform side gaps, and the second is with the assembly tucked into one corner. The k_{eff} values plotted in Figure 4-5 show that this is a very small effect when using the homogeneous representation of the fuel assemblies, and consequently, the effect on temperatures is expected to be quite small.

The temperature database calculations for the k_{eff} values for the eccentricity and emissivity studies assumed 100% helium fill gas. The range of applicability of these effective conductivity functions have been verified for assembly decay heat values from 0.5 to 0.05 kW per assembly. This spans the full range of individual assembly decay heat values corresponding to the assumed total decay heat loads in the DSC. Total decay heat loads from 10.58 kW down to 2 kW correspond to assembly decay heat values ranging from approximately 0.5 to 0.1 kW.

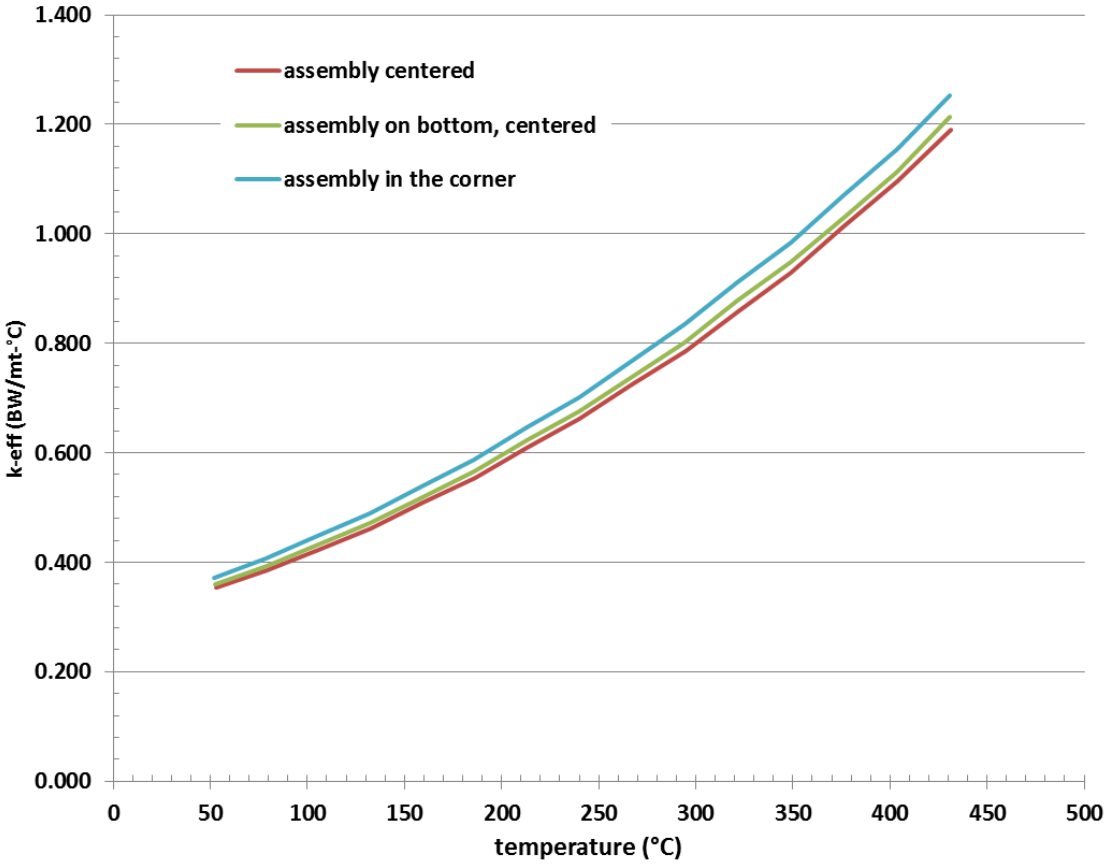

Figure 4-5. Fuel Effective Conductivity for CE 14x14 Fuel as a Function of Assembly Position within Fuel Compartment (for Assembly Eccentricity Sensitivity Study)

5. SENSITIVITY EVALUATIONS

This section presents the results of the sensitivity evaluations performed for the matrices defined in Section 4. The canister backfill gas study results are discussed in Section 5.1. The emissivity sensitivity study results are presented in Section 5.2. The evaluations of the effect of assumed fuel assembly eccentricity within the storage compartment are discussed in Section 5.3.

5.1 Results of Canister Backfill Gas Study

This section presents the results obtained in the canister backfill gas sensitivity study for the matrix of cases described in Section 4.1 and Table 4-1. Figures 5-1 and 5-2 illustrate the effect of canister backfill gas on system temperatures with a comparison of results for 100% helium backfill gas and 100% air backfill gas for a total decay heat load of 7.58 kW. The color contour plots show temperatures for radial and axial cross-sectional slices through the system, at the location of peak clad temperature. The axial slice is on a plane passing through the 'column' of fuel assemblies that includes the assembly containing the peak clad temperature. These results show that the peak component temperatures within the DSC are higher with air as the back fill gas, compared to the results with helium, as expected. With a total decay heat load of 7.58 kW, the peak clad temperature is approximately 25 degrees Celsius higher with air as the backfill gas, compared to the value obtained with helium. Similar results are obtained with mixtures of air and helium as the backfill gas, with the difference in peak temperature increasing as the assumed fraction of air increases. The same pattern is predicted for the lower decay heat loads evaluated in this study, but at lower overall peak temperatures.

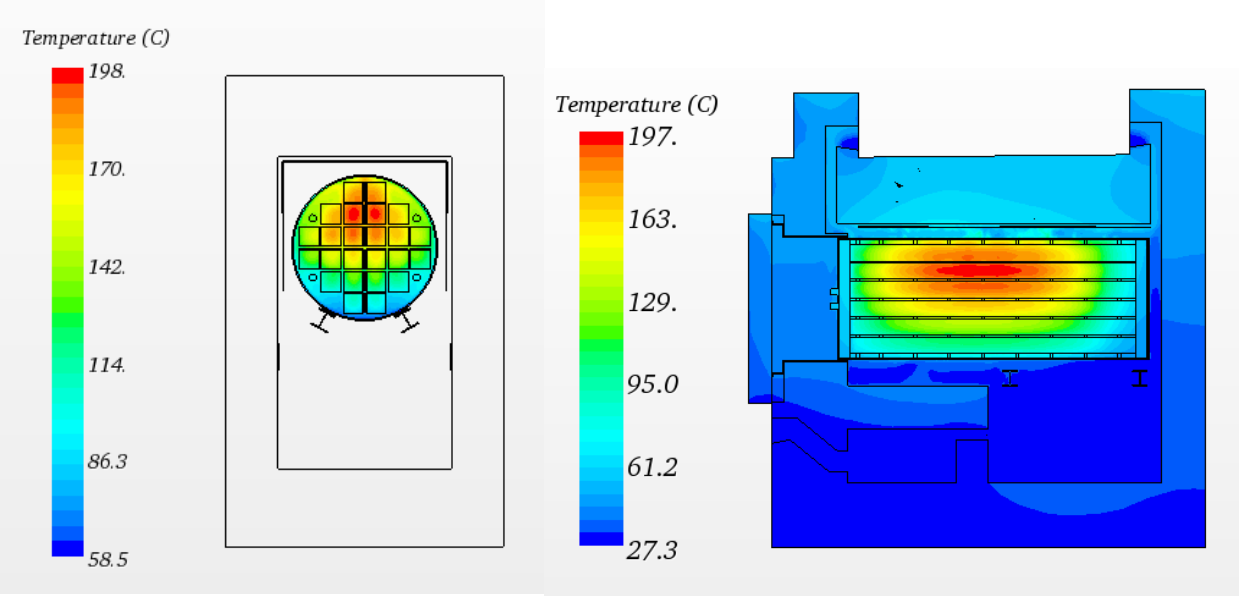

Figure 5-1. DSC Internal Temperatures at 7.58 kW Total Decay Heat Load: Results with 100% Helium as Backfill Gas

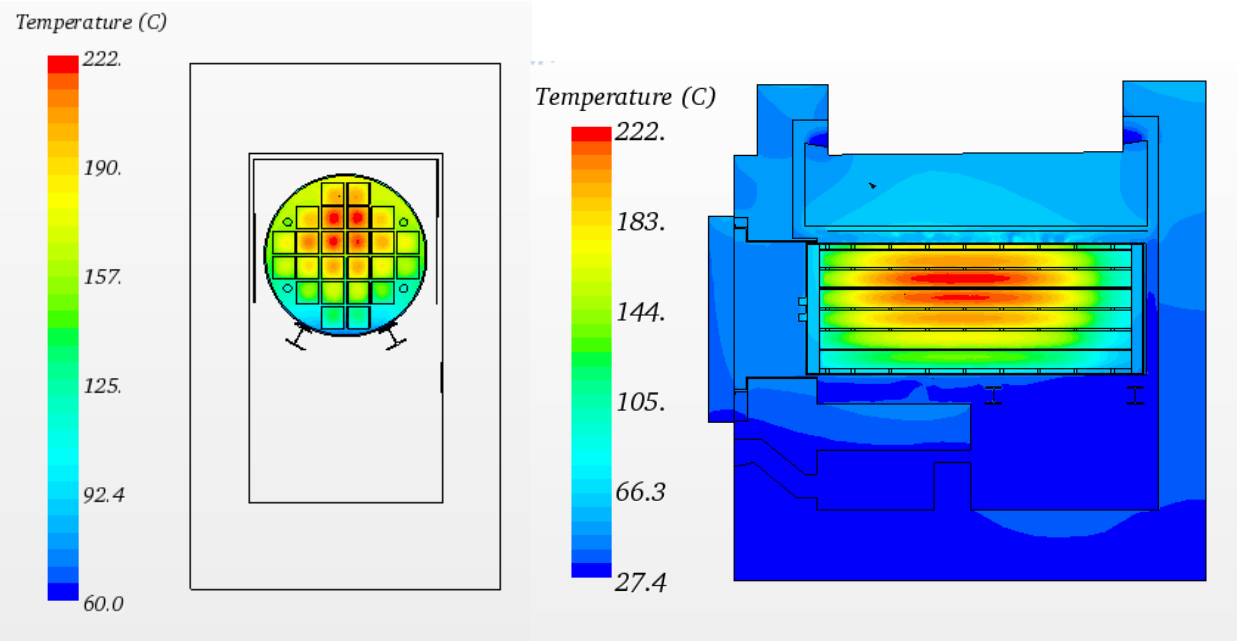

Figure 5-2. DSC Internal Temperatures at 7.28 kW Decay Heat Load: Results with 100% Air as Backfill Gas

The effect of backfill gas mixture on internal temperatures of DSC components is the expected result, and is too easily predicted to justify developing the matrix of cases for this study. The main motivation for this study is evaluation of the potential for using DSC outer shell temperature measurements to detect canister loss of helium due to SCC of the DSC welds. Therefore, the results presented here focus on the sensitivity of DSC shell temperatures and temperature distributions to backfill gas composition. Figure 5-3 shows color thermographs comparing the DSC shell surface temperatures obtained with 100% helium backfill to those obtained assuming 100% air within the canister, at a total decay heat load of 7.58 kW (average 0.316 kW/assembly). The plots in Figure 5-3 also show a similar comparison for a total decay heat load of 2 kW (average 0.083 kW/assembly), corresponding to the projected decay heat in this canister approaching 300 years in storage.

The plots in Figure 5-3 indicate that the differences in peak temperatures on the DSC shell are relatively small for the assumed variation in backfill gas at a given decay heat load. For these two cases, the difference is only 2 or 3 degrees (Celsius). This is the expected result, since the total heat load in the canister is the same in each of the two comparisons. The DSC shell outer surface temperature is determined primarily by heat transfer rates to the ambient air, due to natural circulation air flowing through the storage module and around the canister. (This is the reason that it is not generally possible to determine peak fuel cladding temperatures based on canister shell temperatures alone, but discussion of that generic dry storage evaluation issue is beyond the scope of this study.)

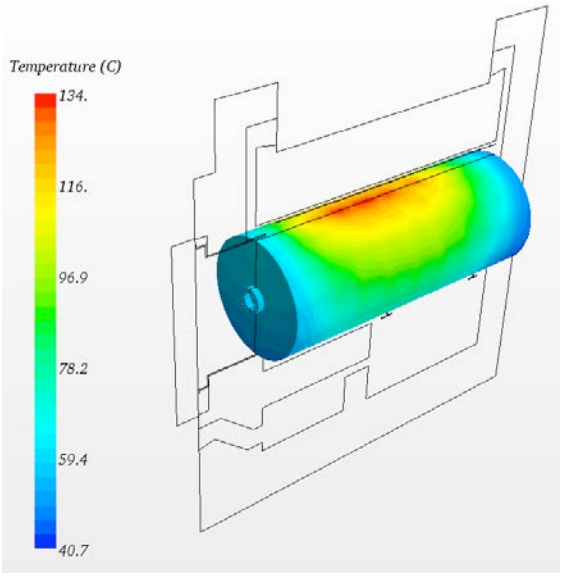

(100% Helium, 7.58 kW)

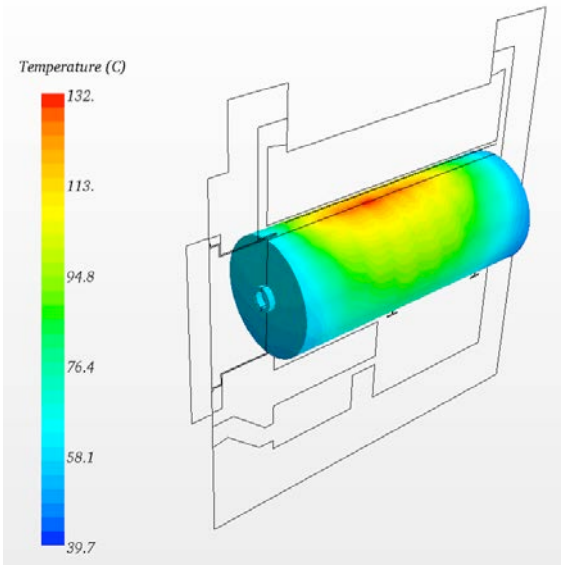

(100% air, 7.58 kW)

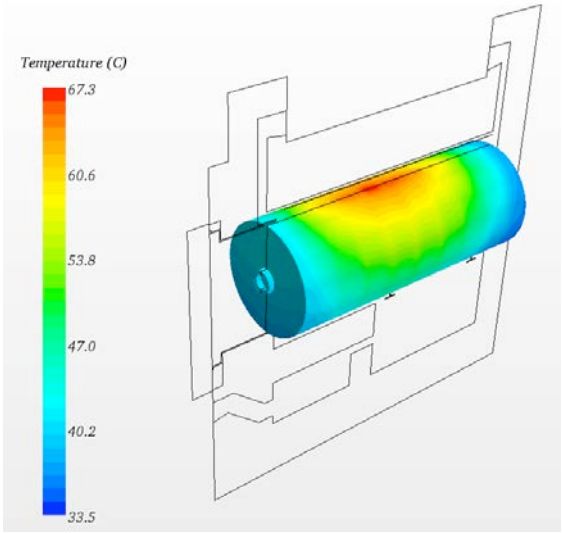

(100% Helium, 2 kW)

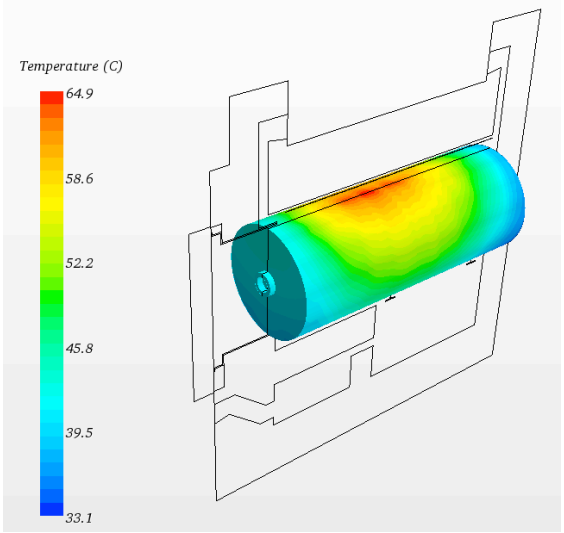

(100% air, 2 kW)

Figure 5-3. DSC Shell Temperatures at 7.58 kW and 2 kW Decay Heat Loads, Comparing Results with Helium and Air Backfill Gas

This general behavior is further illustrated in Figure 5-4 with line plots of temperature profiles along the top of the DSC, at 7.58 kW and 2 kW decay heat loads, for the full range of backfill gas compositions evaluated. Similarly, Figure 5-5 shows the temperature profiles along the side of the DSC for these cases. The line plots show the same trends as the color graphic plots, but also reveal some small but potentially interesting differences in the local temperature distribution, as a function of backfill gas.

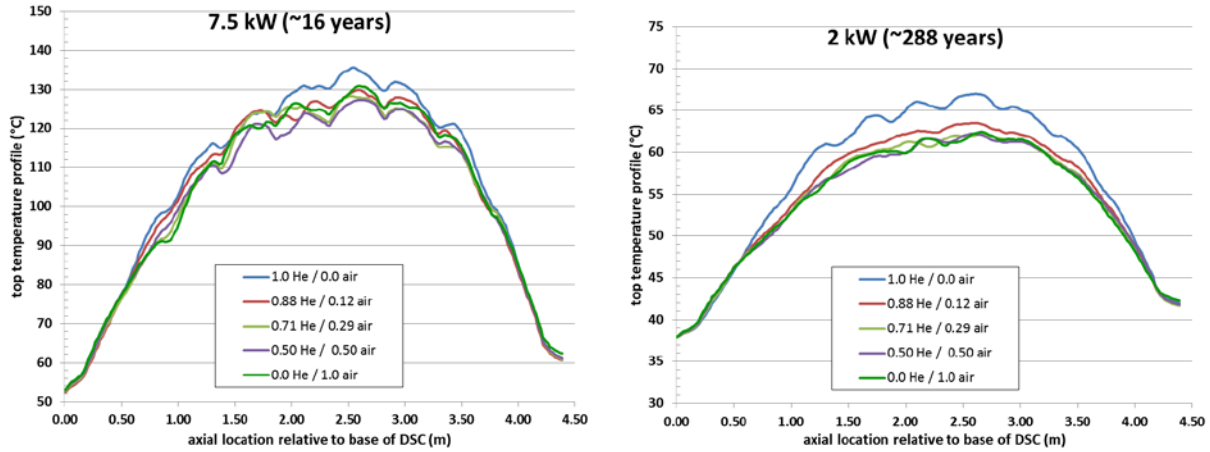

Figure 5-4. DSC Top Temperatures at 7.58 kW and 2 kW Decay Heat Loads, Comparing Results for all Backfill Gas Compositions Evaluated

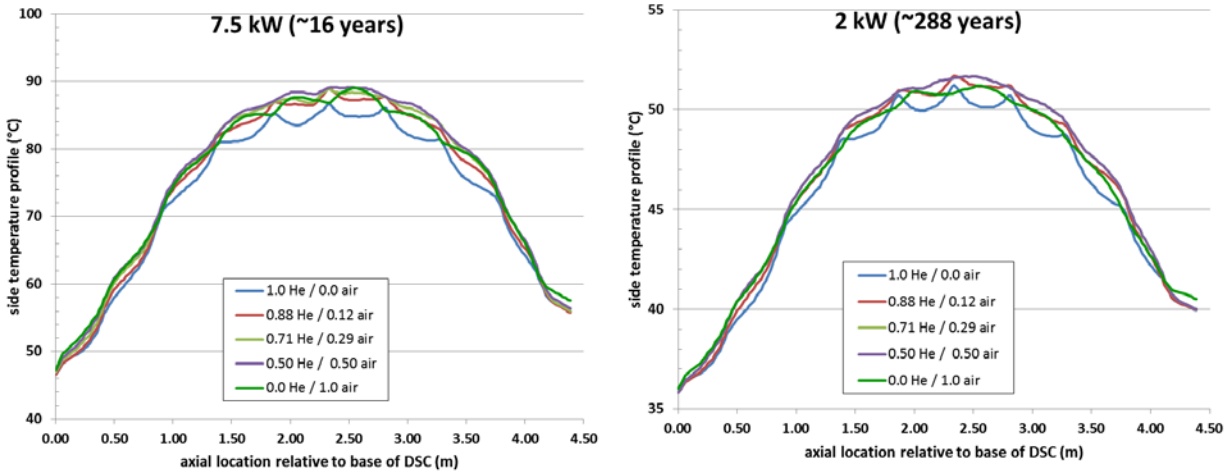

Figure 5-5. DSC Side Temperatures at 7.58 kW and 2 kW Decay Heat Loads, Comparing Results for all Backfill Gas Compositions Evaluated

The peak values of the temperature differences between the top and side of the canister are summarized in Table 5-1 for all cases evaluated in this study. These results show that there is a discernible difference in the top-to-side temperature difference as a function of gas mixture composition. This difference persists over the full range of decay heat values tested, even as the temperature gradients flatten on the DSC shell surface. The change in temperature differences is noticeable even with only a relatively small fraction of air (50% mass fraction, corresponding to 12% mole fraction) mixed in with the helium backfill gas. This behavior is currently under investigation as a potential signature of backfill gas composition that might be used to monitor storage systems for evidence of weld seal degradation due to stress corrosion cracking.

Table 5-1. Peak Temperature Differences Top to Side for Backfill Gas Sensitivity Study

Gas Composition			Temperature Difference (degrees Celsius)			
Component	(Mass Fraction)	(Mole Fraction)	7.5 kW (~16 years)	6 kW (~38 years)	4 kW (~88 years)	2 kW (~288 years)
Helium	1.0	1.0	50.9	40.4	28.8	16.9
Air	0.0	0.0				
Helium	0.5	0.88	42.6	36.8	26.8	12.3
Air	0.5	0.12				
Helium	0.25	0.71	40.0	33.2	23.0	10.9
Air	0.75	0.29				
Helium	0.12	0.50	38.4	32.7	23.4	10.8
Air	0.88	0.50				
Helium	0.0	0.0	42.1	34.2	25.0	11.6
Air	1.0	1.0				

The magnitude of the top-to-side temperature difference is greatest for 100% helium, at all decay heat levels evaluated. The reason for the slight increase in the differences with 100% air, compared to the trend of decreasing difference with increasing percentage of air in the mixture at any given decay heat load is not entirely clear, and may reflect limitations of the CFD modeling of natural convection in closed containers, as discussed in Section 5.1.1. (Further study of the computational modeling of natural recirculation within the DSC enclosure is recommended, based on the results obtained in this initial investigation.)

The comparison of peak temperature differences alone gives an incomplete picture of the complexity of the flow behavior within the DSC, since the location of the peak temperature is not necessarily the same for all cases. A more complete picture of this effect is given by line plots of the point-by-point temperature differences, as shown in Figure 5-6. This behavior is due to natural circulation of the backfill gas within the DSC, which is allowed by the relatively open geometry of the fuel support structure in this particular canister design. In the 24P DSC, the basket structure containing the fuel assemblies consists of 24 fuel tubes supported by an axial array of steel disks spanning the cross-section of the canister. (The disks account for the 'humps' in the line plots, with minima at the locations where the disks touch the canister wall.)

The region between the disks and external to the fuel tubes is relatively open (see Figure 3-4), allowing top-to-bottom recirculation of the backfill gas due to the circumferential temperature gradient on the DSC outer shell. This temperature gradient is the result of natural circulation of air through the module and around the DSC cavity, as illustrated in Figure 5-7. The overall top-to-side temperature difference seen in the 24P DSC is the result of the interaction of the two natural recirculation flow fields, via heat transfer through the canister shell. Canister designs that do not have significant natural circulation flow paths around the basket would not show the variation in the top-to-side temperature difference with fill gas composition observed in this study. The possibility of using this behavior to potentially provide information on backfill gas composition is limited to casks of similar design to the 24P.

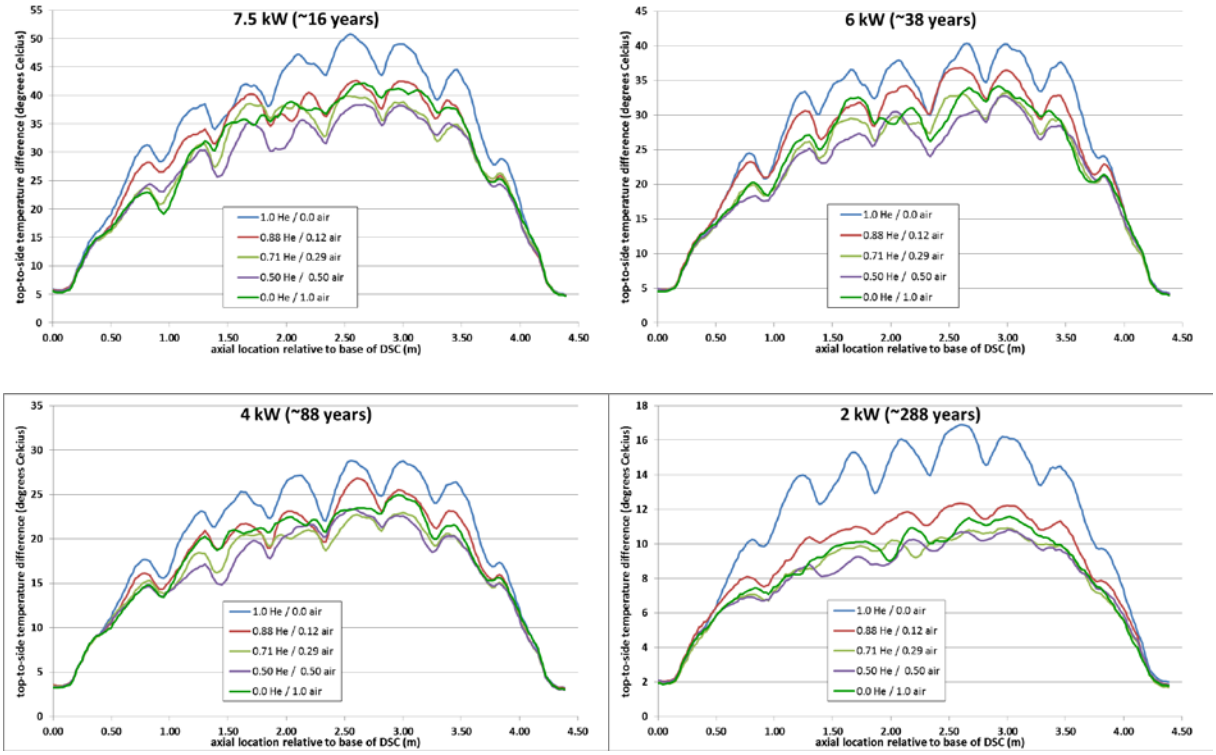

Figure 5-6. Axial Distribution of DSC Top-to-side Temperature Differences at all Decay Heat Loads for all Backfill Gas Compositions Evaluated in this Study

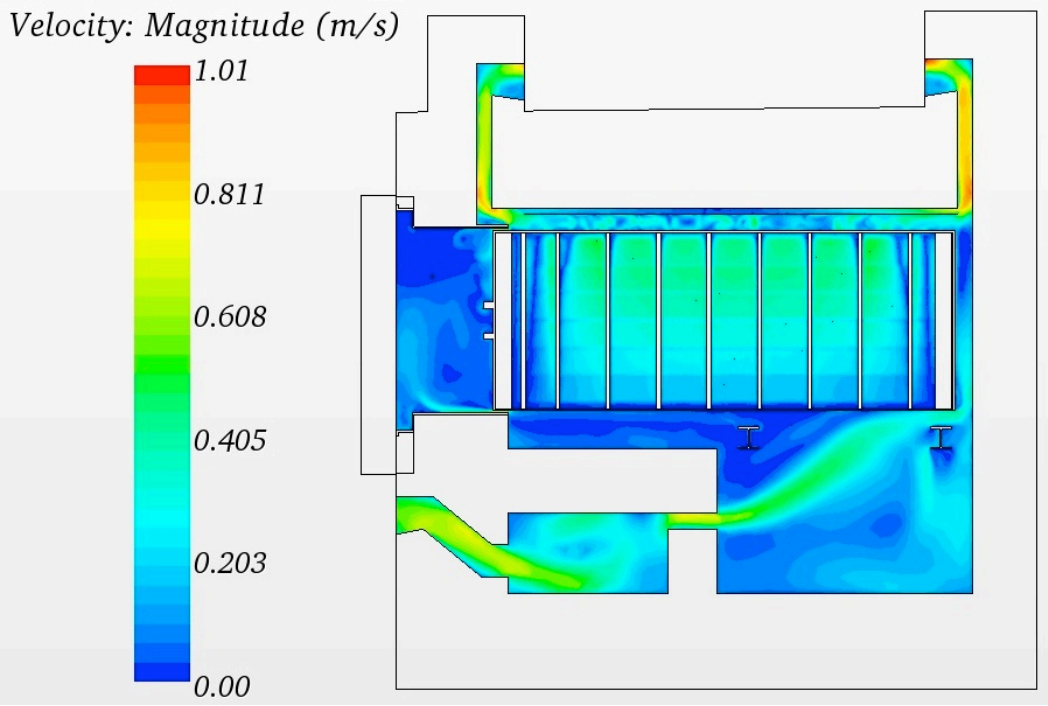

Figure 5-7. Velocity at Axial Midplane in HSM15

The importance of the CFD solution of the flow field for natural circulation within the canister in obtaining accurate predictions of the change in the canister shell temperature distributions with different backfill gas compositions prompted a closer look at the capabilities of the STAR-CCM+ code to model gas behavior within a sealed container. Non-isothermal gas in a sealed container cannot be modeled with the ideal gas law when using the standard steady-state incompressible flow solvers typically used in CFD codes. The recommended approach (from the CFD code vendors) is to use the Boussinesq approximation to solve for the gas flow field within a closed container. The applicability of this approximation to evaluation of internal recirculation flow in the 24P DSC is discussed in Section 5.1.1.

5.1.1 CFD Modeling of Natural Convection in Sealed Containers

Based on the recommendation of the CFD code vendors (see for example ANSYS Inc. 2012), non-isothermal gases in sealed containers should not be modeled as ideal gases when using their standard incompressible flow solvers. Absolute pressure is not computed correctly for an enclosed volume, and the computed density based on the erroneous pressure is incorrect. By extension, flow velocities computed from the density gradients would also be incorrect, but the error is detectable as a failure to conserve mass for the gas within the enclosure.

The cause of this error is the treatment of the pressure field solution in the incompressible CFD model. The solution for the pressure field is relative to an arbitrary constant, typically specified by the user as a reference pressure. The computed field is the gauge pressure relative to this reference. For fluid flow systems that are open to the environment, the reference pressure is the pressure at the inlet or outlet boundary (i.e., ambient pressure) and this remains constant during a steady-state simulation. For sealed containers undergoing temperature change, however, a constant value for the reference pressure is inadequate and the solution methodology has no provision for computing it directly. This leads to density errors, because in the incompressible model the ideal gas density is computed directly from the reference pressure and the local temperature.

For a sealed dry storage canister (such as the 24P DSC), the fill gas pressure varies with temperature changes resulting from the balance between the internal decay heat load and the rate of heat removal by natural convection from the canister exterior. But instead of computing pressure using the initial gas density and current temperature, the CFD code computes the density with the ideal gas law, using the reference pressure. In a simulation initialized at ambient conditions, the increase in fill gas temperature due to fuel decay heat results in a non-physical *decrease* in average fill gas density. This results in an overprediction of peak fuel temperatures, since natural convection cooling within the canister is reduced due to the artificially low fill gas density.

The recommended approach (ANSYS Inc. 2012) is to use the Boussinesq approximation for the fill gas, rather than treating it as an ideal gas. The Boussinesq approximation consists of modeling the gas density as a constant, and approximating the localized density gradients that drive natural convection flow as a body force computed from the thermal expansion coefficient, β, defined as a gas material property. For an ideal gas, the thermal expansion coefficient is equal to the inverse of the absolute temperature.

The Boussinesq approximation is accurate for small temperature differences ($\beta \Delta T << 1$), but temperature differences are not typically that small in a dry storage canister. For the 24P DSC, this term is on the order of 0.5 for the conditions evaluated in this study. For evaluations with large temperature changes, the *FLUENT Users Guide* (ANSYS Inc. 2012) recommends modeling the gas as ideal and solving the problem as a transient calculation, as an alternative to the Boussinesq approximation approach. Testing in simple 2-D geometries found that this approach suffers from the same limitations as seen in steady-state simulations. It may be possible to adjust appropriate solution parameters to make this approach work correctly, but a transient solution is impractical for the HSM15 model, due to the large size of the model and the computational effort required by the long thermal time constants of this system.

Based on comparisons with results for simplified models where the ideal gas law can be used to obtain an appropriate solution in steady-state and transient evaluations, there is some confidence that the Boussinesq approximation approach can produce a reasonably accurate solution for the range of conditions evaluated in this study, even though the large range of temperatures exceeds the recommended range for this approximate model. However, additional modeling studies are strongly recommended, to verify and validate the natural circulation behavior predicted with CFD models of flow dynamics within the dry storage canister. This is particularly important if evaluations are to be carried out for higher decay heat loads, such as values approaching system design-basis limits, where the temperature differences are likely to be much larger than encountered in this study of a DSC that was initially loaded at less than 60% of design basis.

5.2 Results of Surface Emissivities Sensitivity Study

Material surface conditions within the storage module can affect temperatures and temperature distributions mainly through the effect of surface emissivity on thermal radiation heat transfer. Effects on surface heat transfer by means of convection are in general expected to be negligible, over the range of conditions postulated for extended storage for the 24P in HSM15. In the STAR-CCM+ model of the 24P in HSM15, the wall surface is treated as smooth in the CFD solution for fluid velocities and temperatures near the wall. Section 5.2.1 presents a detailed background discussion of why this is a reasonable assumption for convection heat transfer in general, with particular focus on how this relates to the conditions postulated in HSM15. The results of the sensitivity study, showing the effect of surface conditions on thermal radiation heat transfer, are presented in Section 5.2.2.

5.2.1 Effect of Surface Conditions on Heat Transfer

Thermal radiation is a strong function of the surface emissivity, and as a result, significant changes in local surface temperatures and temperature gradients might reasonably be expected with changes in surface conditions that affect surface emissivity values over time in the storage system. A detailed discussion of thermal radiation modeling, as implemented in STAR-CCM+ is included in the Users Guide (see CD-adapco, 2012). For the purpose of showing the influence of emissivity on heat flux due to thermal radiation exchange, the simple case of radiation heat transfer between two surfaces that see only each other provides a convenient illustration of this phenomenon. Treating the thermal energy exchange as a radiation network, the net energy exchange Q due to thermal radiation between two surfaces is given by

$$Q = \sigma(T_1^4 - T_2^4) / \left[\frac{(1-\epsilon_1)}{\epsilon_1 A_1} + \frac{1}{A_1 F_{1-2}} + \frac{(1-\epsilon_2)}{\epsilon_2 A_2}\right]$$

where σ = Stefan-Boltzmann constant, 5.669 x 10^{-8} W/m^2-°K^4
T_1 , T_2 = temperatures of surfaces 1 and 2
ϵ_1 , ϵ_2 = emissivities of surfaces 1 and 2
A_1 , A_2 = areas of surfaces 1 and 2
F_{1-2} = geometric view factor between surfaces 1 and 2

The above relationship shows that increasing emissivity values tend to decrease the magnitude of the emissivity terms in the denominator, such that in the limit of emissivities equal to 1.0, the relationship reduces to

$$Q = \sigma F_{1-2} A_1 (T_1^4 - T_2^4)$$

This is the maximum amount of energy that can be exchanged between the two surfaces by thermal radiation in this simple geometry. In an actual system, surfaces generally see more than one other surface, so the radiation exchange network is more complicated than this simple equation shows. However, the general effect of emissivity on the heat transfer rate is essentially the same, even in a more complicated geometry.

Because these flow conditions are natural circulation at low velocities (<0.5 m/s on the DSC outer surface, and <0.25 m/sec within the DSC, on the shell inner surface and fuel compartment walls), convection heat transfer within the module is relatively insensitive to surface conditions. This applies particularly to natural circulation of the helium gas within the DSC, but is also the case for the flow of air through the module. The effect of emissivity is seen most directly in thermal radiation, due to the very different physical mechanism of heat removal, compared to convection. In general, the temperature at a surface subject to low-velocity convection heat transfer is essentially unaffected by the surface condition, and analyses are typically performed using the assumption of 'smooth' surfaces. This is because the flow velocity at the surface for any system is by definition zero, regardless of how smooth or rough the surface might be. For a constant heat flux condition at a surface where heat is being removed by convection, the surface temperature is determined by the balance between heat conducted from the surface to the fluid and the rate of its subsequent removal by convection (i.e., physical movement of the heated fluid away from the surface). That is,

$$q_{constant} = -k_f \frac{\partial T}{\partial y}|_{y=0} = h(T_s - T_\infty)$$

where k_f = thermal conductivity of the *fluid*
y = distance from the surface within the fluid boundary layer
T_s = surface temperature
T_∞ = bulk fluid temperature
h = surface heat transfer coefficient

In this relationship, the condition of the surface is largely irrelevant. However, the surface condition can have a significant effect on the material temperatures *within* the wall, where heat is

moving down the local gradients to the surface temperature determined by convection heat transfer. For example, considerable effort has been expended in determining the effect of oxidation on fuel rods in-reactor, even though the rod surface temperature is determined by the hydrodynamics of the coolant, not the condition of the rod surface. The focus in that case is on the effect on the cladding *internal* surface temperature and the consequent effect on fuel material temperatures, not the cladding outer surface temperature. The fuel rod outer surface temperature is the same (for the same hydraulic conditions), with or without the oxide. In a used fuel storage system, the heat flux and therefore the temperature gradients of interest are much smaller than encountered in reactor conditions, but the physical processes are essentially the same.

Conduction heat transfer through a wall with essentially constant heat flux can be expressed simply as

$$q_{constant} = -k_s \frac{\partial T}{\partial x}$$

where k_s = thermal conductivity of the *solid material of the wall*

$\frac{\partial T}{\partial x}$ = temperature gradient in the solid material of the wall

For simplicity, this discussion is presented in terms of one-dimensional heat conduction. Since the primary direction of heat removal from the fuel is radially through the structures of the storage canister, this is a reasonable approximation for heat flow from the fuel to the canister shell. Essentially any given surface in the canister that sees this radial heat flow, therefore, can be conceptualized as a wall with a constant heat flux on one side and a hydrodynamic temperature boundary on the other, as shown in Figure 5-8.

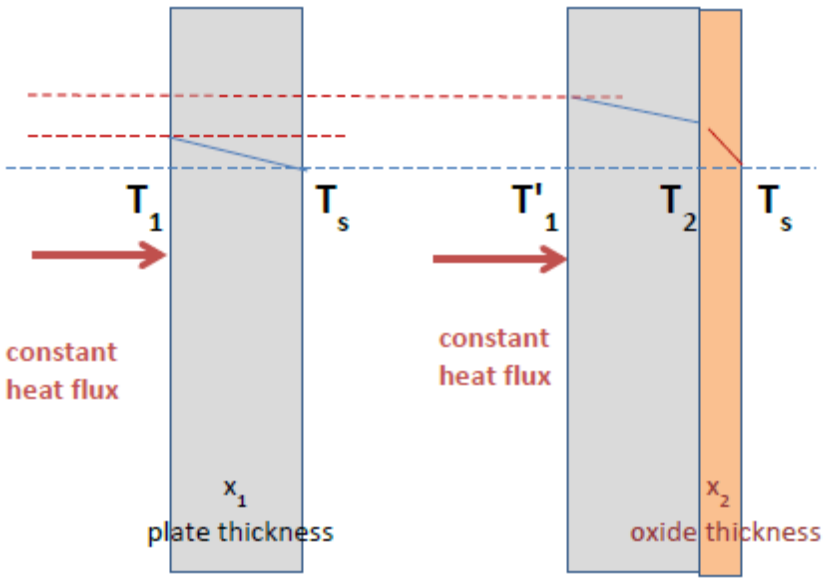

Figure 5-8. Conceptual Diagram of Heat Flow Path

Simplifying the partial differential in the one-dimensional conduction equation to linear differences, the relationship for heat flow through the wall with a ‘clean’ surface is

$$q = -k_1 \frac{(T_s - T_1)}{x_1}$$

where k_1 = thermal conductivity of the solid material comprising the wall
x_1 = thickness of the wall

With the addition of another layer of material, such as an oxide layer, as illustrated in Figure 5.8, the flow of heat (still at the same constant heat flux), can be expressed as

$$q = \frac{-k_1}{x_1}(T_s - T_1) = \frac{-k_1}{x_1}(T_2 - T_1') = \frac{-k_2}{x_2}(T_s - T_2)$$

where k_2 = thermal conductivity of the oxide layer
x_2 = thickness of the oxide layer

For a constant heat flux, the addition of the second layer will result in an increase in T_1 by the amount ($T_2 - T_s$), the temperature difference across the additional layer. The question of interest here is how much it could increase. This relationship was applied to the geometry of the 24P DSC, which consists primarily of fuel rods and steel plates of various thicknesses, using heat flux values based on the decay heat loads for this system assumed over time. A typical thermal conductivity of 0.38 W/m-°C (0.22 Btu/hr-ft-°F) was used for the oxide layer in these example calculations. (In general, oxides have thermal conductivity values one to two orders of magnitude lower than the original metal.)

The results show that for these relatively low heat flux values, the effect on component temperatures would be quite small, even for very large assumed oxide thicknesses. Figure 5-9 shows the results obtained for a range of assumed oxide thicknesses on the fuel rod cladding for the CE 14x14 fuel in the 24P DSC, with heat flux from the rod based on the range of decay heat loading values spanning approximately 300 years in storage. To facilitate the comparison, the oxide thickness values are expressed in terms of fraction of the clad thickness, from a ratio of 0.001 (i.e., 0.1% of the clad thickness) to 1.0 (i.e., an oxide layer as thick as the cladding itself.).

The results in Figure 5-9 show that for the initial decay heat load of the fuel stored in this DSC, the temperature drop across the oxide layer is quite small; less than a tenth of a degree Celsius, even for a relatively thick postulated oxide layer. At higher decay heat loads, the temperature drop would be larger, as a linear function of heat flux through the layer. Figure 5-10 shows these results for assembly decay heat of 1.0 kW, which is the design-basis maximum decay heat load per assembly permitted in the 24P DSC. Two additional curves are shown for results obtained with an assumed decay heat load of 1.5 kW per assembly, and 2.0 kW per assembly, but these values are hypothetical only, since assemblies with decay heat above 1.0 kW would not be permitted in the 24P DSC. However, the curves in Figure 5-10 show that even at 2.0 kW per assembly, it would require an extremely thick oxide layer to produce a temperature drop of even one-fourth of a degree Celsius through the oxide layer on the fuel rod cladding.

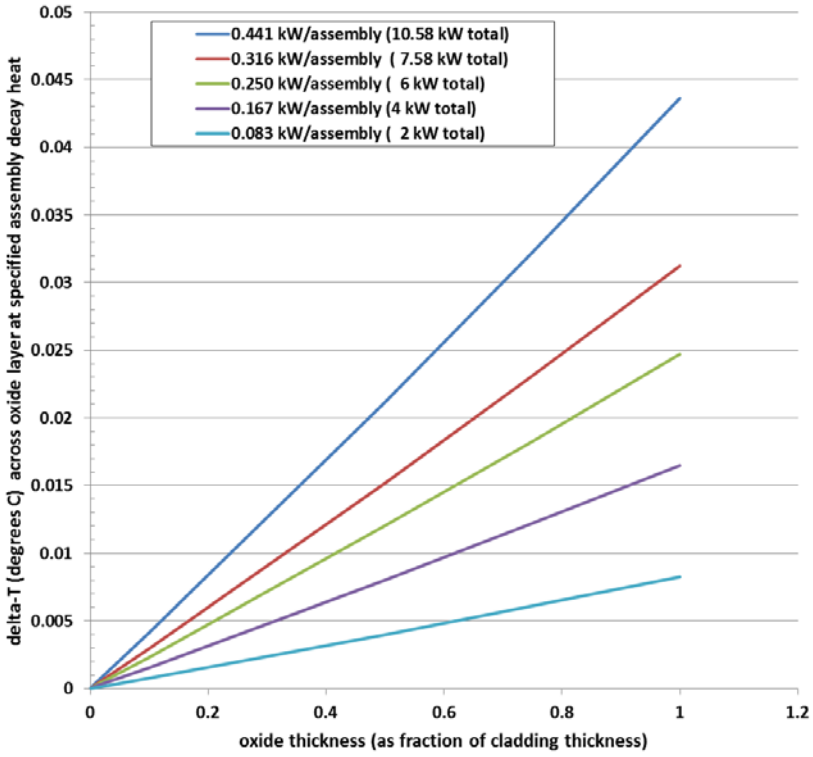

Figure 5-9. Estimated Temperature Drop Across Oxide Layer on Fuel Rod Cladding, for Constant Heat Flux at Postulated Decay Heat Loads over Time

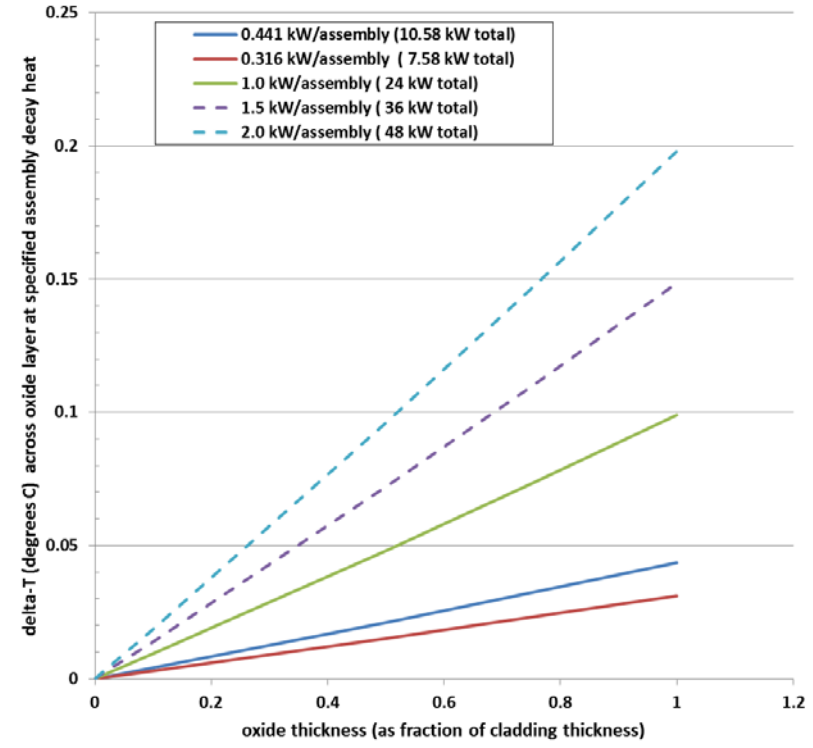

Figure 5-10. Estimated Temperature Drop Across Oxide Layer on Fuel Rod Cladding at Design Basis Decay Heat Loading and Above

The heat flux through the fuel rod cladding is the highest heat flux that would be encountered in the DSC, and therefore provides a reasonable bounding heat flux value for determining temperature drop through postulated oxide layer thicknesses and compositions. Using the simple 1-D conduction equation described above, it is also possible to estimate typical temperature drops across various components of the system for heat flux values based on postulated decay heat loading. Figure 5.11 shows the results obtained for the DSC shell for a surface heat flux corresponding to the total decay heat load in the canister over time. These calculations assumed an oxide layer varying from essentially zero to 3 cm (1.2 in.) thick. The DSC shell is only about 1.27 cm (0.5 in.) thick, so the upper bound implies rather more corrosion than is physically possible, but since this evaluation assumes no change in the steel thickness, it is equivalent to imposing a layer of foreign material of a specified thickness on the outer surface.

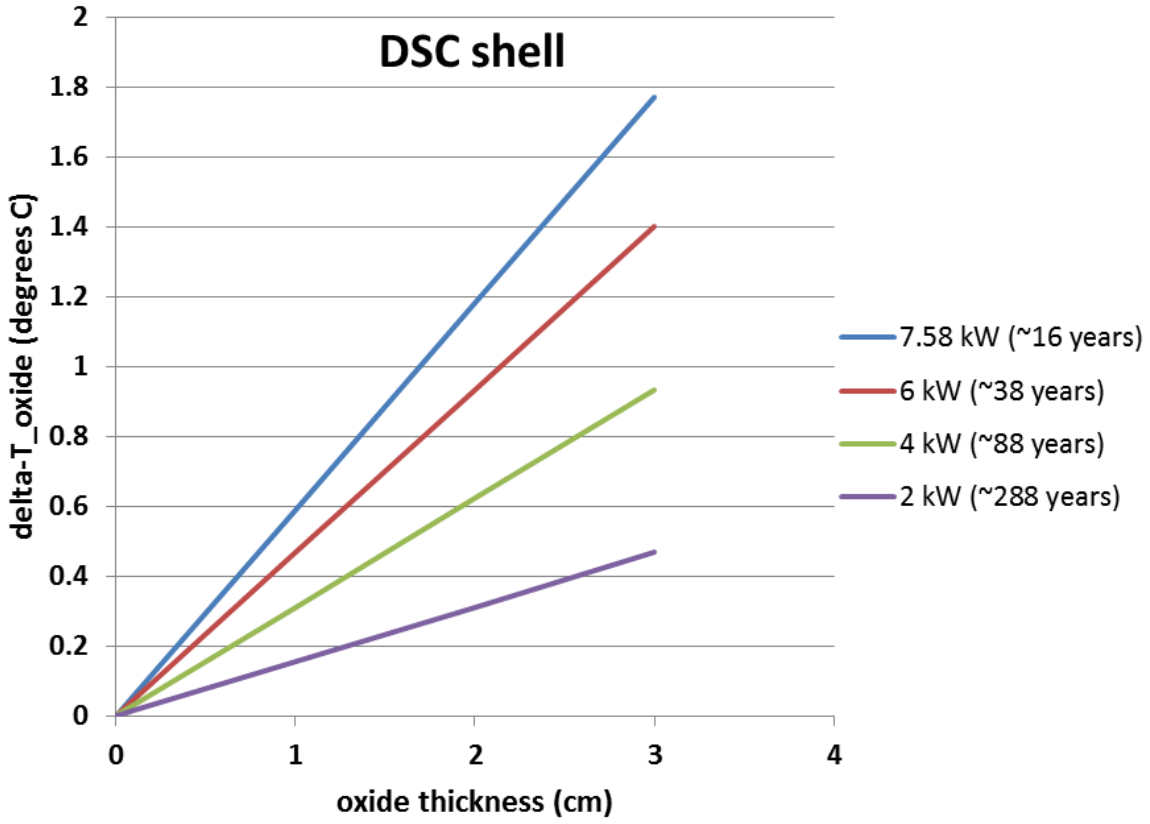

Figure 5-11. Estimated Temperature Drop Across Oxide Layer for Constant Heat Flux through DSC Shell at Postulated Decay Heat Loads over Time

Results of a similar calculation for the thin steel wall of the storage compartment containing the fuel assembly are shown in Figure 5.12, for heat flux values corresponding to the assembly decay heat load of the hottest fuel assembly at the corresponding total decay heat load. The results in Figures 5-9 through 5-12 show that at the relatively low decay heat values for the fuel stored in the 24P DSC in HSM15, the effect on internal component temperatures due to an oxide layer on the metal surface is likely to be quite small. The linear nature of the relationship, however, suggests that systems with significantly higher decay heat loads may be more sensitive to changes in surface conditions than is indicated by the behavior of this particular system.

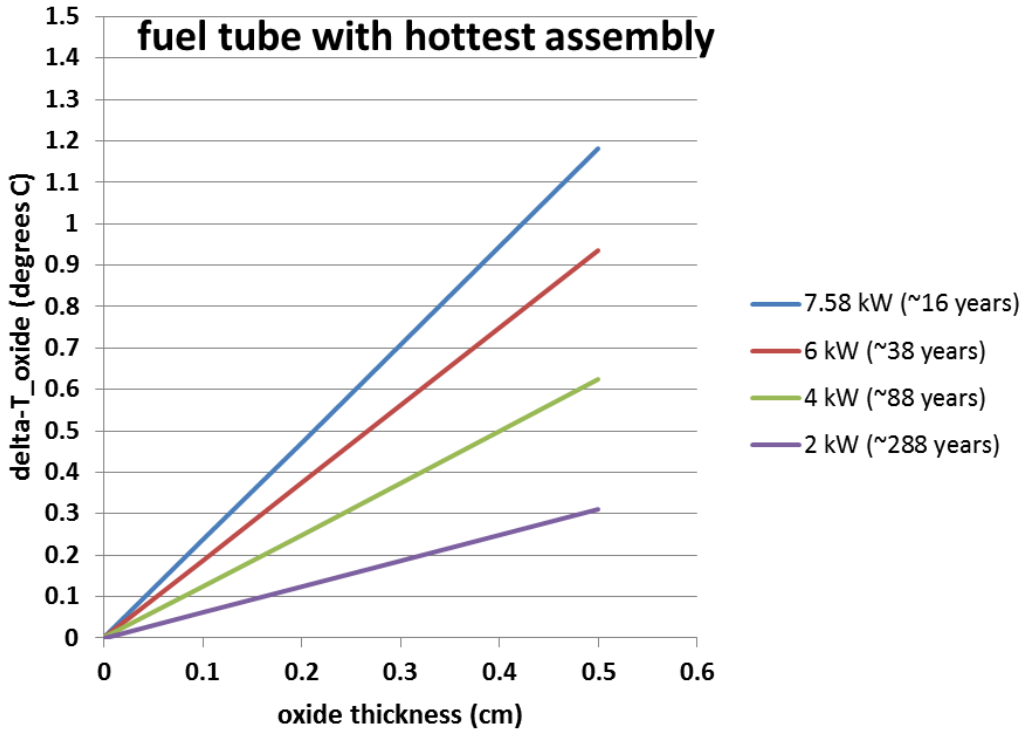

Figure 5-12. Estimated Temperature Drop Across Oxide Layer for Constant Heat Flux through Fuel Storage Compartment Wall at Postulated Decay Heat Loads over Time

This simplified evaluation does not take into consideration the effect of dimension changes that could occur with changes in surface conditions. Such changes are likely to have structural as well as thermal consequences, and are beyond the scope of this study. For metal components, such as steel plates and tubes, it has been fairly well established by archeology that these materials can preserve their original overall geometry even when very highly oxidized, if left undisturbed. The behavior of non-metallic materials would have to be evaluated on an individual basis.

5.2.2 Effect of Assumed Surface Emissivities on System Temperatures

As shown by the previous discussion, changing surface emissivity, which is generally a function of an oxide layer or possibly a debris layer accumulating on the surface, has little effect on temperatures due to conduction or convection heat transfer at the decay heat loading values considered in this study. For this system, the main effect of changing surface emissivity on component temperatures is due to the effect on thermal radiation heat transfer within the system. This is shown by the results obtained with the emissivity sensitivity study matrix described in Section 4.2 and Table 4-3. A total of 30 simulations were run with the STAR-CCM+ model of the 24P DSC in HSM15. As outlined in Table 4-3, the matrix consists of the following set of cases defining postulated variations in component emissivities:

- Case A – base case; all surface emissivities at nominal values
- Case B – bounding case; all surface emissivities assumed at 1.0 (completely black)

- Case C – surfaces inside DSC assumed to remain at base case values; emissivities of module surfaces assumed to increase
  - Case C-1 – changed emissivities increase by 50%
  - Case C-2 – changed emissivities increase to 1.0
- Case D – emissivities of surfaces inside DSC internals assumed to increase; module surfaces remain at base case values
  - Case D-1 – changed emissivities increase by 50%
  - Case D-2 – changed emissivities increase to 1.0

Calculations were performed for each of these cases at five different decay heat loads in the DSC, simulating the decrease in decay heat load from initial loading out to approximately 300 years. The initial loading was 10.58 kW for this particular module, and the decay heat load as of June 2012 (the time of the inspections at the Calvert Cliffs ISFSI) was calculated to be 7.58 kW. The decay heat load values of 6 kW, 4 kW, and 2 kW correspond to the estimated decay heat load for this canister at nominally 38 years, 88 years, and 288 years, respectively.

The effect of surface emissivity on DSC internal component temperatures is illustrated in Figure 5-13 and Figure 5-14. The color graphics in each of these figures show an axial and radial 'slice' through the DSC, capturing the temperature distributions in the 24 fuel assembly regions, the fuel tubes, and the helium backfill gas. Figure 5-13 shows the results for Case A, the base case, with all surface emissivities at nominal initial values. Figure 5-14 shows the results for Case B, the bounding case of all surface emissivities assumed to be at 1.0. As expected from the physics of thermal radiation heat transfer, Case B has lower overall peak temperatures on components, and flatter temperature distributions, for the same total decay heat load.

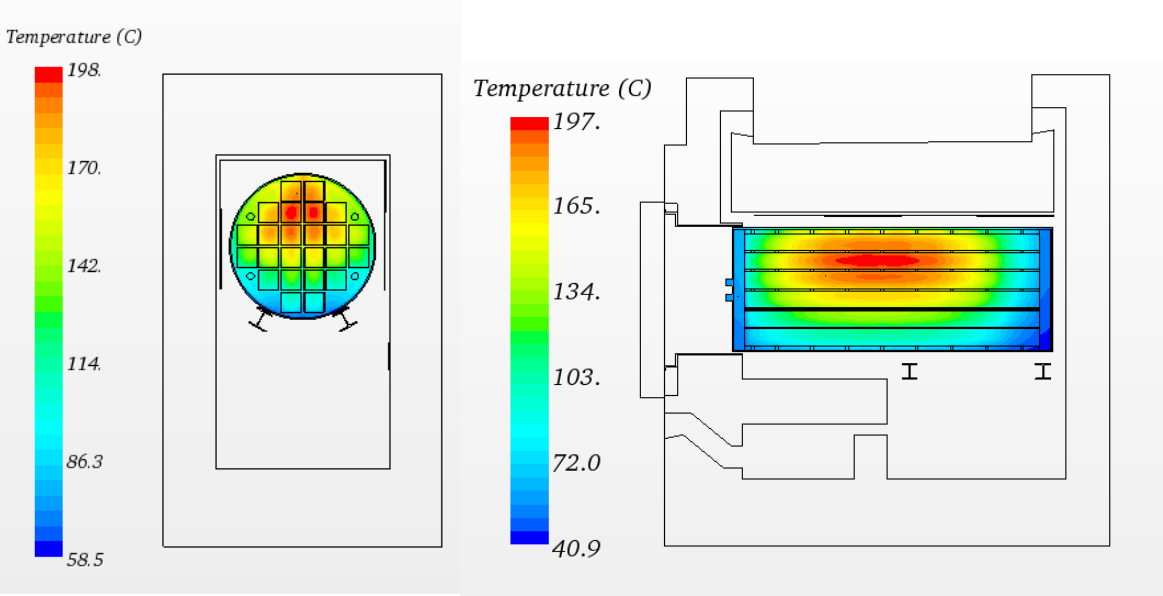

Figure 5-13. Axial and Radial Temperature Contours within the DSC at 7.58 kW Decay Heat Load: Case A (Base Case)

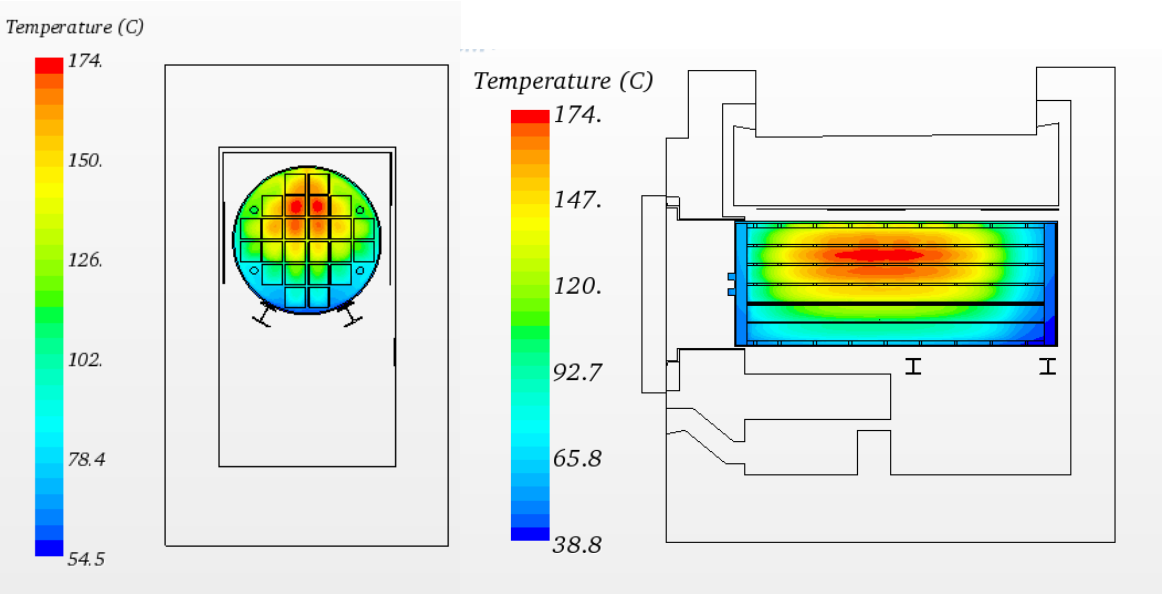

Figure 5-14. Axial and Radial Temperature Contours within the DSC at 7.58 kW Decay Heat Load: Case B (Bounding Case)

This behavior is also illustrated for the emissivities assumed for components within the module, including the outer surface of the DSC, in Figure 5-15 for Case A (base case) and for Case B (the bounding case). For clarity, the module surfaces (i.e., heat shield and inner concrete wall surfaces) have been omitted from these plots, but the effect of emissivity of these surfaces is directly reflected in the DSC shell temperatures. To facilitate the comparison, both color graphic plots are constrained to the same temperature scale. This comparison clearly illustrates the flattening of temperature gradients that is the expected result with increased surface emissivity on all components within the DSC and external to the DSC within the module. As discussed in detail in Section 5.2.1, increased emissivity values tend to increase the amount of heat transfer due to thermal radiation and has the effect of smearing out temperature differences in a system.

This effect is further illustrated by the comparison in Figure 5-16 for Case C. For this case, the emissivities of surfaces inside the DSC are unchanged from the base case (Case A), but the emissivities of the surfaces in the surrounding module are assumed to increase, by 50% in Case C-1, and to the bounding limit of 1.0 in Case C-2. In comparison to Case A (in Figure 5-15), it can be seen that the temperature gradients on the DSC are flattened somewhat in Case C-1, but still reach nearly the same peak value. For Case C-2, however, the color plot shows essentially the same temperature distribution as the bounding Case B in Figure 5-15. (Note that the plots in Figure 5-16 are also constrained to the same temperature scale as the plots in Figure 5-15, to facilitate this comparison.)

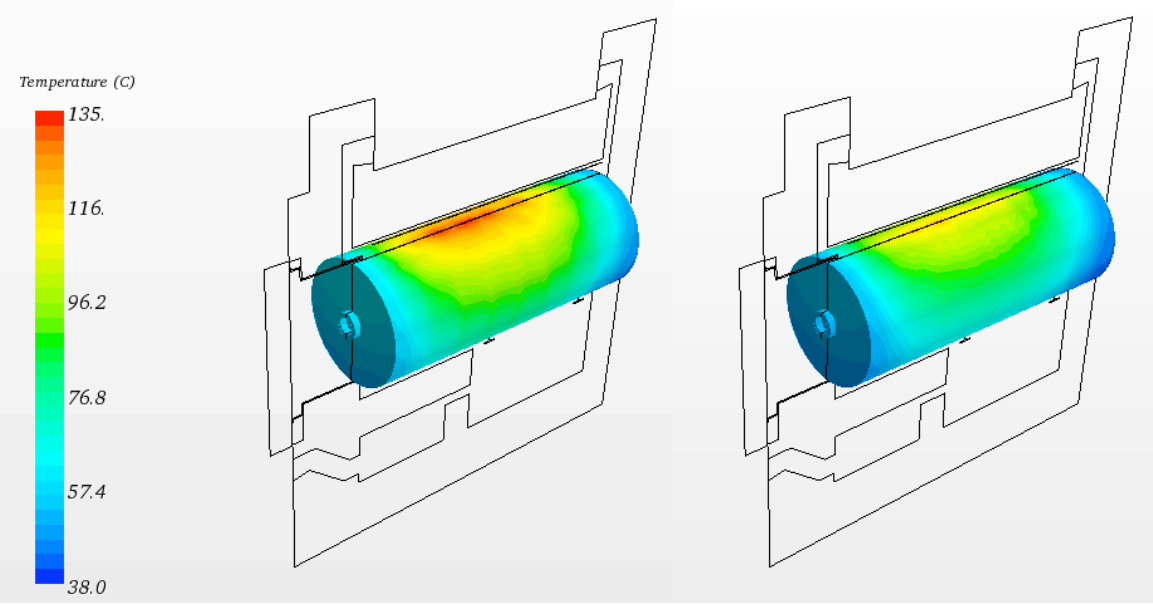

(Case A) (Case B)

Figure 5-15. DSC Temperature Contours at 7.58 kW Decay Heat Load: Case A (Base Case) and Case B (Bounding Case)

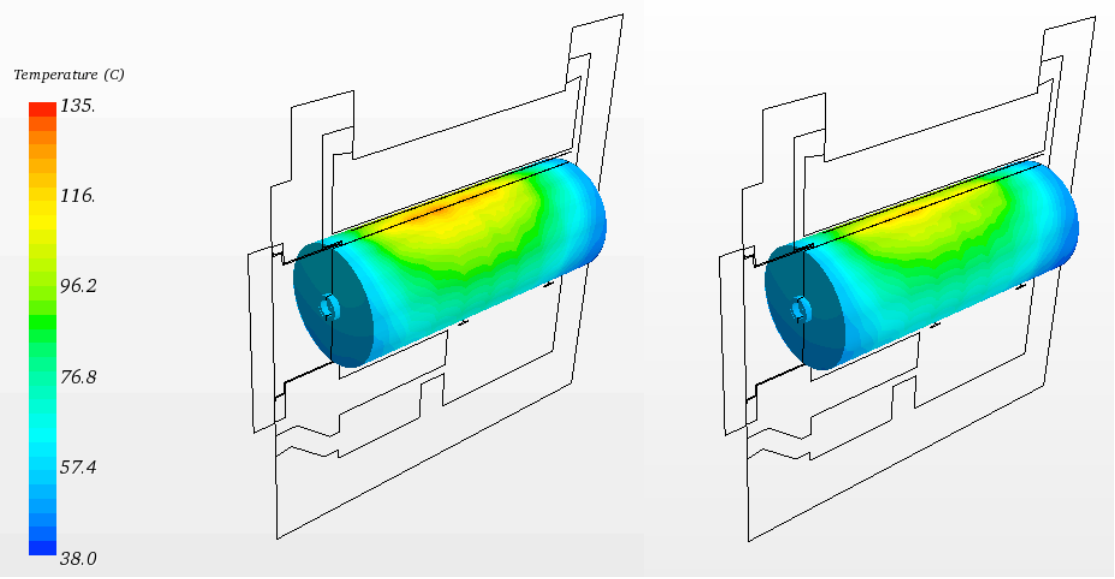

(Case C-1) (Case C-2)

Figure 5-16. DSC Temperature Contours at 7.58 kW Decay Heat Load: Case C-1 (50% Increase in Module Surface Emissivities) and Case C-2 (Bounding Emissivities for Module Surfaces)

The effect on DSC shell temperatures due to the emissivity assumptions for Case D is illustrated in Figure 5-17. The results of this case show that changes in the emissivities of the DSC internal components have little effect on the DSC shell temperatures, when the module emissivities remain the same. This is the expected result, since the total decay heat to be removed is unchanged, and the heat flux at the DSC surface would be essentially the same. Surface emissivities of the module components have more effect on the DSC shell temperatures, since

these parameters influence the rate of heat transfer from the surface by thermal radiation, as is illustrated by the results shown for Case C in Figure 5-16.

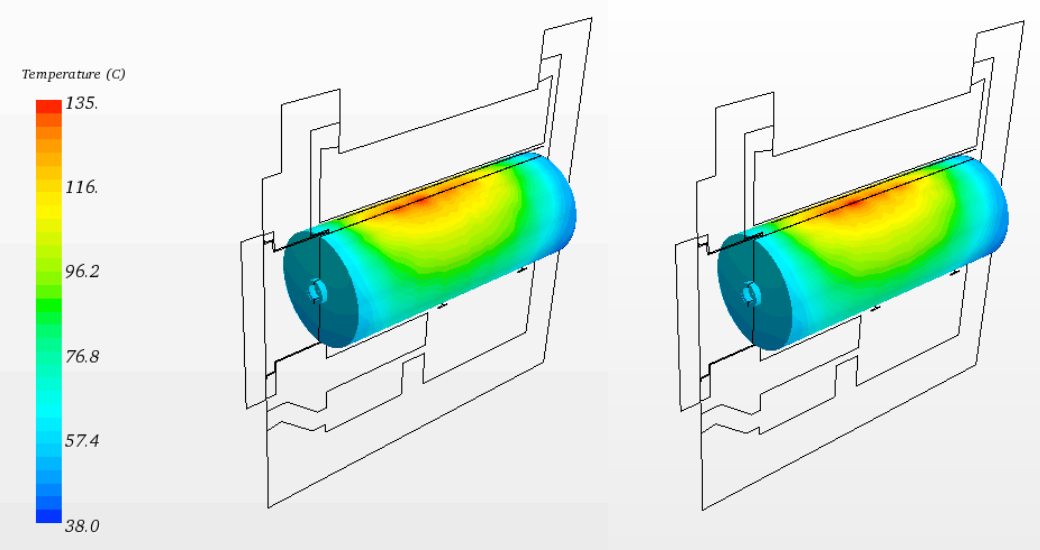

(Case D-1) (Case D-2)

Figure 5-17. DSC Temperature Contours at 7.58 kW Decay Heat Load: Case D-1 (50% Increase in DSC Internal Surface Emissivities) and Case D-2 (Bounding Emissivities for DSC Internal Surfaces)

The results shown in Figures 5-13 through 5-17 are at a relatively high decay heat load for this system, corresponding to only about 16 years in dry storage. The postulated changes in surface emissivities are more likely to occur over a somewhat longer timeframe, and the decay heat load in the DSC will be decreasing over the course of time that the age-related changes would tend to accumulate. It may therefore be more interesting to examine the effect of changing emissivities over the full range of decay heat loads evaluated in this study. The peak component temperatures obtained for all 30 simulations are presented in Table 5-2. The peak temperatures reported in Table 5-2 are also presented graphically in Figure 5-18, with bar charts comparing the peak temperatures for the concrete surfaces and the heat shield, and in Figure 5-19, for the DSC shell outer surface and the peak fuel cladding temperature, over the range of decay heat values considered, and by extension, over equivalent time in dry storage.

Two observations are immediately apparent from the charts in Figures 5-18 and 5-19. First, the range of variation in peak temperature is relatively small with changes in surface emissivities. Second, the magnitude of the variation decreases significantly with decreasing decay heat load (and therefore with increasing time in dry storage). At these relatively low temperatures in dry storage, even at initial conditions (where severe degradation of surface conditions is unlikely, given that some significant elapse of time is generally necessary for degradation to occur), the temperature gradients are not large, and the scope for changes in temperature with changing emissivity values is therefore not extremely large. This behavior is more clearly illustrated by the set of plots in Figure 5-20, comparing the peak temperatures for Case A (base case, with nominal emissivities) to the results for Case B (bounding case, all emissivities at 1.0). These results show the maximum possible variation in peak temperatures due to surface emissivity changes, for this particular storage configuration. The differences are in general quite small, and

of diminishing significance with time. However, the peak clad temperature variation at high decay heat loads may be of importance to phenomenon such as hydride precipitation, ductile-to-brittle transition temperature, and annealing of radiation damage. Studies of systems at design basis loading are needed to fully characterize this sensitivity parameter over the full range of storage conditions, assuming that at some point systems will actually be loaded at or near thermal design basis.

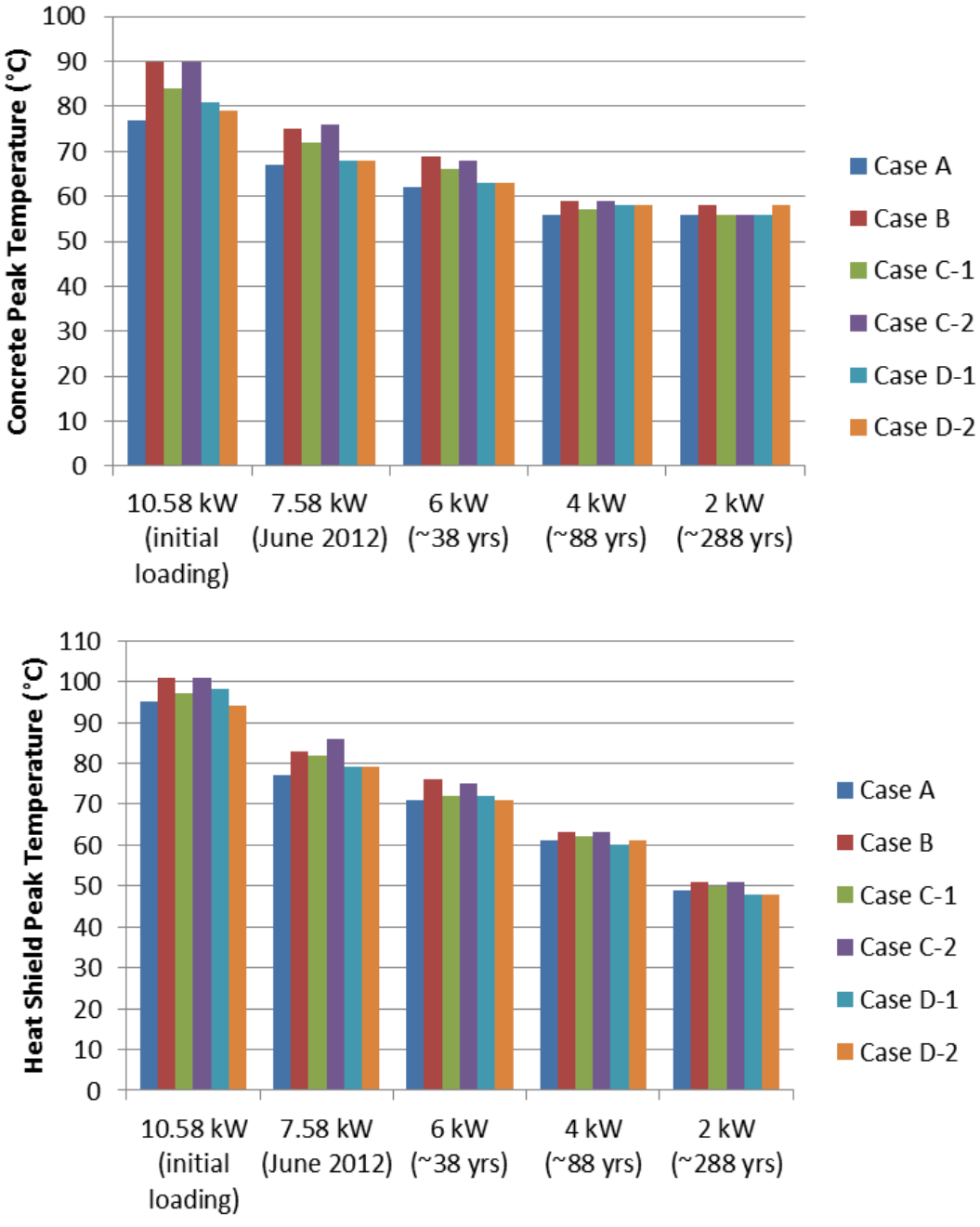

Figure 5-18. Peak Module Component Temperatures for all Cases in the Emissivity Matrix

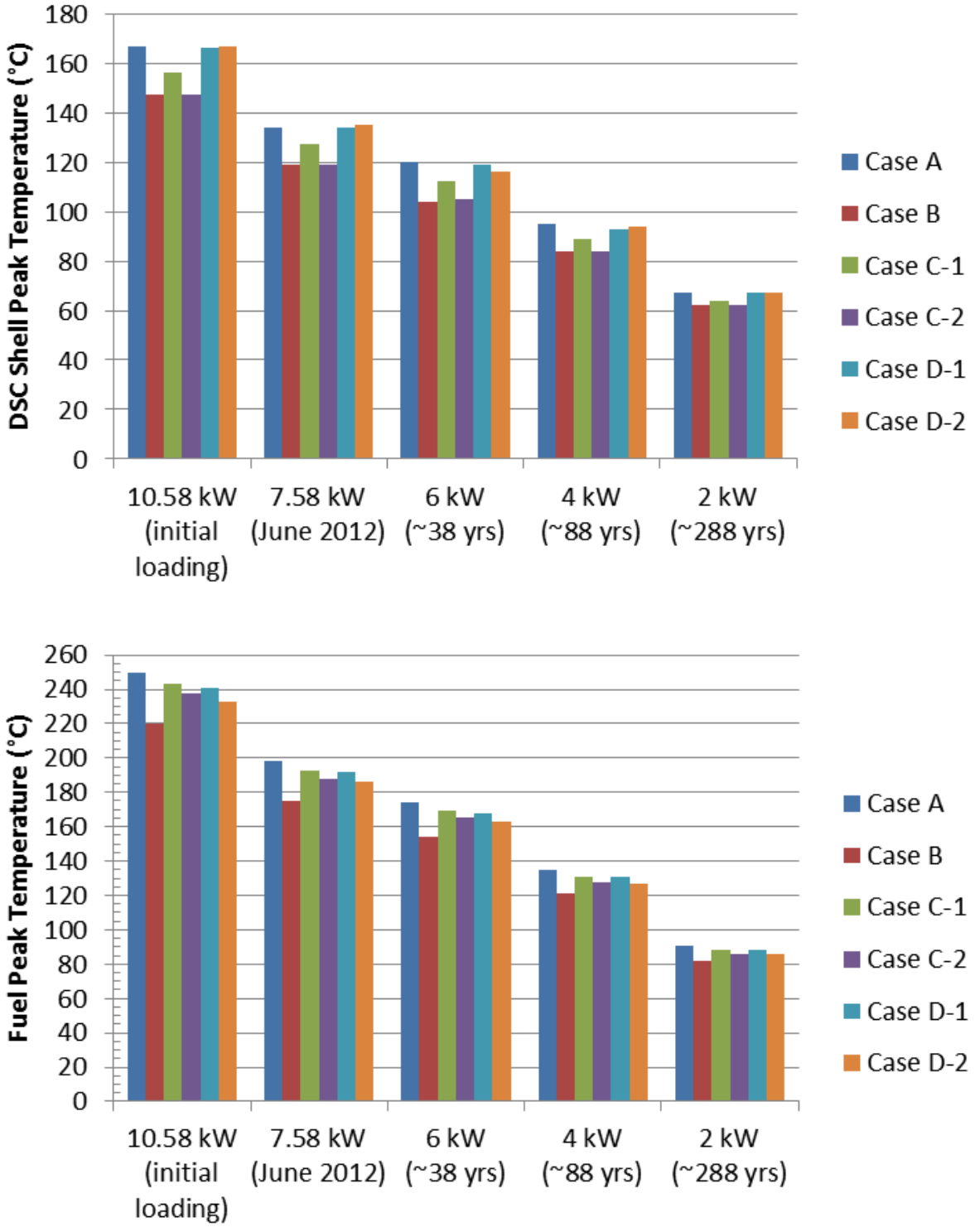

Figure 5-19. Peak Fuel Cladding Temperatures and DSC Shell Temperatures for all Cases in the Emissivity Matrix

Table 5-2. Maximum Component Temperatures in Surface Emissivity Study Cases

	Peak Component Temperatures (°C)			
Case ID	Concrete	DSC Shell	Fuel cladding	Heat Shield
10.58 kW (initial loading)				
Case A	77	167	250	95
Case B	90	147	220	101
Case C-1	84	156	243	97
Case C-2	90	147	238	101
Case D-1	81	166	241	98
Case D-2	79	167	233	94
7.58 kW (at ~16 years)				
Case A	67	134	198	77
Case B	75	119	175	83
Case C-1	72	127	193	82
Case C-2	76	119	188	86
Case D-1	68	134	192	79
Case D-2	68	135	186	79
6 kW (at ~38 years)				
Case A	62	120	174	71
Case B	69	104	154	76
Case C-1	66	112	169	72
Case C-2	68	105	165	75
Case D-1	63	119	168	72
Case D-2	63	116	163	71
4 kW (at ~88 years)				
Case A	56	95	135	61
Case B	59	84	121	63
Case C-1	57	89	131	62
Case C-2	59	84	128	63
Case D-1	58	93	131	60
Case D-2	58	94	127	61
2 kW (at ~288 years)				
Case A	56	67	91	49
Case B	58	62	82	51
Case C-1	56	64	88	50
Case C-2	56	62	86	51
Case D-1	56	67	88	48
Case D-2	58	67	86	48

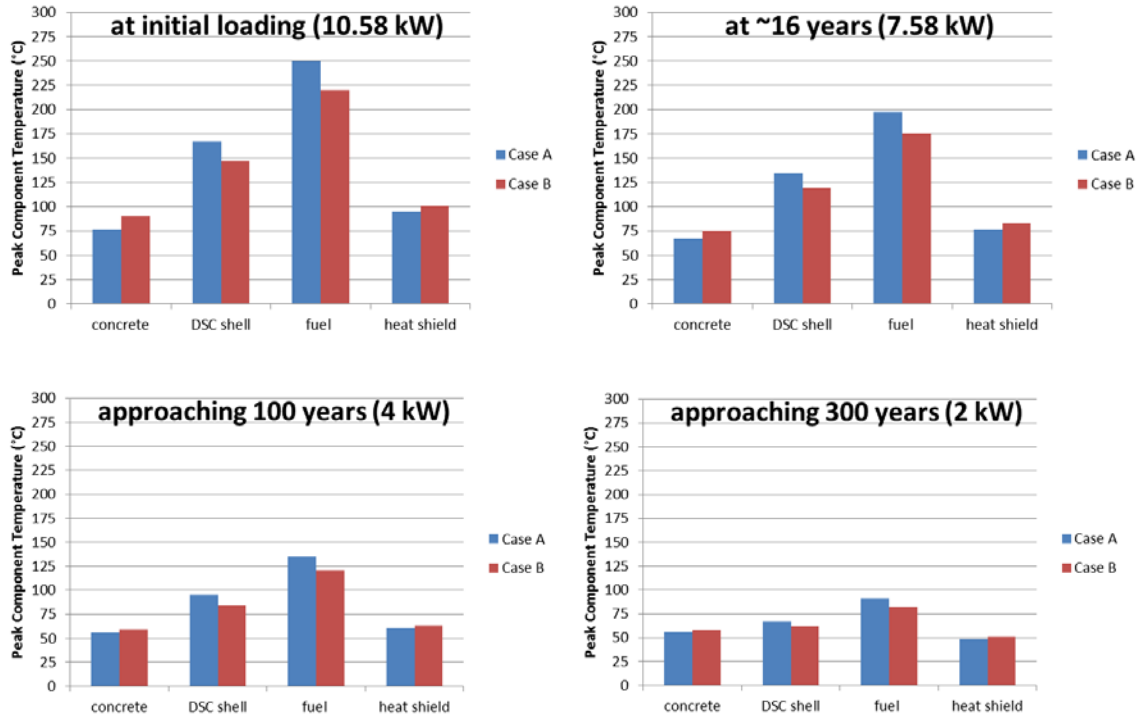

Figure 5-20. Comparison of Peak Component Temperatures for Nominal and Bounding Cases over the Full Range of Decay Heat Values Evaluated

The variations in emissivity assumed for Cases C and D were developed to evaluate the effect of differential changes in surface conditions within the storage system over time. Case C evaluates the possibility of the DSC internals remaining at nominal or design basis conditions, assuming that the inert gas environment can be maintained over the long term, while surfaces exposed to air within the storage module undergo changes that result in increased emissivities. Case D evaluates the opposite possibility, in that the components exposed to ambient air are assumed to maintain essentially constant surface emissivities, but surfaces within the DSC undergo changes that increase surface emissivities. Postulated causes of such changes would include oxidation due to air ingress, or the presence of water vapor due to incomplete vacuum drying. (Case B bounds both Case C and Case D, with the assumption that both the module and canister surfaces undergoing increased emissivity, to the maximum value of 1.0.)

The results obtained for the two variants evaluated in Case C are compared to the base case (Case A) results in Figure 5-21. These plots show the DSC shell outer surface peak temperatures and the peak fuel temperatures. These components tend to show the greatest dependence on surface emissivities, and are indicative of the general sensitivity of system temperatures to such changes in the heat transfer environment. The plots in Figure 5-21 show that the effect is significant only at higher decay heat values, and gradually dwindles to the point of almost disappearing at the lowest decay heat level examined, i.e., 2 kW, corresponding to time in storage approaching 300 years.

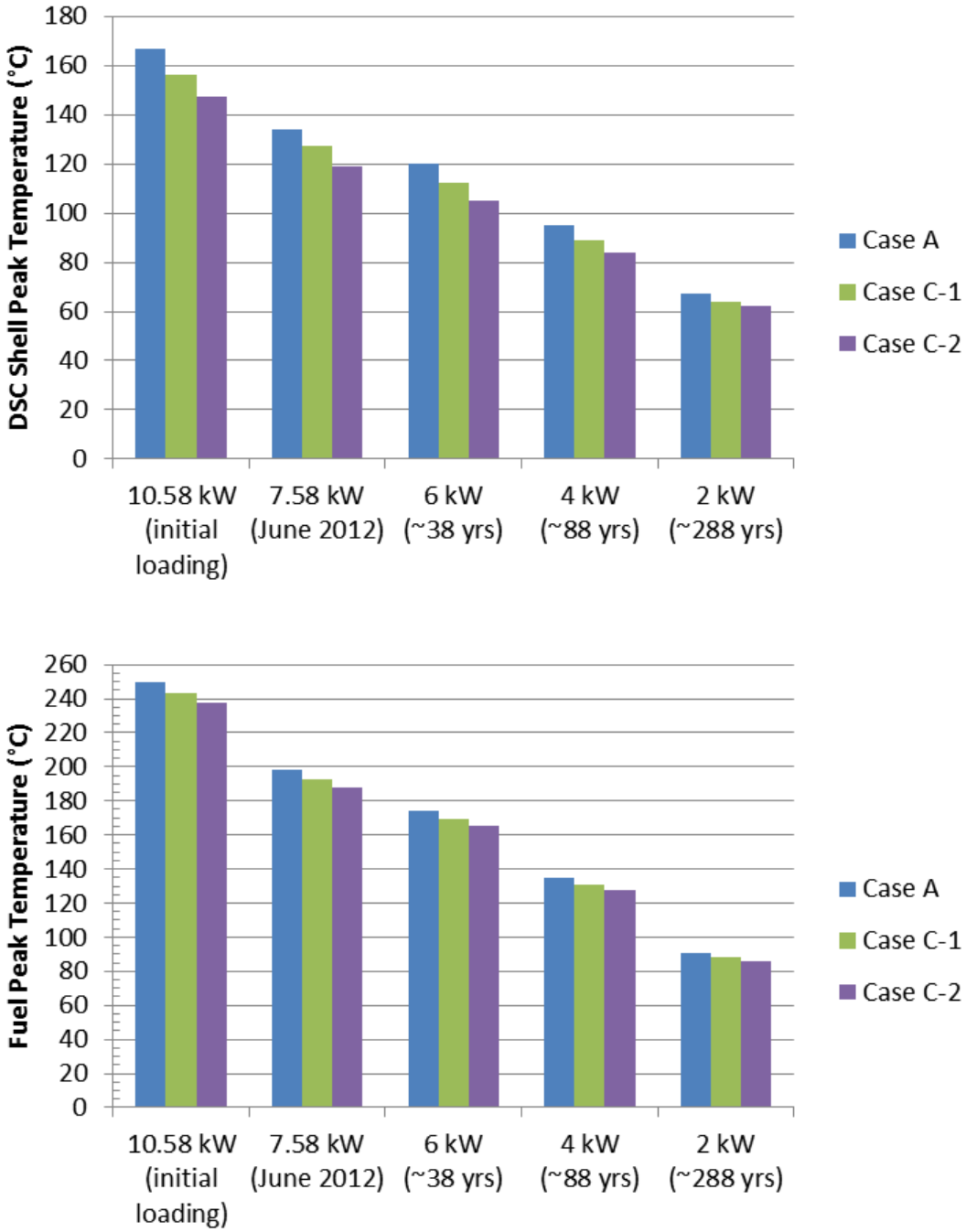

Figure 5-21. Comparison of Peak Component Temperatures for Case C-1 and C-2 (Varying Surface Emissivities for Module and DSC Shell Exterior) to the Nominal Case (Case A) over Full Range of Decay Heat Values Evaluated

The results obtained for the two variants evaluated in Case D are compared to the base case (Case A) results in Figure 5-22. These results are similar to those obtained for the calculations in Case C, except that there is essentially no change in DSC outer shell temperature with the variations in internal surface emissivities. This is because the exterior surface of the DSC

remains at the nominal emissivity, as do the emissivity values for the other surfaces in the HSM module. Therefore, there is essentially no change in the pattern of heat transfer within the HSM module. The only significant change in this scenario is the slight flattening of temperature gradients within the DSC, due to enhanced thermal radiation exchange with increasing emissivities. The magnitude of this effect dwindles with time, due to decreasing decay heat load.

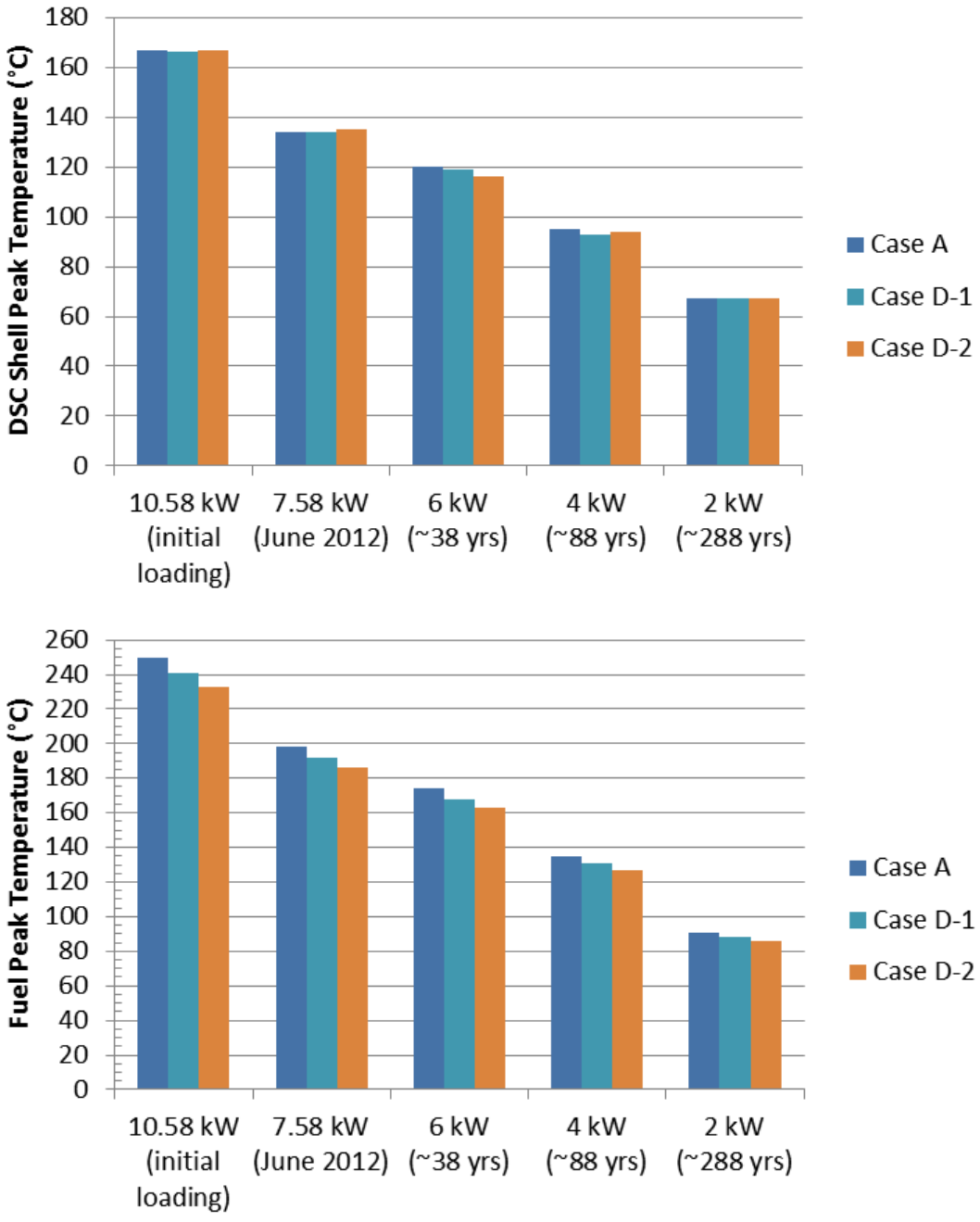

Figure 5-22. Comparison of Peak Component Temperatures for Case D-1 and D-2 (Varying Surface Emissivities for DSC Internal Surfaces Only) to the Nominal Case (Case A) over Full Range of Decay Heat Values Evaluated

5.3 Results of Fuel Assembly Eccentricity Study

This section presents the results obtained for the eccentricity sensitivity study matrix described in Section 4.3. The purpose of this sensitivity study is to evaluate the effect of the assumed position of the fuel assembly within the storage compartment within the canister, since this is in general not known precisely, and cannot readily be determined for any storage system. Due to the limitations of the homogeneous k-effective model used to represent the fuel assemblies within a large system model such as the STAR-CCM+ model of the 24P DSC in HSM15 (discussed in detail in Section 3.2 and Section 4.3), this study evaluates only the effect of the geometric eccentricity of the fuel assembly within the fuel storage compartment. Evaluation of other effects, including contact conductance between the fuel assembly components and the wall, will require additional studies with a detailed COBRA-SFS model of the fuel assembly region.

This study therefore constitutes in effect a 'separate effects' evaluation of the effect of fuel assembly geometry on peak temperatures in this storage system. Typically, in thermal evaluations of storage systems, a fuel assembly is assumed to be centered within its individual storage compartment. This assumption is used even in a horizontal system, as a simplifying assumption that is by definition conservative for evaluations of peak cladding temperature. To quantify the effect of this assumption for the Star-CCM+ model of the 24P DSC in HSM15, three possible configurations were considered in this study, including the base case. The matrix consists of the following set of cases defining postulated variations in fuel assembly eccentricity within the storage compartment.

- each assembly centered within its fuel storage compartment (base case)
- each assembly centered on the bottom face of the fuel storage compartment
- each assembly resting on the bottom face of the fuel storage compartment, and also close to one side wall (i.e., tucked into the corner).

Contact conductance between a fuel assembly and the wall is not considered, due to the assumptions and limitations of the modeling approach of treating the fuel assembly as a homogeneous region with an effective conductivity based on decay heat and assembly geometry. Calculations were performed for each of these configurations only for the at-loading decay heat of 10.58 kW for the 24P DSC in HSM15. Based on the very small differences these assembly configuration assumptions make in the fuel effective conductivity, as shown in Section 4.3, the effect of this parameter on system temperatures calculated with the model is expected to be relatively small. Therefore, the sensitivity study was conducted at the highest decay heat for this system, to determine the maximum possible effect for the assumed variation in assembly location.

The effect of variation in assembly eccentricity on DSC internal component temperatures is illustrated in Figure 5-23 with radial cross-sections through the location of peak fuel clad temperature. The differences in temperatures are so small that it was not necessary to artificially constrain the plots to the same temperature scale; the maximum and minimum temperatures are essentially the same for the cases evaluated.

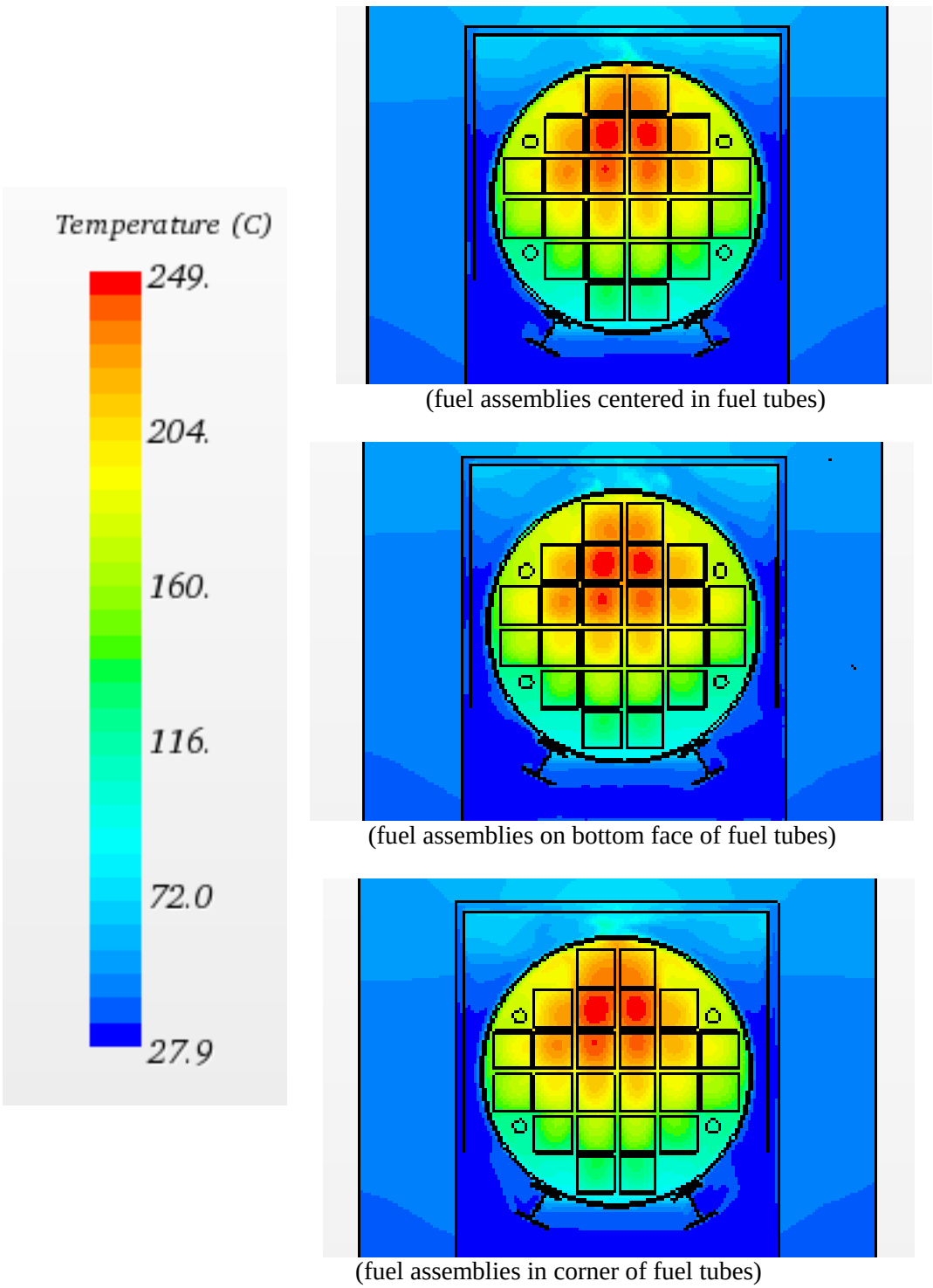

Figure 5-23. Comparison of DSC Internal Temperatures Obtained with Assumed Variations in Fuel Assembly Eccentricity within Fuel Storage Compartment

The peak component temperatures obtained in these evaluations are summarized in Table 5-3. There is no significant change in any of these temperatures with assumed assembly eccentricity, which suggests that the width of the 'edge gap' between the assembly and the fuel storage compartment wall by itself is not an important parameter influencing component temperatures in

the storage system. This is the expected result for this parameter, since the possible geometric variation in the assembly location is quite small within a typical fuel assembly. The change in the conduction path through the helium gas between the fuel and the wall is quite small with these geometry changes, and thermal radiation exchange would also be largely unaffected, due to the relatively small changes in view factors between the fuel rod surfaces and the wall surfaces.

Table 5-3. Maximum Component Temperatures in Assembly Eccentricity Studies

Assembly Position in Storage Compartment	Peak Component Temperatures (°C)			
	Concrete	DSC Shell	Fuel Cladding	Heat Shield
Assembly centered (base case)	77	167	250	95
Assembly on the Bottom	78	166	250	93
Assembly in the Corner	79	167	249	94

This study did not include evaluation of the effect of physical contact of the grid spacer structures or fuel rods with the compartment wall, which would provide paths for conduction heat transfer between assembly components and the compartment wall. The design of typical spacer grids in fuel assemblies would tend to limit such contact to a relatively small area, such that heat transfer due to contact conductance would be expected to have a relatively minor effect on peak temperatures in the fuel assembly. However, the magnitude of this effect has not been quantified, and future work is recommended, to determine the potential magnitude of this effect, and the range of conditions over which it could potentially be important for complete characterization of fuel cladding surface temperatures and temperatures of other components in dry storage systems.

6. CONCLUSIONS AND RECOMMENDATIONS

In general, the results of this study have shown that variation in the parameters examined have relatively small effects on peak temperatures and temperature distributions within a storage system initially loaded at approximately 45% of maximum thermal design basis. The results also show that these effects tend to diminish with time, due to the general decrease in temperatures with decreasing decay heat load. In particular, this study suggests that changes in surface emissivities of system components over long periods of time are not expected to have significant effects on overall temperatures for extended storage conditions. However, the uncertainty of the emissivity of cladding with much higher burnup or of newer cladding materials could have a large enough effect on the calculated peak clad temperature that some mechanisms (e.g., hydride reorientation and annealing of radiation damage) could be affected. The planned demonstration of high burnup fuel in a dry storage cask should consider this uncertainty when designing the instrumentation for that project.

The evaluations of the effect of backfill gas composition on DSC surface temperature distribution suggest that measurements may provide information to assist in monitoring for evidence of the possibility of SCC of the DSC welds. However, it must be noted that these temperature differences are due to significant natural recirculation of the backfill gas within the 24P canister. Canister designs that do not have significant natural circulation flow paths around the basket would not show the variation in the top-to-side temperature difference with fill gas composition observed in this study. The possibility of using this behavior to detect temperature differences that could potentially provide information on backfill gas composition is limited to canisters of similar design to the 24P DSC.

The effect of eccentricity of the fuel assemblies within the basket was shown to be negligible when using the homogeneous k_{eff} model to represent the fuel assemblies, and ignoring potential effects due to contact conduction.

6.1 Recommendations for Future Work

Further investigation of modeling of natural circulation behavior within enclosed volumes is strongly recommended, to verify and validate the accuracy of predicted flow fields obtained with CFD models of gas flow dynamics within a dry storage canister. Preliminary evaluations have shown that the Boussinesq approximation approach can produce a reasonably accurate solution for the range of conditions evaluated in this study, even though the temperature differences exceed the recommended range for this model. This is particularly important for evaluations for vertical systems, and for evaluations in horizontal and vertical systems at higher decay heat loads, such as values approaching system design-basis limits. Temperatures and temperature differences in such systems will generally be much larger than those encountered in this study of a DSC that was initially loaded at less than 50% of thermal design basis maximum.

Specific recommendations developed in this study can be summarized as follows.

1. At low decay heat loadings, changes in surface emissivities of components of the canister and storage module have been shown to have only a minor effect on system peak temperatures, and this effect diminishes with time, due to decreasing decay heat load.

However, this study should be extended to systems at thermal design basis and to systems without significant internal natural convection heat transfer within the DSC. At higher decay heat loading, and with the generally steeper temperature gradients in systems that rely on thermal radiation and conduction only, without convection, to remove heat from the fuel assemblies, the effect of surface emissivities may have a greater influence on peak temperatures and temperature distributions than are indicated by the necessarily limited scope of the current study.

2. The homogeneous effective conductivity model used by necessity in this study with a CFD model of the storage system allowed only limited evaluation of the effect of fuel assembly eccentricity within the storage compartment. Additional work is needed with a detailed model that can take into account conduction due to contact between the fuel assembly structure and the compartment wall in a multi-assembly canister model. The specific recommendation is to develop a detailed model using the COBRA-SFS code for representative horizontal and vertical systems.

7. REFERENCES

ANSI/ANS-5.1-2004. 2004. American National Standard for Decay Heat Power in Light Water Reactors. American Nuclear Society, La Grange Park, Illinois, USA.

ANSYS, Inc. 2012. *FLUENT Users Guide*, version 14.5. Cecil Township, Pennsylvania.

Bahney III RH and TL Lotz, 1996. *Spent Nuclear Fuel Effective Thermal Conductivity Report.* BBA000000-01717-5705-00010 Rev. 00. TRW Environmental Safety Systems, Inc., Fairfax, Virginia.

Carslaw HS and JC Jaeger. 1986. **Conduction of Heat in Solids**, 2nd Edition. Oxford University Press, New York.

CD-adapco. 2012. STAR-CCM+ 7.02.011 (computer software). CD-Adapco, Melville, New York.

CD-adapco Group. 2004. *STAR-CD User Guide, Version 3.20*. CD adapco Group, London.

Creer, J.M., T.E. Michener, M.A. McKinnon, J.E. Tanner, E.R. Gilbert, R.L. Goodman, D.A. Dziadosz, E.V. Moore, H.S. McKay, D.P. Batalo, D.H. Schoonen, M. Jensen, and C. Mullen. 1987. ***TN-24P PWR Spent Fuel Storage Cask: Testing and Analyses.*** EPRI NP-5128, Palo Alto, California: Electric Power Research Institute.

Davis, R.B. 1980. *Data Report for the Nondestructive Examination of Turkey Point Spent Fuel Assemblies B02, B03, B17, B41, and B43.* HEDL-TME-79-68, Hanford Engineering Development Laboratory, Richland, Washington.

Hanson BD, H Alsaed, C Stockman, D Enos, RM Meyer, and K Sorenson. 2012. *Used Fuel Disposition Campaign – Gap Analysis to Support Extended Storage of Used Nuclear Fuel.* FCRD-USED-2011-000136 Rev. 0, U.S. Department of Energy, Washington, D.C.

Kesterson R, R Sindelar, D Vinson. 2013. *Used Fuel Disposition Campaign – Used Nuclear Fuel Characteristics at End of Life.* FCRD-UFD-2013-000130, U.S. Department of Energy, Washington, D.C.

McKinnon, M.A., T.E. Michener, M.F. Jensen, and G.R. Rodman. 1987. ***Testing and Analysis of the TN-24P PWR Spent-Fuel Dry Storage Cask Loaded with Consolidated Fuel.*** EPRI NP-6191, Palo Alto, California: Electric Power Research Institute.

Michener TE, DR Rector, JM Cuta, RE Dodge, and CW Enderlin. 1995. *COBRA-SFS: A Thermal-Hydraulic Code for Spent Fuel Storage and Transportation Casks*. PNL-10782, Pacific Northwest Laboratory, Richland, Washington.

NIST. 2010. **NIST Standard Reference Database 23:** *NIST Reference Fluid Thermodynamic and Transport Properties – REFPROP, Version 9.0.* U.S. Department of Commerce, Technology

Administration, National Institute of Standards and Technology, Standard Reference Data Program, Gaithersburg, Maryland.

NRC. 1990. *SCDAP/RELAP5/MOD2 Code Manual, Volume 4: MATPRO – A Library of Materials Properties for Light-Water-Reactor Accident Analysis.* NUREG/CR-5273. US Nuclear Regulatory Commission, Washington, D.C.

Sanders T, K Seager, Y Rashid, P Barrett, A Malinauskas, R Einziger, H Jordan, T Duffey, S Sutherland and P Reardon. 1993. *A Method for Determining the Spent Fuel Contribution to Transport Cask Containment Requirements.* SAND90-2406, TTC-1019. Sandia National Laboratories, Albuquerque, New Mexico.

Sandoval RP, et al., *Estimate of CRUD Contribution to the Shipping Cask Containment Requirements*. SAND88-1358, Sandia National Laboratory, January 1991.

Suffield SR, JA Fort, HE Adkins, JM Cuta, BA Collins, and ER Siciliano. 2012. *Thermal Modeling of NUHOMS HSM15 and HSM-1 Storage Module at Calvert Cliffs Nuclear Power Station ISFSI*. PNNL-21788, Pacific Northwest National Laboratory, Richland, Washington.

Van Wylen GJ and RE Sonntag. 1973. **Fundamentals of Classical Thermodynamics**. John Wiley and Sons, Inc., New York.

Appendix A

The material properties used in the STAR-CCM+ HSM15 model for the various canister gas compositions are listed in Tables A-1 through A-5. The gas composition is given in molar fraction.

Table A-1. Gas Composition 1.0 Helium

Helium				
Temperature [K]	Density [kg/m3]	Specific Heat [kJ/kg-K]	Thermal Conductivity [W/m-K]	Dynamic Viscosity [kg/m-s]
200	0.24053	5.1934	0.11798	15.142
210	0.22908	5.1934	0.122	15.647
220	0.21868	5.1933	0.12596	16.145
230	0.20918	5.1933	0.12986	16.636
240	0.20047	5.1933	0.13372	17.122
250	0.19245	5.1933	0.13754	17.602
260	0.18505	5.1933	0.1413	18.077
270	0.1782	5.1932	0.14503	18.547
280	0.17184	5.1932	0.14871	19.013
290	0.16592	5.1932	0.15236	19.473
300	0.16039	5.1932	0.15597	19.93
310	0.15522	5.1932	0.15955	20.382
320	0.15037	5.1932	0.16309	20.831
330	0.14582	5.1932	0.1666	21.275
340	0.14153	5.1932	0.17008	21.716
350	0.13749	5.1932	0.17353	22.154
360	0.13367	5.1932	0.17695	22.588
370	0.13006	5.1932	0.18034	23.019
380	0.12664	5.1932	0.18371	23.446
390	0.12339	5.1931	0.18705	23.871
400	0.12031	5.1931	0.19037	24.292
410	0.11738	5.1931	0.19366	24.711
420	0.11458	5.1931	0.19692	25.127
430	0.11192	5.1931	0.20017	25.54
440	0.10938	5.1931	0.20339	25.951
450	0.10695	5.1931	0.20659	26.359
460	0.10462	5.1931	0.20977	26.764
470	0.1024	5.1931	0.21293	27.167
480	0.10026	5.1931	0.21608	27.568
490	0.098219	5.1931	0.2192	27.967
500	0.096255	5.1931	0.2223	28.363
510	0.094368	5.1931	0.22538	28.757
520	0.092554	5.1931	0.22845	29.149
530	0.090808	5.1931	0.2315	29.539
540	0.089127	5.1931	0.23453	29.927
550	0.087507	5.1931	0.23755	30.313
560	0.085945	5.1931	0.24055	30.697
570	0.084437	5.1931	0.24354	31.079
580	0.082982	5.1931	0.24651	31.46
590	0.081576	5.1931	0.24946	31.838
600	0.080217	5.1931	0.2524	32.215

Table A-1. (cont.)

Helium				
Temperature [K]	Density [kg/m3]	Specific Heat [kJ/kg-K]	Thermal Conductivity [W/m-K]	Dynamic Viscosity [kg/m-s]
610	0.078902	5.1931	0.25532	32.59
620	0.07763	5.1931	0.25824	32.964
630	0.076398	5.1931	0.26113	33.335
640	0.075204	5.1931	0.26402	33.706
650	0.074047	5.1931	0.26689	34.074
660	0.072926	5.1931	0.26974	34.441
670	0.071838	5.1931	0.27259	34.807
680	0.070781	5.1931	0.27542	35.17
690	0.069756	5.1931	0.27824	35.533
700	0.068759	5.1931	0.28105	35.894
710	0.067791	5.1931	0.28385	36.254
720	0.06685	5.1931	0.28663	36.612
730	0.065934	5.1931	0.2894	36.969
740	0.065043	5.1931	0.29217	37.324
750	0.064176	5.1931	0.29492	37.679
760	0.063332	5.1931	0.29766	38.031
770	0.06251	5.1931	0.30039	38.383
780	0.061709	5.1931	0.30311	38.733
790	0.060928	5.1931	0.30582	39.083
800	0.060166	5.1931	0.30852	39.431
810	0.059423	5.1931	0.31121	39.777
820	0.058699	5.1931	0.31389	40.123
830	0.057992	5.1931	0.31656	40.467
840	0.057302	5.1931	0.31922	40.81
850	0.056627	5.1931	0.32187	41.153
860	0.055969	5.1931	0.32451	41.494
870	0.055326	5.1931	0.32714	41.834
880	0.054697	5.1931	0.32977	42.172
890	0.054083	5.1931	0.33238	42.51
900	0.053482	5.1931	0.33499	42.847
910	0.052894	5.1931	0.33759	43.183
920	0.05232	5.1931	0.34017	43.517
930	0.051757	5.1931	0.34276	43.851
940	0.051207	5.1931	0.34533	44.184
950	0.050668	5.1931	0.34789	44.515
960	0.05014	5.1931	0.35045	44.846
970	0.049623	5.1931	0.353	45.176
980	0.049117	5.1931	0.35554	45.505
990	0.048621	5.1931	0.35808	45.833
1000	0.048135	5.1931	0.3606	46.16

Table A-2. Gas Composition 1.0 Air

Air				
Temperature [K]	Density [kg/m3]	Specific Heat [kJ/kg-K]	Thermal Conductivity [W/m-K]	Dynamic Viscosity [kg/m-s]
81.639	4.4327	1.0694	0.0075281	5.8688
200	1.7455	1.007	0.018217	13.368
210	1.6618	1.0066	0.01904	13.927
220	1.5857	1.0062	0.019852	14.478
230	1.5164	1.006	0.020653	15.019
240	1.4528	1.0058	0.021444	15.551
250	1.3945	1.0058	0.022224	16.075
260	1.3406	1.0058	0.022995	16.591
270	1.2908	1.0059	0.023757	17.099
280	1.2445	1.006	0.02451	17.6
290	1.2015	1.0063	0.025254	18.093
300	1.1613	1.0066	0.025989	18.579
310	1.1237	1.007	0.026717	19.059
320	1.0886	1.0075	0.027437	19.532
330	1.0555	1.0081	0.028149	19.999
340	1.0244	1.0087	0.028853	20.46
350	0.99508	1.0094	0.029551	20.916
360	0.9674	1.0103	0.030242	21.365
370	0.94122	1.0112	0.030926	21.809
380	0.91642	1.0121	0.031604	22.248
390	0.89289	1.0132	0.032276	22.682
400	0.87055	1.0144	0.032942	23.111
410	0.8493	1.0156	0.033602	23.535
420	0.82906	1.0169	0.034257	23.954
430	0.80976	1.0183	0.034906	24.369
440	0.79135	1.0198	0.035549	24.78
450	0.77375	1.0213	0.036188	25.186
460	0.75692	1.023	0.036822	25.588
470	0.74081	1.0247	0.03745	25.987
480	0.72537	1.0264	0.038075	26.381
490	0.71056	1.0282	0.038694	26.772
500	0.69634	1.0301	0.03931	27.159
510	0.68268	1.032	0.039921	27.543
520	0.66955	1.034	0.040528	27.923
530	0.65691	1.0361	0.04113	28.3
540	0.64475	1.0381	0.041729	28.673
550	0.63302	1.0403	0.042324	29.044
560	0.62172	1.0424	0.042916	29.411
570	0.61081	1.0446	0.043503	29.775
580	0.60027	1.0469	0.044088	30.137
590	0.5901	1.0492	0.044668	30.495
600	0.58026	1.0514	0.045246	30.851
610	0.57075	1.0538	0.04582	31.204
620	0.56154	1.0561	0.046391	31.554
630	0.55263	1.0585	0.046959	31.902
640	0.544	1.0608	0.047524	32.248
650	0.53563	1.0632	0.048086	32.591
660	0.52751	1.0656	0.048645	32.931

Table A-2. (contd.)

Air				
Temperature [K]	Density [kg/m3]	Specific Heat [kJ/kg-K]	Thermal Conductivity [W/m-K]	Dynamic Viscosity [kg/m-s]
670	0.51964	1.068	0.049202	33.269
680	0.512	1.0704	0.049755	33.605
690	0.50458	1.0728	0.050306	33.939
700	0.49737	1.0752	0.050855	34.27
710	0.49036	1.0776	0.0514	34.6
720	0.48355	1.08	0.051944	34.927
730	0.47693	1.0824	0.052485	35.252
740	0.47049	1.0848	0.053023	35.576
750	0.46421	1.0872	0.05356	35.897
760	0.45811	1.0896	0.054094	36.217
770	0.45216	1.0919	0.054625	36.534
780	0.44636	1.0943	0.055155	36.85
790	0.44071	1.0966	0.055683	37.164
800	0.4352	1.0989	0.056208	37.477
810	0.42983	1.1012	0.056732	37.787
820	0.42459	1.1035	0.057253	38.096
830	0.41948	1.1058	0.057773	38.404
840	0.41448	1.1081	0.05829	38.709
850	0.40961	1.1103	0.058806	39.014
860	0.40485	1.1125	0.05932	39.316
870	0.40019	1.1147	0.059833	39.618
880	0.39565	1.1169	0.060343	39.917
890	0.3912	1.119	0.060852	40.216
900	0.38686	1.1212	0.061359	40.513
910	0.38261	1.1233	0.061865	40.808
920	0.37845	1.1254	0.062369	41.102
930	0.37438	1.1274	0.062871	41.395
940	0.3704	1.1295	0.063372	41.687
950	0.3665	1.1315	0.063871	41.977
960	0.36268	1.1335	0.064369	42.266
970	0.35894	1.1355	0.064866	42.554
980	0.35528	1.1374	0.065361	42.84
990	0.35169	1.1394	0.065855	43.126
1000	0.34818	1.1413	0.066347	43.41

Table A-3. Gas Composition of 0.5 Helium – 0.5 Air

0.12 Helium - 0.88 Air				
Temperature [K]	Density [kg/m3]	Specific Heat [kJ/kg-K]	Thermal Conductivity [W/m-K]	Dynamic Viscosity [kg/m-s]
200	0.993300679	3.099950777	0.04774675	14.23745713
210	0.945673964	3.099750767	0.049636681	14.76995843
220	0.902422407	3.099550763	0.051498405	15.29395966
230	0.862970988	3.099400756	0.053332156	15.80946082
240	0.826864689	3.099350753	0.055142274	16.31846191
250	0.793653495	3.099300751	0.056931505	16.81996293
260	0.763002393	3.099300751	0.058694586	17.31496388
270	0.734676375	3.099300756	0.06043792	17.80346476
280	0.708345429	3.09940076	0.062159932	18.28646556
290	0.68388455	3.099500765	0.063863695	18.76246632
300	0.661018728	3.099700775	0.065548429	19.23346699
310	0.63963296	3.099900784	0.06721634	19.69896763
320	0.61960724	3.100100794	0.068865371	20.15946817
330	0.600831566	3.100400808	0.070497723	20.61396867
340	0.583135931	3.100750824	0.072115887	21.06446912
350	0.566435331	3.101100841	0.073717486	21.5104695
360	0.550679765	3.10150086	0.075304984	21.95146983
370	0.53577923	3.101950881	0.076877211	22.38847011
380	0.521663723	3.102450905	0.078436382	22.82047035
390	0.508273242	3.102950933	0.079982752	23.24947054
400	0.495557786	3.103500959	0.081517329	23.67347068
410	0.483462351	3.10415099	0.083037955	24.09447078
420	0.471941938	3.104801021	0.084545838	24.51147083
430	0.460961543	3.105501054	0.086044197	24.92497085
440	0.450481167	3.10625109	0.087529851	25.3349708
450	0.440465808	3.107001125	0.08900501	25.74147073
460	0.430880464	3.107801163	0.090469694	26.14447064
470	0.421715135	3.108651204	0.091923917	26.54447049
480	0.412919819	3.109551246	0.093371084	26.9414703
490	0.404494016	3.110451289	0.094805603	27.33547007
500	0.396401726	3.111401334	0.096230871	27.72646983
510	0.388627947	3.112351379	0.097646894	28.11446955
520	0.381150679	3.113351426	0.099055907	28.49996924
530	0.37395742	3.114351474	0.100455693	28.88296891
540	0.367031672	3.115401523	0.10184509	29.26296853
550	0.360356432	3.116451573	0.103229841	29.64046812
560	0.353920201	3.117551625	0.104604217	30.0154677
570	0.347710978	3.118651678	0.105972792	30.38796725
580	0.341718263	3.11975173	0.107332171	30.75846675
590	0.335925055	3.120901784	0.108683519	31.12596625
600	0.330325354	3.122051839	0.110029079	31.49196573
610	0.32490766	3.123201893	0.111366613	31.85496516
620	0.319671472	3.12440195	0.112699456	32.21696459
630	0.31459529	3.125552005	0.114022033	32.575464
640	0.309678113	3.126752061	0.115342246	32.93296336
650	0.304914442	3.127952118	0.116653287	33.28796274
660	0.300293777	3.129152175	0.117957468	33.64096208
670	0.295814616	3.130352232	0.119258143	33.99246139
680	0.29146596	3.131552289	0.120550806	34.34146073

Table A-3. (cont.)

0.12 Helium - 0.88 Air				
Temperature [K]	Density [kg/m3]	Specific Heat [kJ/kg-K]	Thermal Conductivity [W/m-K]	Dynamic Viscosity [kg/m-s]
690	0.287238308	3.132752346	0.121838869	34.68896
700	0.283134661	3.133952403	0.123121181	35.03495928
710	0.279150518	3.13515246	0.124398896	35.37895853
720	0.275274879	3.136352517	0.125668604	35.72095777
730	0.271501743	3.137552573	0.126933717	36.06145699
740	0.267831112	3.13875263	0.128195353	36.3999562
750	0.264262483	3.139902685	0.129451282	36.73745537
760	0.260785359	3.141102742	0.130701472	37.07295459
770	0.257399237	3.142302799	0.131947073	37.40695374
780	0.254098619	3.143452853	0.133186941	37.73945291
790	0.250883003	3.14465291	0.134423368	38.07095203
800	0.247746891	3.145802964	0.135655209	38.40045116
810	0.244690281	3.146953019	0.136881321	38.72795028
820	0.241708174	3.148103073	0.138103994	39.05494938
830	0.238794569	3.149203126	0.139322083	39.37994848
840	0.235954468	3.15035318	0.14053559	39.70394758
850	0.233176868	3.151453232	0.141744515	40.02694663
860	0.230467771	3.152553284	0.142948859	40.3484457
870	0.227816176	3.153653337	0.144149764	40.66844476
880	0.225231583	3.154753389	0.145348368	40.98644381
890	0.222699492	3.155853441	0.146540113	41.30394284
900	0.220223903	3.156903491	0.1477307	41.62044186
910	0.217804816	3.15795354	0.148916709	41.93544087
920	0.215437731	3.15900359	0.150096997	42.2489399
930	0.213121148	3.16005364	0.151277273	42.5619389
940	0.210856067	3.161053687	0.152450689	42.87343788
950	0.208636487	3.162053735	0.153620666	43.18393691
960	0.206462409	3.163053782	0.154789489	43.49293587
970	0.204333833	3.164053829	0.155953737	43.80143485
980	0.202250758	3.165003874	0.157114546	44.10843381
990	0.200207685	3.16595392	0.158273069	44.41493279
1000	0.198204613	3.166953967	0.159425863	44.71993175

Table A-4. Gas Composition of 0.71 Helium – 0.29 Air

0.25 Helium - 0.75 Air				
Temperature [K]	Density [kg/m3]	Specific Heat [kJ/kg-K]	Thermal Conductivity [W/m-K]	Dynamic Viscosity [kg/m-s]
200	0.681734474	3.966413896	0.068708482	14.61184072
210	0.649081033	3.966296669	0.071295978	15.13295944
220	0.619426492	3.966138055	0.073844069	15.64619895
230	0.592371743	3.966050135	0.076353084	16.15155926
240	0.56760457	3.966020828	0.078831282	16.65104037
250	0.544819824	3.965991521	0.081281308	17.14364228
260	0.523792181	3.965991521	0.083694198	17.63036498
270	0.504354928	3.965950135	0.086082191	18.11120848
280	0.486289808	3.966008748	0.088439699	18.58717278
290	0.469502861	3.966067362	0.090773799	19.05655095
300	0.453812208	3.966184589	0.093081708	19.52175684
310	0.439138026	3.966301816	0.095367601	19.98166966
320	0.425393424	3.966419043	0.097627502	20.43741022
330	0.412505651	3.966594883	0.099865581	20.88756464
340	0.400358509	3.966800031	0.102084129	21.33413292
350	0.388898037	3.967005178	0.104281008	21.776822
360	0.378082514	3.967239632	0.106458474	22.21492495
370	0.367855047	3.967503393	0.10861548	22.64944176
380	0.358166332	3.967796461	0.110756211	23.07937244
390	0.348972921	3.968048142	0.11287875	23.50671698
400	0.340245508	3.968370516	0.114986184	23.92947538
410	0.331943579	3.968751504	0.117074407	24.34964765
420	0.32403248	3.969132492	0.119144512	24.76623379
430	0.316495835	3.969542786	0.121203769	25.17952686
440	0.309301922	3.969982388	0.123244958	25.58994072
450	0.302426087	3.970421989	0.125272262	25.99706152
460	0.295843676	3.970890897	0.127285703	26.40088925
470	0.289552967	3.971389112	0.129285299	26.80213084
480	0.283512237	3.971916634	0.131276312	27.2007863
490	0.277729057	3.972444156	0.133249333	27.59685563
500	0.272173221	3.973000984	0.13520961	27.98992495
510	0.266835936	3.973557813	0.137157153	28.38040814
520	0.261702652	3.974143948	0.139096169	28.76859826
530	0.256763974	3.974730083	0.141022474	29.15449531
540	0.252008988	3.975345525	0.142935031	29.53780623
550	0.247426074	3.975960967	0.144841187	29.91882408
560	0.243007251	3.976605715	0.146733613	30.29754887
570	0.23874383	3.977250464	0.148618613	30.67398058
580	0.234629241	3.977895213	0.150490941	31.04882616
590	0.230651866	3.978569268	0.152351639	31.42067174
600	0.22680736	3.979243324	0.154204929	31.79122426
610	0.22308774	3.979917379	0.156046594	32.15919063
620	0.219492301	3.980620742	0.157884052	32.52615701
630	0.216007197	3.981294797	0.15970567	32.88983032
640	0.212631016	3.981998159	0.161525163	33.2529175
650	0.209360119	3.982701521	0.163332014	33.61329774
660	0.206187939	3.983404884	0.165128285	33.97209185
670	0.203112354	3.984108246	0.166921416	34.32959289
680	0.20012609	3.984811608	0.168702944	34.68438699

Table A-4. (cont.)

0.25 Helium - 0.75 Air				
Temperature [K]	Density [kg/m3]	Specific Heat [kJ/kg-K]	Thermal Conductivity [W/m-K]	Dynamic Viscosity [kg/m-s]
690	0.197223993	3.98551497	0.170478132	35.0383019
700	0.194406164	3.986218333	0.172245958	35.39050987
710	0.19167038	3.986921695	0.174007451	35.74113171
720	0.189009366	3.987625057	0.175757345	36.08975354
730	0.186418778	3.988328419	0.177500907	36.43708231
740	0.183898615	3.989031782	0.179241366	36.78241108
750	0.181448171	3.989705837	0.180972273	37.12715372
760	0.179060877	3.990409199	0.182695833	37.46948249
770	0.176736026	3.991112562	0.18441307	37.81093205
780	0.174469981	3.991786617	0.186122966	38.15067469
790	0.172262035	3.992489979	0.18782756	38.48983119
800	0.17010855	3.993164035	0.189525833	38.82698768
810	0.168009526	3.99383809	0.191216772	39.16214418
820	0.165962033	3.994512146	0.19290241	39.49700761
830	0.163961726	3.995156894	0.194581731	39.82987105
840	0.162011535	3.99583095	0.196254737	40.16173448
850	0.160104186	3.996475699	0.197921428	40.49301177
860	0.158244023	3.997120447	0.199581805	40.82258214
870	0.15642377	3.997765196	0.20123688	41.15085943
880	0.154648583	3.998409945	0.20288991	41.47713673
890	0.152910376	3.999054693	0.204532361	41.80312096
900	0.151210665	3.999670135	0.20617378	42.12810519
910	0.149549452	4.000285577	0.207808888	42.45179635
920	0.147924511	4.000901019	0.209434425	42.77378058
930	0.146333723	4.001516461	0.211062195	43.09547174
940	0.144778501	4.002102596	0.212679385	43.41586983
950	0.143254501	4.002688732	0.214291274	43.73485406
960	0.141761723	4.003274867	0.215902136	44.05295909
970	0.140300166	4.003861002	0.217506691	44.37035718
980	0.13886983	4.00441783	0.219105946	44.6864622
990	0.137467079	4.004974659	0.220703172	45.0018603
1000	0.136091912	4.005560794	0.222290818	45.31596532

Table A-5. Gas Composition of 0.88 Helium – 0.12 Air

0.5 Helium – 0.5 Air				
Temperature [K]	Density [kg/m3]	Specific Heat [kJ/kg-K]	Thermal Conductivity [W/m-K]	Dynamic Viscosity [kg/m-s]
200	0.423309281	4.685092285	0.093688176	14.92236911
210	0.403075259	4.685043721	0.097038278	15.43404666
220	0.384698615	4.684919439	0.100337363	15.93835999
230	0.367926149	4.684883016	0.103585717	16.43530909
240	0.352564089	4.684870875	0.106797137	16.92689395
250	0.338427448	4.684858734	0.109973367	17.41211459
260	0.325381878	4.684858734	0.113100265	17.89197099
270	0.313317313	4.684783016	0.116198396	18.36646316
280	0.302108193	4.684807298	0.119255729	18.83659111
290	0.291686307	4.68483158	0.122285305	19.30047623
300	0.281947018	4.684880144	0.125281117	19.76087571
310	0.272839688	4.684928708	0.128250099	20.21615379
320	0.264304891	4.684977272	0.131185483	20.66794622
330	0.256300773	4.685050118	0.134094198	21.11449583
340	0.248755768	4.685135105	0.136977687	21.55780262
350	0.241641664	4.685220092	0.139834632	21.99774519
360	0.234923605	4.685317221	0.142666449	22.43344493
370	0.228572165	4.68542649	0.145472497	22.86590185
380	0.222555202	4.6855479	0.148259713	23.29411595
390	0.216843005	4.685593592	0.151022585	23.72008723
400	0.211423432	4.685727143	0.153767367	24.14181569
410	0.206267985	4.685884976	0.156487186	24.56130133
420	0.201350593	4.686042809	0.15918272	24.97754415
430	0.196670329	4.686212783	0.161867162	25.39066556
440	0.192202336	4.686394899	0.164527361	25.80142274
450	0.187930545	4.686577014	0.167170251	26.20905851
460	0.183838884	4.68677127	0.169795852	26.61357287
470	0.179932497	4.686977667	0.172404179	27.01584441
480	0.176176529	4.687196205	0.175002833	27.41587313
490	0.172585243	4.687414744	0.177577305	27.81365903
500	0.169133241	4.687645423	0.180135187	28.20844493
510	0.165816879	4.687876102	0.182676488	28.60098801
520	0.162627789	4.688118922	0.185208161	28.99140967
530	0.159559147	4.688361742	0.187723272	29.37970993
540	0.156604676	4.688616704	0.190221184	29.76576737
550	0.15375722	4.688871665	0.19271078	30.1497034
560	0.151011714	4.689138767	0.195183193	30.53151802
570	0.148362216	4.689405869	0.197646665	30.91121123
580	0.14580542	4.689672972	0.200093603	31.28966161
590	0.143334167	4.689952215	0.202524648	31.665112
600	0.140945488	4.690231458	0.204946764	32.03944098
610	0.138634318	4.690510701	0.20735299	32.41152714
620	0.136399779	4.690802086	0.209756636	32.78261329
630	0.134234378	4.691081329	0.212137429	33.15057804
640	0.132136358	4.691372713	0.214516915	33.51829997
650	0.130103627	4.691664097	0.216879892	33.8831433
660	0.128132878	4.691955482	0.219227619	34.24674382
670	0.126221474	4.692246866	0.221573423	34.60922293
680	0.124365231	4.69253825	0.223903353	34.96882344

Table A-5. (cont.)

0.5 Helium – 0.5 Air				
Temperature [K]	Density [kg/m3]	Specific Heat [kJ/kg-K]	Thermal Conductivity [W/m-K]	Dynamic Viscosity [kg/m-s]
690	0.1225626	4.692829635	0.226225014	35.32805973
700	0.120811279	4.693121019	0.228537785	35.68541743
710	0.119110933	4.693412403	0.230842292	36.0415323
720	0.117457377	4.693703787	0.233130928	36.39564718
730	0.11584764	4.693995172	0.235411303	36.74864065
740	0.114281721	4.694286556	0.237689783	37.09963411
750	0.112758742	4.694565799	0.239953639	37.45038476
760	0.111275396	4.694857183	0.242208616	37.79837823
770	0.109830805	4.695148568	0.244455338	38.14600746
780	0.108422876	4.695427811	0.246693185	38.49175811
790	0.10705073	4.695719195	0.248923398	38.83726593
800	0.105712275	4.695998438	0.251145357	39.18077376
810	0.10440751	4.696277682	0.253358448	39.52228159
820	0.103135222	4.696556925	0.255563904	39.863668
830	0.101892439	4.696824027	0.25776111	40.20305442
840	0.100680376	4.69710327	0.259950066	40.54144083
850	0.099494846	4.697370373	0.262130772	40.87958443
860	0.098338822	4.697637475	0.264303231	41.21584943
870	0.097208118	4.697904577	0.266468055	41.55099303
880	0.096104283	4.698171679	0.268631635	41.88413663
890	0.095024554	4.698438782	0.270779965	42.21715881
900	0.093968387	4.698693743	0.272927665	42.549181
910	0.092935783	4.698948704	0.27506712	42.88008177
920	0.091926407	4.699203665	0.277191935	43.20910396
930	0.090937621	4.699458627	0.279322518	43.53800473
940	0.089971185	4.699701447	0.28143785	43.8657841
950	0.089024125	4.699944267	0.283545548	44.19180628
960	0.088096443	4.700187087	0.285652621	44.51746424
970	0.087188138	4.700429908	0.287751451	44.8422436
980	0.086299211	4.700660587	0.289842647	45.16590156
990	0.085427568	4.700891266	0.291932613	45.48868092
1000	0.08457321	4.701134086	0.294007932	45.81033888